A study of $\tau^- \to \pi^-\pi^0\nu_\tau$ using the *BABAR* detector

Jonathan David Fullwood

THE UNIVERSITY of MANCHESTER

Particle Physics Group

Department of Physics and Astronomy

May, 2001

A thesis submitted to The University of Manchester for the degree of Doctor of Philosophy in the Faculty of Science and Engineering

Contents

Abstract 6

Declaration 7

The author 8

Acknowledgements 9

1 Introduction **11**

2 Tau physics with *BABAR* **14**

2.1 Properties of the τ lepton 14

2.1.1 The τ mass 15

2.1.2 The τ lifetime 15

2.2 Tau-pair production at *BABAR* 16

2.3 Hadronic τ decays and conserved vector current 17

2.3.1 Hadronic τ decays 17

2.3.2 Vector and axial-vector currents 19

2.4 Phenomenology and models 20

2.4.1 Models of the hadronic current 20

2.4.2 The model of Kühn and Santamaria 22

2.4.3 The model of Gounaris and Sakurai 23

2.5 Previous experimental results 24

2.5.1 The ALEPH measurements 24

2.5.2 The CLEO measurements 25

3 The *BaBar* experiment **29**

3.1 The PEP-II collider 30

3.1.1 Overview 30

3.1.2 The interaction region 32

3.1.3 Machine backgrounds 33

3.2 The *BaBar* detector 36

3.2.1 The silicon vertex tracker 37

3.2.2 The drift chamber 43

3.2.3 The DIRC particle identification system 47

3.2.4 The electromagnetic calorimeter 51

3.2.5 The instrumented flux return 56

3.2.6 The trigger system 60

4 *BaBar* software **63**

4.1 The C++ programming language 64

4.1.1 Object-oriented programming 64

4.1.2 Inheritance 65

4.1.3 Encapsulation 65

4.1.4 Polymorphism 66

4.2 Simulation 66

4.2.1 Event generators 66

4.2.2 Detector model 67

4.2.3 Detector response simulation and reconstruction 68

4.3 Online prompt reconstruction 68

5 Electron control sample for particle identification **70**

5.1 Motivation for producing the sample 71

5.2 Event properties 73

5.3 The Monte Carlo sample 75

5.4 Trigger efficiency 76

5.5 Event selection 76

5.6 Electron candidate selection 82

5.7 Properties of the sample 83

5.8 Summary 85

6 Selection of $\tau^- \to \pi^-\pi^0\nu_\tau$ candidate events **87**

6.1 Data samples 88

6.1.1 The data sample 88

6.1.2 The Monte Carlo samples 88

6.1.3 The TauQED skim 89

6.1.4 The BGFTau filter . . . 91
6.2 Event selection . . . 93
6.2.1 Charged candidate selection . . . 94
6.2.2 Neutral candidate selection . . . 94
6.2.3 Neutral pion reconstruction . . . 97
6.2.4 The event tag . . . 100
6.2.5 Rho meson reconstruction . . . 103
6.2.6 Background rejection . . . 105
6.3 Background subtraction . . . 107
6.3.1 Background contributions . . . 107
6.3.2 Background subtraction . . . 109
6.3.3 Error propagation . . . 111
6.4 Selection efficiency . . . 114

7 Results and conclusion **117**
7.1 Fitting procedure . . . 117
7.1.1 The model of Kühn and Santamaria . . . 123
7.1.2 The model of Gounaris and Sakurai . . . 124
7.2 Comparison with previously published results . . . 124
7.3 Fully corrected mass spectrum . . . 129
7.3.1 The problem . . . 130
7.3.2 The correction method . . . 130

7.3.3 Treatment of errors 135

7.4 Conclusions 137

A Electromagnetic calorimeter cluster lateral moment **145**

B Track-cluster matching **147**

Abstract

A study of the $\pi^-\pi^0$ invariant mass spectrum in the hadronic decay $\tau^- \to \pi^-\pi^0\nu_\tau$ was performed using $19.2\,\mathrm{fb}^{-1}$ of data from the *BABAR* detector operating at the PEP-II e^+e^- collider. Two different models for the weak pion form factor were used to fit the $\pi^-\pi^0$ invariant mass spectrum. All fits to the mass spectrum, with and without a contribution from the $\rho(1700)$ meson, gave acceptable fits, with no clear preference for any one.

Declaration

No portion of the work referred to in this thesis has been submitted in support of an application for another degree or qualification of this or any other university or other institute of learning.

The author

Jonathan Fullwood was educated at Cheslyn Hay High School, Cheslyn Hay, Staffordshire, between 1987 and 1994, before obtaining a first class B.Sc. (Hons) degree in Physics at the University of Manchester in 1997. The work presented in this thesis was conducted at the University of Manchester and the Stanford Linear Accelerator Center, California.

Acknowledgements

I would like to thank my supervisor George Lafferty for his guidance, encouragement and patience. Thanks also to the many people I have had the pleasure of working with, on both sides of the Atlantic, during the last four years.

I should definitely thank Jim, David and John for some (literally) unbelievable nights out in Manchester. Nik and Alessandra also deserve a big thank you for providing some memorable moments (and sandwiches).

Jamie, Mark, Pete and the rest of the SLAC *soccer?* team deserve a mention. *Great D!* I would also like to say a big thank you to Dave and the *BABAR* ski team.

Mickey and his behemoth **t e l e v i s i o n** set deserve a special mention, as does the Chrysler Motor Company.

To all of the people at Manchester and SLAC that are too many to mention individually "Thank you for my making the last four years very enjoyable ones." Special thanks go out to all those present in Abingdon, Edinburgh, Seattle, Elba and on the numerous other excursions — you know who you are.

Finally, I would like to thank my family for their continuous love, support and encouragement. I couldn't have done it without you.

To my parents

1

Introduction

The *BABAR* experiment [1] is situated at the Stanford Linear Accelerator Center and started logging data in 1999. In combination with the PEP-II machine [2], which collides electrons and positrons at centre of mass energies $\sqrt{s} \sim 10$ GeV, the *BABAR* detector was designed with the primary goal of studying CP asymmetries in the decays of neutral B mesons. However, e^+e^- collisions at these energies also produce copious quantities of τ-lepton pairs. It is these τ-pair events which form the basis for the analysis presented here.

The main physics goal of the experiment imposed a number of specific requirements on the design of both the detector and the collider. In order to measure the CP asymmetries mentioned above, it is important that three specific requirements are met. First, the exclusive final states must be fully reconstructed. Second, it must be possible to flavour-tag $B\overline{B}$ events. Finally, the proper time of the B^0 decay with respect to its production needs to be measured. Furthermore, although the CP asymmetries to be measured may be quite large, the branching ratios for the states in question are very small. Although only a few hundred fully reconstructed events may be needed in a particular channel, branching ratios of order 10^{-5} mean that in excess of 10^7 $B\overline{B}$ pairs need to be produced in order to measure the asymmetries with errors at the 10% level or better.

As a result of the clean environment and the high luminosity of the collider, in addition to measurements of asymmetries in B decays, a range of other physics can be studied at BABAR. In particular, conditions are favourable for τ physics.

This thesis contains details of a study of the invariant mass spectrum of the hadronic system in the decay $\tau^- \to \pi^-\pi^0\nu_\tau$.[†] It is believed (as discussed in Chapter 2) that the decay $\tau^- \to \pi^-\pi^0\nu_\tau$ is dominated by the formation of the lowest lying vector meson, the $\rho(770)$, with a contribution from the $\rho(1450)$ and possibly the $\rho(1700)$. Although there is strong experimental evidence for the existence of these radial excitations [3], the structure of the states is not completely clear. New data can help to increase understanding in this area.

In addition to details of the invariant mass spectrum analysis, this thesis also describes an algorithm developed to allow the production of an electron control sample. Extracted from experimental data, the sample can be used in the calibration of particle identification software. An explanation of the relevance of this work to the mass spectrum analysis is included in Section 5.1.

[†] Throughout this thesis, charge conjugate states are implied.

The information contained in this thesis is organised as follows: Chapter 2 contains a summary of the properties of the τ lepton, an outline of the theory of hadronic τ decays and a review of some relevant published results. A brief description of the PEP-II machine and *BABAR* detector can be found in Chapter 3 and details of the software used by the experiment in Chapter 4. Chapter 5 provides details of the cut-based selection algorithm devised to allow the production of an electron control sample. Finally, Chapters 6 and 7 go on to discuss the analysis, giving details of event selection, error analysis and the results of the study.

2

Tau physics with *BABAR*

2.1 Properties of the τ lepton

The τ lepton was discovered in 1975 by M. Perl *et al.* [4] using the MARK I detector situated on the SPEAR e^+e^- collider at the Stanford Linear Accelerator Center. The discovery was the first evidence for a third generation of elementary fermions; the magnitude and behaviour of the $e^+e^- \to \tau^+\tau^-$ cross section were consistent with the production of point-like spin-$\frac{1}{2}$ Dirac particles. Since the first evidence of the τ, a series of measurements have revealed its properties, a selection of which are summarised in the following sections.

2.1.1 The τ mass

Unlike the electron and muon, the τ is more massive than the lightest hadrons and can thus undergo hadronic decays. The most precise measurement of the τ mass was published in 1996 by the BES Collaboration [5]. The method employed in making this measurement involved fitting the $e^+e^- \rightarrow \tau^+\tau^-$ production cross section, which, at threshold energies is given by [6]

$$\sigma_\tau = \frac{4\pi\alpha^2}{3s}\frac{\beta(3-\beta^2)}{2}F_c, \tag{2.1}$$

where α is the electromagnetic coupling constant and $\beta = (1-4M_\tau^2/s)^{1/2}$. M_τ is the τ mass and s is the centre of mass energy squared. F_c has the form

$$F_c \sim \frac{\pi\alpha}{\beta(1-exp(-\pi\alpha/\beta))}, \tag{2.2}$$

and accounts for the Coulomb attraction between the τ^+ and τ^-. The BES Collaboration reported a τ mass of

$$M_\tau = 1776.96^{+0.18}_{-0.21}{}^{+0.25}_{-0.17}\,\mathrm{MeV/c^2}.$$

The current Particle Data Group world average value for the τ mass is [3]

$$M_\tau = 1777.03^{+0.30}_{-0.26}\,\mathrm{MeV/c^2}.$$

2.1.2 The τ lifetime

Until recently, the LEP experiments dominated the measurements of the τ lifetime as a result of their high-resolution silicon vertex detectors. At LEP-I energies, τ-pairs are produced in Z^0 decays and the τ decay vertex is displaced by an average of 2.2 mm from the $\tau^+\tau^-$ production vertex. Although numerous methods for determining the τ lifetime exist [7–10], all of the LEP measurements are statistically limited.

The most recent Particle Data Group world average value of the measurements,

$$\tau_\tau = (290.6 \pm 1.1) \text{ fs},$$

includes a result from the CLEO collaboration [11], which, although less precise than the LEP measurements, is no longer statistically limited. We can expect a series of additional measurements of the τ lifetime from new experiments including *BABAR* at PEP-II, BELLE at KEKB [12] and CLEO III at CESR [13].

2.2 Tau-pair production at *BABAR*

The cross section for τ-pair production through $e^+e^- \to \tau^+\tau^-$, as a function of centre of mass energy, is shown in Figure 2.1.

At threshold, $s = 4M_\tau^2$ so that $\beta = 0$ and (from (2.1)) the total cross section for τ-pair production is given by

$$\sigma_\tau^{\text{threshold}} = \frac{\pi^2\alpha^3}{2M_\tau^2} = 0.23 \text{ nb.} \tag{2.3}$$

Inserting the optimal PEP-II centre of mass energy ($\sqrt{s} = 10.58$ GeV) into (2.1) and (2.2), the resulting τ-pair production cross section is 0.94 nb.

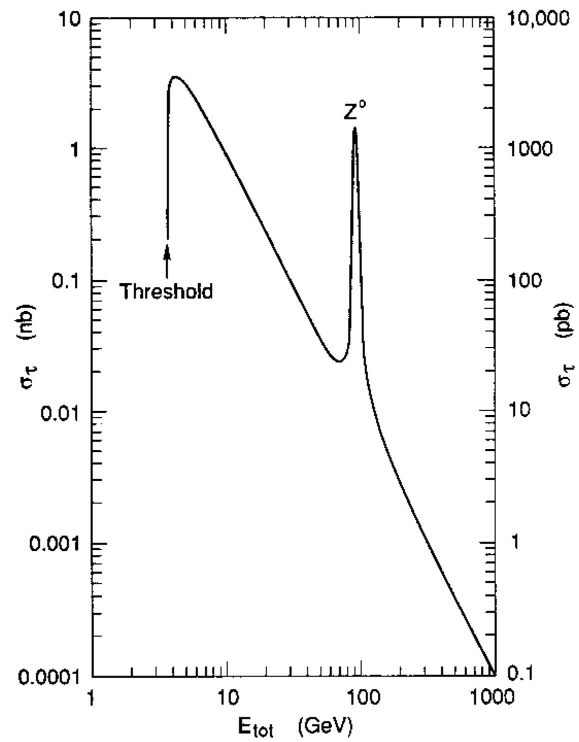

Figure 2.1: *The cross section as a function of centre of mass energy for τ-pair production through $e^+e^- \to \tau^+\tau^-$.*

2.3 Hadronic τ decays and conserved vector current

2.3.1 Hadronic τ decays

The invariant amplitude for semileptonic (hadronic) τ decays can be written [14] (in analogy to purely leptonic τ decays) in the form of a current-current interaction,

$$\mathcal{M}(\tau^- \to h^-\nu_\tau) = \frac{G_F}{\sqrt{2}}|V_h|L_\mu H^\mu, \tag{2.4}$$

where h^- represents a particular hadronic system. V_h is the corresponding element of the Cabibbo-Kobayashi-Maskawa matrix (V_{ud} for non-strange h^- and V_{us} for strange h^-) and G_F denotes the Fermi coupling constant. A Feynman diagram for the process is shown in Figure 2.2. The leptonic current is given by

$$L_\mu = \bar{v}_{\nu_\tau} \gamma_\mu (1 - \gamma_5) u_\tau, \tag{2.5}$$

where $\bar{v}_{\nu_\tau}$ and u_τ are Dirac spinors and γ_μ and γ_5 the usual gamma matrices [15]. The hadronic current, H_μ, can in general be expressed in terms of a vector (V) and an axial-vector (A) current

$$H_\mu = \langle h^- | V_\mu(0) - A_\mu(0) | 0 \rangle. \tag{2.6}$$

The hadronic current describes how the hadronic final state is formed from the vacuum by the weak charged current.

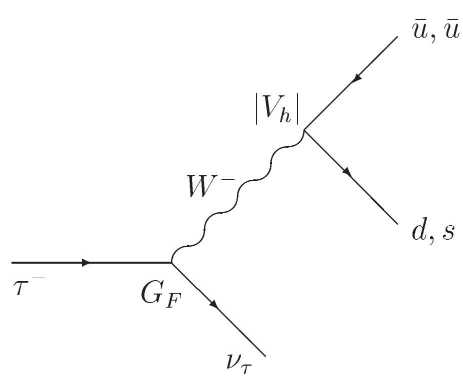

Figure 2.2: *Feynman diagram for semileptonic τ decay.*

It can be shown [16] that the differential τ width into a system $h^-\nu_\tau$, can be expressed as

$$\mathrm{d}\Gamma(\tau^- \to h^- \nu_\tau) = \frac{G_F^2}{4M_\tau} |V_h|^2 L_{\mu\nu} H^{\mu\nu} \mathrm{d}PS, \tag{2.7}$$

with $L_{\mu\nu}$ the leptonic tensor (arising from the square of L_μ), $H^{\mu\nu}$ the hadronic tensor and $\mathrm{d}PS$ the Lorentz invariant phase space element. In the rest frame of the hadronic system h^-, the tensor product simplifies to a sum over structure functions and kinematic factors [16]. For the decay modes $\tau^- \to \pi^- \nu_\tau$ and $\tau^- \to K^- \nu_\tau$, the structure functions are delta-functions, such that the τ partial widths are directly related to the corresponding weak decay rate of the hadron:

$$\Gamma(\tau^- \to \pi^- \nu_\tau) = \frac{G_F^2}{16\pi} f_\pi^2 |V_{ud}|^2 M_\tau^3 \left(1 - \frac{m_\pi^2}{M_\tau^2}\right)^2 , \tag{2.8}$$

where m_π is the charged pion mass and f_π^2 is the pion decay constant defined by the width

$$\Gamma(\pi^- \to \mu^- \bar{\nu_\mu}) = \frac{G_F^2}{8\pi} f_\pi^2 |V_{ud}|^2 m_\pi m_\mu^2 \left(1 - \frac{m_\mu^2}{m_\pi^2}\right)^2 , \tag{2.9}$$

where m_μ is the muon mass. Corresponding relations for $\tau^- \to K^- \nu_\tau$ follow by replacing the pion mass with the kaon mass and $f_\pi |V_{ud}|$ with $f_K |V_{us}|$.

2.3.2 Vector and axial-vector currents

The quantum number corresponding to the conserved vector and axial-vector currents is that of the isotopic parity (G-parity), the operation of isospin rotation followed by charge conjugation. Considering the properties of the weak charged current shown in Table 2.1, it is clear that the measurement of non-strange τ vector current properties will require the measurement of τ decay modes with a G-parity, $G = +1$. Similarly, the measurement of τ axial-vector current properties will require decay modes with a G-parity, $G = -1$.

The conservation of G-parity implies that, in the case of the decay of a τ lepton to pions (which have $G = -1$), decay modes with an even number of pions will proceed via the vector current, while those with an odd number of pions will proceed via the axial-vector current.

The weak current and its conjugate, together with the electromagnetic current are believed to form an isospin triplet of conserved currents. This is referred to as the *conserved vector current hypothesis* (CVC). In semileptonic τ decays, the description of hadronic resonance production is complicated by the structure of

Table 2.1: Properties of the weak charged current.

Property	Vector current (V)	Axial-vector current (A)
Isospin I	1	1
G-parity G	$+1$	-1
Spin-parity J^P	1^-	$0^-, 1^+$

the resonance itself. For even G-parity final states however, only the vector current contributes and CVC provides a convenient way to relate the decay width to the cross section for $e^+e^- \to \mathrm{hadrons}$. A discussion of the application of CVC to the channel $\tau^- \to \pi^-\pi^0\nu_\tau$ can be found in Section 2.4.1.

2.4 Phenomenology and models

2.4.1 Models of the hadronic current

Expanding the ideas presented in Section 2.3 we go on to consider the decay $\tau^- \to \pi^-\pi^0\nu_\tau$ in more detail.

The general form of the decay rate for hadronic decays of a heavy lepton, derived [17] four years before the discovery of the τ, can be written as [18]

$$\begin{aligned}\Gamma(\tau^- \to h^- + \nu_\tau) = {} & \frac{G_F^2}{32\pi^2 M_\tau^3}\int_0^{M_\tau^2} \mathrm{d}q^2 \left(M_\tau^2 - q^2\right)^2 \\ & \Big\{ \cos^2\theta_c \left[\left(M_\tau^2 + 2q^2\right)\left(v_1(q^2) + a_1(q^2)\right) + M_\tau^2 a_0(q^2)\right] \\ & + \sin^2\theta_c \Big[\left(M_\tau^2 + 2q^2\right)\left(v_1^s(q^2) + a_1^s(q^2)\right) + M_\tau^2\left(v_0^s(q^2) + a_0^s(q^2)\right) \Big] \Big\}\end{aligned} \tag{2.10}$$

where q^2 is the invariant mass squared of the hadronic system and θ_c is the Cabibbo angle. As usual, G_F is the Fermi constant and M_τ is the rest mass of the τ. The

v and a refer to spectral functions connected to the vector (V) and axial-vector (A) parts of the weak charged current. The numerical subscript indicates the spin of the hadronic final state and a superscript s denotes the Cabibbo-suppressed strange decays. The spectral functions are different for every hadronic final state. They are continuous functions of q^2, except in the special cases $h^- = \pi^-$ and $h^- = K^-$ when they are delta functions (as described in Section 2.3.1).

Simplifying the general formulation of hadronic τ decay widths (recalling that the two-pion decay mode proceeds via the vector current only), the partial width for $\tau^- \to \pi^-\pi^0\nu_\tau$ can be written [19] as a function of $\pi^-\pi^0$ invariant mass, q:

$$\frac{\mathrm{d}\Gamma(\tau^- \to \pi^-\pi^0\nu_\tau)}{\mathrm{d}q^2} = \frac{G_F^2|V_{ud}|^2 S_{ew}^{\pi\pi}}{32\pi^2 M_\tau^3}(M_\tau^2 - q^2)^2(M_\tau^2 + 2q^2)v^{\pi\pi^0}(q^2). \quad (2.11)$$

V_{ud} is the Cabibbo-Kobayashi-Maskawa matrix element, $S_{ew}^{\pi\pi}$ has been introduced to denote electroweak radiative corrections and $v^{\pi\pi^0}(q^2)$ is the vector spectral function. The corresponding $\pi^+\pi^-$ spectral function is related to the cross section for $e^+e^- \to \pi^+\pi^-$

$$\sigma(e^+e^- \to \pi^+\pi^-) = \left(\frac{4\pi^2\alpha^2}{s}\right) v^{\pi\pi}(s), \quad (2.12)$$

where α is the electromagnetic coupling constant and s the squared e^+e^- centre of mass energy. The isovector part of the spectral function $v^{\pi\pi}$ can be related to the spectral function from $\tau^- \to \pi^-\pi^0\nu_\tau$ decay by the application of CVC:

$$v_{I=1}^{\pi\pi}(s) = v^{\pi\pi^0}(q^2). \quad (2.13)$$

Furthermore, the $e^+e^- \to \pi^+\pi^-$ spectral function can be expressed in terms of the pion electromagnetic form factor $F_\pi(q^2)$

$$v^{\pi\pi}(q^2) = \frac{1}{12\pi}|F_\pi(q^2)|^2 \left(\frac{2p_\pi}{\sqrt{q^2}}\right)^3. \quad (2.14)$$

The last factor represents the p-wave phase space factor; p_π is the momentum of one of the pions in the $\pi\pi$ rest frame. The weak pion form factor, which describes phenomenologically the probability density of the transition $W^- \to \pi^-\pi^0$, can be used in a similar expression for the τ decay spectral function.

Various models for the weak pion form factor exist since its exact form is not presently calculable in QCD (the electric charge of the π^- does however imply that $F_\pi(0) = 1$). It is expected that F_π is dominated by the line shape of the $\rho(770)$, with contributions from its radial excitations, the $\rho(1450)$ and possibly the $\rho(1700)$. For convenience, in the following sections the $\rho(1450)$ and $\rho(1700)$ are denoted as ρ' and ρ'' respectively.

2.4.2 The model of Kühn and Santamaria

One model for the pion form factor is that of Kühn and Santamaria [20], which has the form

$$F_\pi^{(I=1)}(q^2) = \frac{1}{1+\beta+\gamma+....}(BW_\rho + \beta BW_{\rho'} + \gamma BW_{\rho''} + ...), \tag{2.15}$$

where BW_ρ represents the Breit-Wigner amplitude associated with the ρ resonance line shape

$$BW_\rho = \frac{M_\rho^2}{(M_\rho^2 - q^2) - i\sqrt{q^2}\Gamma_\rho(q^2)}. \tag{2.16}$$

The parameters β and γ specify the relative couplings to the ρ' and ρ'' respectively. M_ρ and $\Gamma_\rho(q^2)$ denote the ρ meson mass and mass-dependant total decay width, the latter of which can be written [20]

$$\Gamma_\rho(q^2) = \Gamma_\rho \frac{M_\rho^2 p_\pi^3}{q^2 p_0^3}, \tag{2.17}$$

where Γ_ρ denotes $\Gamma_\rho(q^2 = M_\rho^2)$ and

$$2p_\pi = (q^2 - 4m_\pi^2)^{1/2}, \;\; 2p_0 = (M_\rho^2 - 4m_\pi^2)^{1/2}. \tag{2.18}$$

2.4.3 The model of Gounaris and Sakurai

The model of Gounaris and Sakurai [21] starts from a more elaborate treatment of the p-wave scattering amplitude for a broad resonance, which yields

$$F_\pi^{(I=1)}(q^2) = \frac{M_\rho^2 + M_\rho \Gamma_\rho d}{(M_\rho^2 - q^2) + f(q^2) - i\sqrt{q^2}\Gamma_\rho(q^2)}, \tag{2.19}$$

where the q^2 dependence of $\Gamma_\rho(q^2)$ is the same as in (2.17). The function $f(q^2)$ is given by

$$f(q^2) = \frac{\Gamma_\rho M_\rho^2}{p_0^3}\left[p_\pi^2(q^2)\left[h(q^2) - h(M_\rho^2)\right] - p_0^2(q^2 - M_\rho^2)\left.\frac{\mathrm{d}h}{\mathrm{d}q^2}\right|_{q^2=M_\rho^2}\right] \tag{2.20}$$

with

$$h(q^2) = \frac{2p_\pi(q^2)}{\pi\sqrt{q^2}} \ln \frac{\sqrt{q^2} + 2p_\pi(q^2)}{2m_\pi}, \tag{2.21}$$

so that [22]

$$\left.\frac{\mathrm{d}h}{\mathrm{d}q^2}\right|_{q^2=M_\rho^2} = h(M_\rho^2)\left[\frac{1}{8p_0} - \frac{1}{2M_\rho^2}\right] + \frac{1}{2\pi M_\rho^2}. \tag{2.22}$$

The parameter d is given by

$$d = \frac{3m_\pi^2}{\pi p_0^2} \ln \frac{M_\rho + 2p_0}{2m_\pi} + \frac{M_\rho}{2\pi p_0} - \frac{m_\pi^2 M_\rho}{\pi p_0^3}. \tag{2.23}$$

This model can be extended to include possible ρ' and ρ'' contributions (as in (2.15)) [20, 22, 23].

Near $q^2 = M_\rho^2$, the function $f(q^2)$ in (2.19) goes as $M_\rho^2 - q^2$ so that the Gounaris and Sakurai form for F_π is similar to that implied by the Kühn and Santamaria model. The Gounaris and Sakurai model does however have a larger value for $F_\pi(q^2 = M_\rho^2)$ (relative to the Kühn and Santamaria model with the same values for M_ρ and Γ_ρ) as a result of the additional term in the numerator of (2.19). For d = 0.48 (corresponding to M_ρ = 0.775 GeV), $F_\pi(M_\rho^2)$ for the Gounaris and Sakurai model is 9% larger than the value from the Kühn and Santamaria model.

2.5 Previous experimental results

2.5.1 The ALEPH measurements

A 1997 publication [22] describes an analysis based on a data set of 124,358 Z boson decays to τ-pairs, recorded by ALEPH at the LEP e^+e^- collider between 1991 and 1994.

2.5.1.1 Results

Fits to the models of Kühn and Santamaria and Gounaris and Sakurai were performed. The functions corresponding to the fits (shown in Figure 2.3) have been convolved with the detector resolution; statistical fluctuations in the detector response matrix lead to functions which are not smooth after convolution. The values of $\Gamma_{\rho'}$, $M_{\rho''}$ and $\Gamma_{\rho''}$ used in the fitting procedure were fixed to the world average values. A summary of the parameters extracted is displayed in Table 2.2.

2.5.1.2 Conclusions

The fits to the ALEPH data establish the need for the ρ' contribution to the weak pion form factor in the Kühn and Santamaria and Gounaris and Sakurai parameterisations. A weighted average of the results for the two parameterisations gives $\beta = -0.087 \pm 0.012$ with a fitted mass $M_{\rho'} = (1380 \pm 24)$ MeV/c^2 when fixing the width at $\Gamma_{\rho'} = 310$ MeV/c^2. This method yields no evidence of a ρ'' contribution ($\gamma = -0.008 \pm 0.008$). If the results from the Kühn and Santamaria and Gounaris and Sakurai fits are considered separately however, the Kühn and Santamaria fit produces a value of γ which deviates from zero by 2σ.

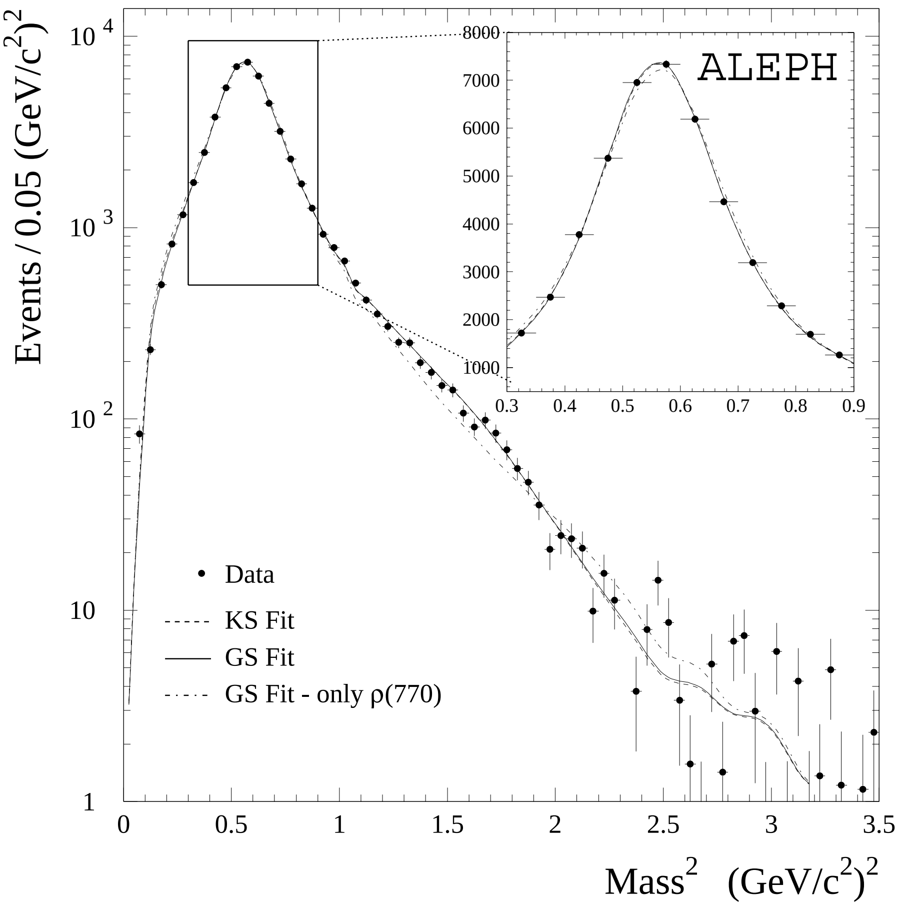

Figure 2.3: *ALEPH collaboration $M^2_{\pi^-\pi^0}$ distribution in $\tau^- \to \pi^-\pi^0\nu_\tau$ events (points). The dashed and solid curves are the functions corresponding to the Kühn and Santamaria and Gounaris and Sakurai models respectively. The dashed-dotted line corresponds to a Gounaris and Sakurai fit in which only the ρ(770) contribution is taken into account.*

2.5.2 The CLEO measurements

The most recent CLEO results were published in 2000 [19]. Based on 3.5 fb^{-1} of e^+e^- collision data, collected (between 1990 and 1994) at centre of mass energies of ∼10.6 GeV, the data correspond to a sample of 3.2×10^6 τ-pairs.

Table 2.2: *ALEPH Collaboration fit results for the Kühn and Santamaria and Gounaris and Sakurai parameterisations. Units for masses and widths are MeV/c^2.*

Parameter	Kühn and Santamaria Model	Gounaris and Sakurai Model
M_ρ	774.9 ± 0.9	776.4 ± 0.9
Γ_ρ	144.2 ± 1.5	150.5 ± 1.6
β	-0.094 ± 0.007	-0.077 ± 0.008
$M_{\rho'}$	1363 ± 15	1400 ± 16
$\Gamma_{\rho'}$	$\equiv 310$	$\equiv 310$
γ	-0.015 ± 0.008	0.001 ± 0.009
$M_{\rho''}$	$\equiv 1700$	$\equiv 1700$
$\Gamma_{\rho''}$	$\equiv 235$	$\equiv 235$
χ^2/dof	81/65	54/65

2.5.2.1 Results

Again, fits to the models of Kühn and Santamaria and Gounaris and Sakurai were performed. The results of a fit to the model of Kühn and Santamaria are shown in Figure 2.4. Results tabulated for the models with and without the ρ'' contribution are shown in Table 2.3. For the fits in which the ρ'' contribution was included, its properties were fixed to the world average values.

2.5.2.2 Conclusion

Although good fits to the data were obtained without the ρ'' meson, the χ^2 values for both the Kühn and Santamaria and Gounaris and Sakurai models were marginally improved when such a contribution was introduced.

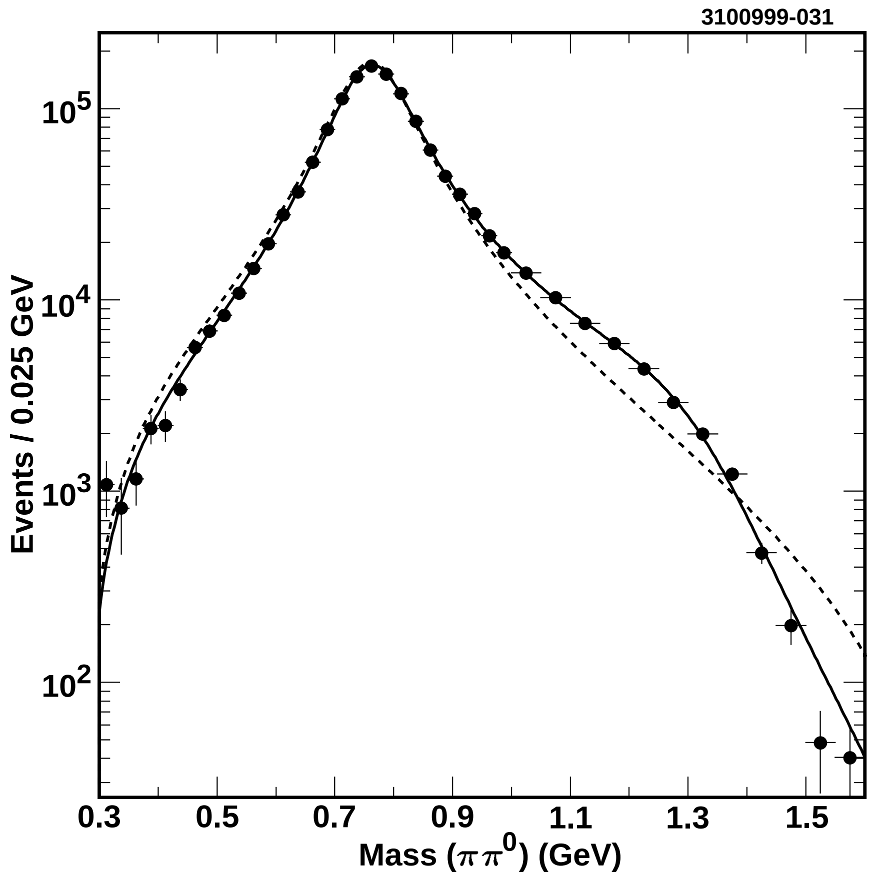

Figure 2.4: *CLEO collaboration $M_{\pi^-\pi^0}$ distribution in $\tau^- \to \pi^-\pi^0\nu_\tau$ events (points). The mass spectrum has been corrected for mass dependent reconstruction efficiency and detector resolution effects. The solid curve represents the results of a fit to the model of Kühn and Santamaria including contributions from the ρ(770) and ρ(1450). The dashed curve is obtained using the same model, but including only a single (ρ(770)) resonance.*

Table 2.3: *CLEO Collaboration fit results for the Kühn and Santamaria and Gounaris and Sakurai parameterisations. Units for masses and widths are MeV/c^2.*

Parameter	Kühn and Santamaria Model		Gounaris and Sakurai Model	
	without ρ''	with ρ''	without ρ''	with ρ''
M_ρ	774.9±0.5	774.6±0.6	775.3±0.5	775.1±0.6
Γ_ρ	149.0±1.1	149.0±1.2	150.5±1.1	150.4±1.2
β	−0.108±0.007	−0.167±0.008	−0.084±0.006	−0.121±0.009
$M_{\rho'}$	1364±7	1408±12	1365±7	1406±13
$\Gamma_{\rho'}$	400±26	502±32	356±26	455±34
γ	$\equiv$ 0	0.050±0.010	$\equiv$ 0	0.032±0.009
$M_{\rho''}$	–	$\equiv$ 1700	–	$\equiv$ 1700
$\Gamma_{\rho''}$	–	$\equiv$ 240	–	$\equiv$ 240
χ^2/dof	27.0/24	23.3/23	26.8/24	22.9/23

3

The *BaBar* experiment

The PEP-II e^+e^- collider operates at and near the $\Upsilon(4S)$ resonance in asymmetric mode with approximate beam energies of 9 GeV and 3.1 GeV for electrons and positrons respectively. Operating the machine at the $\Upsilon(4S)$ ensures a large cross section for B meson production — PEP-II is frequently referred to as a B *factory*. The difference in energy of the two beams results in a relativistic boost of the products of collisions; hence the *BaBar* detector is of asymmetric design. The optimal centre of mass energy of 10.58 GeV corresponds to a centre of mass moving in the lab with $\beta\gamma = 0.56$. The resulting average separation of the B decay vertices is of order 250 μm, sufficient for precise measurements of CP asymmetries.

Collisions of the high-energy and low-energy beams are head-on, but for part of the time that the beams are inside the detector's magnetic field, they are not aligned with each other. In order to minimise the resulting orbit distortions, the detector is rotated 20 mr relative to the beam direction. For this reason, the z axis of the detector coordinate system is aligned with the magnetic field direction, deviating slightly from the boost direction.

The detector, shown in Figure 3.1, is made up of a roughly cylindrical system of sub-detectors which are arranged around the PEP-II beamline and a further set of sub-detectors which form endcaps. The detector coordinate system is defined so that the high-energy beam travels in the direction of increasing z. The coordinate system origin is the nominal collision point and the $+x$ direction is away from the ring centre. The positive y direction is chosen to complete a right-handed coordinate system.

3.1 The PEP-II collider

3.1.1 Overview

In order to achieve the accelerator parameters necessary to satisfy the requirements of the experiment (particularly the high luminosity), significant advances in storage ring design and construction were necessary.

The PEP-II storage ring was designed to produce a luminosity of $3\times10^{33}\,\mathrm{cm}^{-2}\mathrm{s}^{-1}$ at a centre of mass energy of 10.58 GeV. The electrons and positrons are provided by the SLAC linear accelerator. Some of the parameters of the high-energy and low-energy beams are displayed in Tables 3.1 and 3.2. The values quoted are for the period relevant to the analysis presented here, i.e. spring–summer 2000.

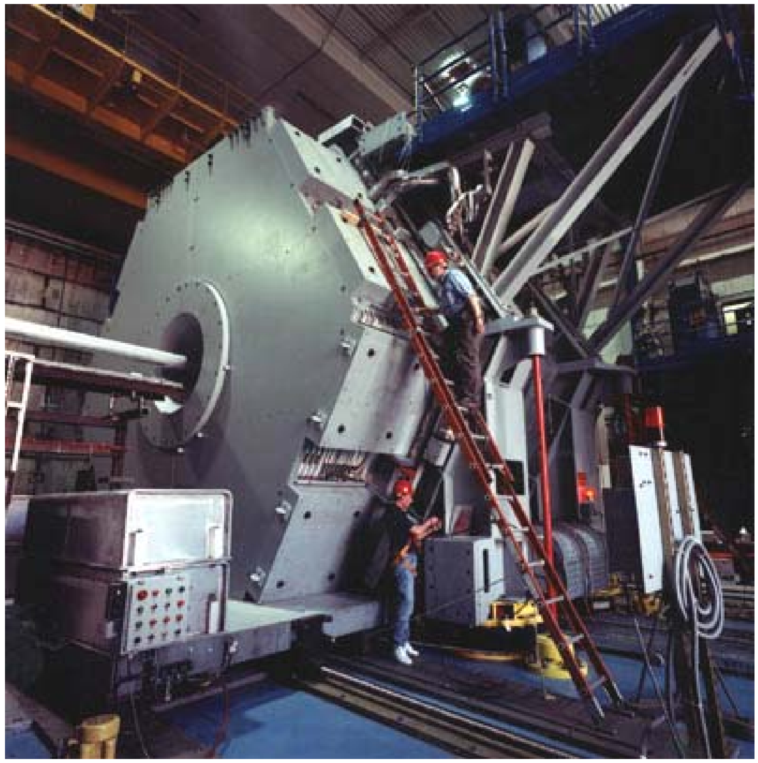

Figure 3.1: *The BABAR detector under construction at SLAC.*

Table 3.1: *PEP-II high-energy ring performance.*

Parameter	Design	Best achieved	Typical
Number of bunches	1658	1658	553-829
Total beam current	0.75 A	0.92 A	0.70 A

Table 3.2: *PEP-II low-energy ring performance.*

Parameter	Design	Best achieved	Typical
Number of bunches	1658	1660	553-829
Total beam current	2.14 A	2.14 A	1.10 A

The PEP-II design has bunches of 2.1×10^{10} electrons (high-energy ring) and 5.9×10^{10} positrons (low-energy ring) spaced at 4.2 ns. An RF (radio frequency) system provides a total of 5.1 MW from seven klystron stations and 24 conventional copper 476 MHz RF cavities. A summary of the PEP-II beam performance and interaction point (IP) parameters [24] (again for the period relevant to the analysis presented here) can be found in Table 3.3. A more detailed report can be found in [25].

Table 3.3: *PEP-II luminosity performance.*

Parameter	Design	Best achieved	Typical
Peak luminosity ($cm^{-2}s^{-1}$)	3×10^{33}	3.1×10^{33}	2.0×10^{33}
Specific luminosity ($cm^{-2}s^{-1}$/bunch)	3.1×10^{30}	4.5×10^{30}	1.8×10^{30}
IP horizontal spot size (μm)	220	190	
IP vertical spot size (μm)	6.7	6.0	
Top-off time (min)	3	2	3
Fill time (min)	6	8	10
Integrated luminosity (pb^{-1}/8 hrs)	45	61	
(pb^{-1}/day)	135	174	
(fb^{-1}/month)		3.65	
Total integrated luminosity (fb^{-1})		25.6	

3.1.2 The interaction region

The requirements of high beam currents, asymmetric energies and head on collisions resulted in an innovative design for the interaction region. Beam-line elements are positioned very close to the interaction point, which is contained within a cylindrical beryllium beam-pipe.

Beam-beam interference effects are minimised by arranging for the beams to collide only at the interaction point and by dividing the high currents into a large number of bunches. A separation dipole (B1), situated 20 cm from the interaction point (Figure 3.2), displaces the beams horizontally in order to prevent additional collisions which would otherwise occur 62 cm from the interaction point. These separation dipoles have the most significant impact on the acceptance of the detector, which is limited to lie in the region $|\cos\theta| < 0.995$, where θ is the polar angle in the laboratory frame.

The strong focusing required for the high-current beams is achieved by quadrupoles located close to the interaction point. The final quadrupole (Q1) starts 90 cm from the interaction point and is common to both the high and low-energy beams. The low-energy beam is off axis in Q1 however, in order to maximise the beam separation. The next quadrupole (Q2) focuses only the low-energy beam, as the high-energy beam passes through a field-free region. Similarly, quadrupoles Q4 and Q5 focus only the high-energy beam.

3.1.3 Machine backgrounds

High beam-currents and the separation of the high-energy and low-energy beams near the interaction point, result in machine backgrounds which are much higher than in conventional e^+e^- colliders. It is important to minimise machine backgrounds, since if they are too high the detector will suffer from high occupancy levels and even radiation damage.

There are three main sources of machine background: synchrotron radiation, lost beam particles resulting from Coulomb scattering off residual gas molecules and lost beam particles resulting from bremsstrahlung with residual gas molecules.

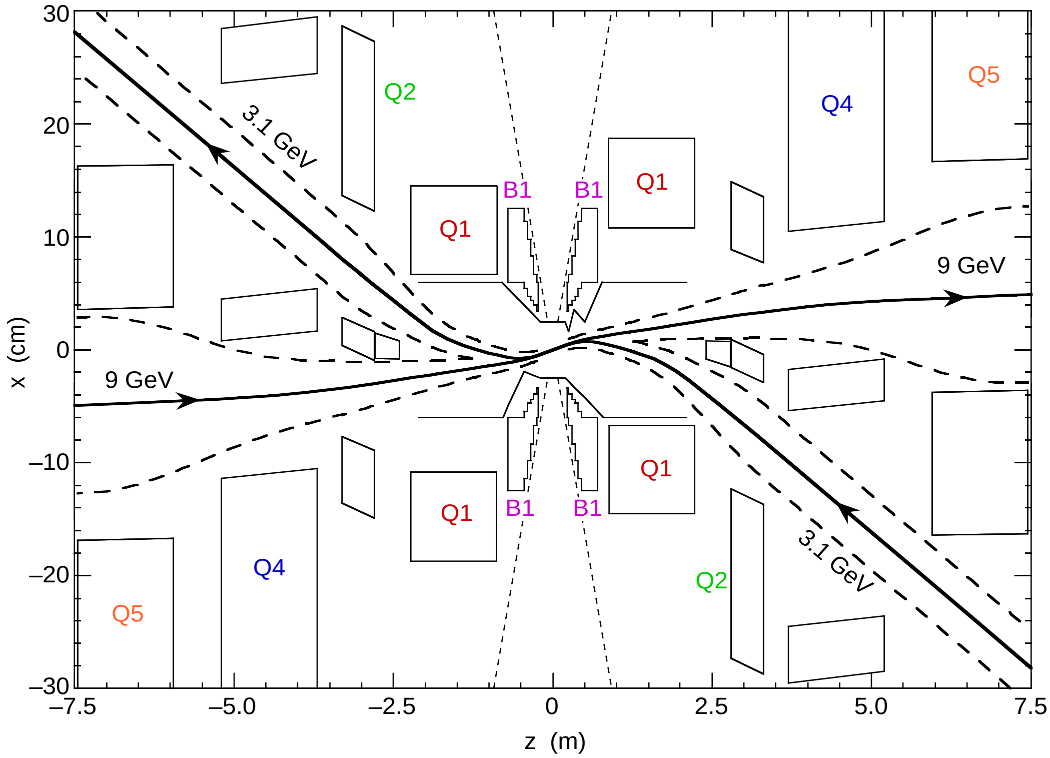

Figure 3.2: *Plan view of the interaction region (the vertical scale is highly exaggerated). Focusing quadrupoles are labelled Q1-Q5 and separation dipoles B1.*

3.1.3.1 Synchrotron radiation

Synchrotron radiation resulting from a beam passing through a dipole or offset quadrupole magnet — fan radiation — is the dominant form of synchrotron radiation background. Figure 3.3 shows how the geometry of the interaction region ensures that most fan radiation from upstream magnets passes through the detector region without interaction. In addition to the design of the interaction region, other measures to minimise backgrounds arising from synchrotron radiation include the positioning of copper masks which prevent the radiation from hitting the beampipe.

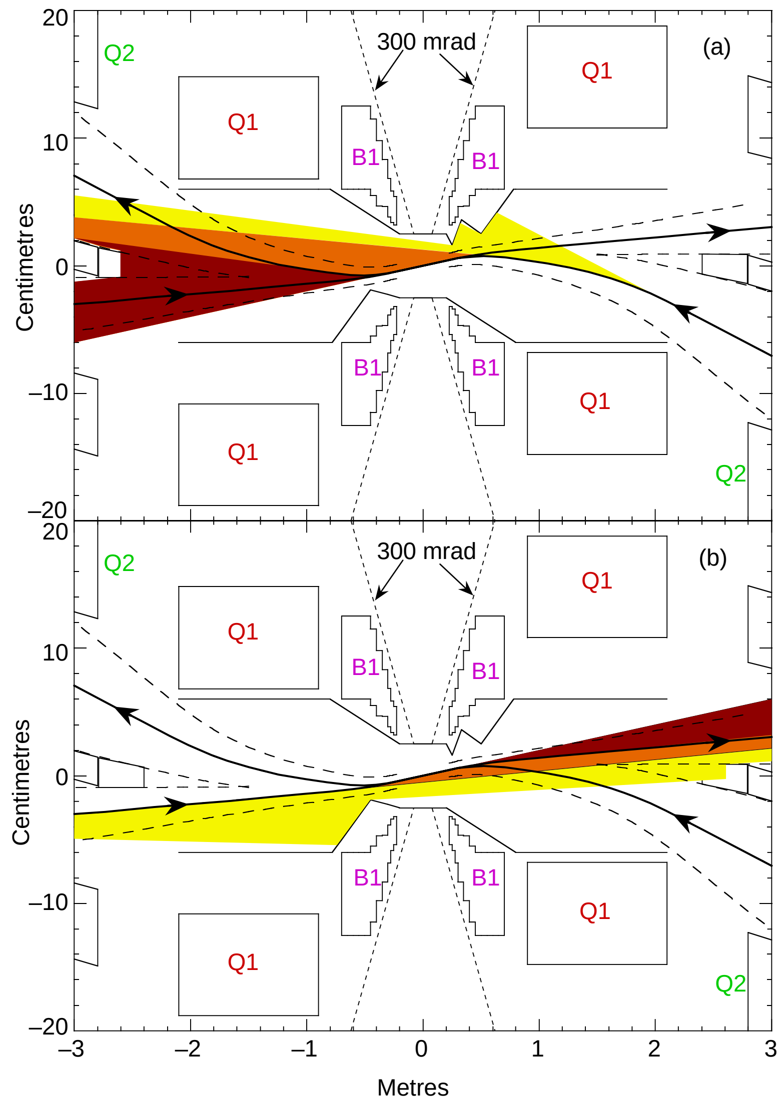

Figure 3.3: *Plan view of the interaction region including synchrotron radiation from (a) the low-energy beam and (b) the high-energy beam. The darker shading indicates regions of higher photon density.*

3.1.3.2 Lost particles

Residual gas molecules in the beam pipe can cause bremsstrahlung or Coulomb scattering of beam particles. Lost particles can interact with the material of the beampipe, resulting in electromagnetic showers. If the beam particles are lost in the vicinity of the interaction region, a high detector occupancy and possibly radiation damage may result. Because lost particles striking the beam pipe near the interaction point can arise from bremsstrahlung or Coulomb scattering occurring tens of metres away, it is essential that the pressure near to the interaction point is as low as possible.

3.2 The *BABAR* detector

A cross sectional view of the *BABAR* detector is shown in Figure 3.4. The principle components are (radially outwards from the centre of the detector):

- ◇ A silicon vertex tracker (SVT) which provides precise position information on charged tracks. The SVT can also provide dE/dx information for particle identification purposes.
- ◇ A gas-filled drift chamber which provides the main momentum measurement for charged particles. Like the SVT, the drift chamber can contribute to particle identification through energy loss measurements.
- ◇ A detector of internally reflected Čerenkov light (DIRC) which is designed and optimised for charged hadron particle identification.
- ◇ A caesium iodide electromagnetic calorimeter. Consisting of a barrel section and a forward endcap (labelled FCAL in Figure 3.4), the calorimeter detects

neutral particles and can also provide particle identification information. A backward endcap was excluded from the detector design since the boost resulting from the asymmetric collider arrangement prevents all but a small fraction of neutral particles escaping detection in the backwards direction.

- A superconducting solenoid which produces a 1.5 T magnetic field.
- An instrumented flux return providing muon identification and neutral hadron detection.

Further details of the individual detector sub-systems are contained in the following sections.

3.2.1 The silicon vertex tracker

3.2.1.1 Overview

At the heart of the detector is the silicon vertex tracker which acts as the only form of tracking for low-momentum charged particles (tracks with transverse momenta less than about 100 MeV/c will not reach the inner radius of the drift chamber). The primary role of the SVT is to provide information to allow the reconstruction of B mesons. The measurement of the time between the decays of these B mesons is essential to the process of the measurement of time-dependant CP asymmetries in B decays. A detailed description of the SVT can be found in [26].

3.2.1.2 Detector layout

The SVT consists of five concentric cylindrical layers of double-sided silicon detectors (shown in Figure 3.5). Each layer is divided into modules in azimuth. The

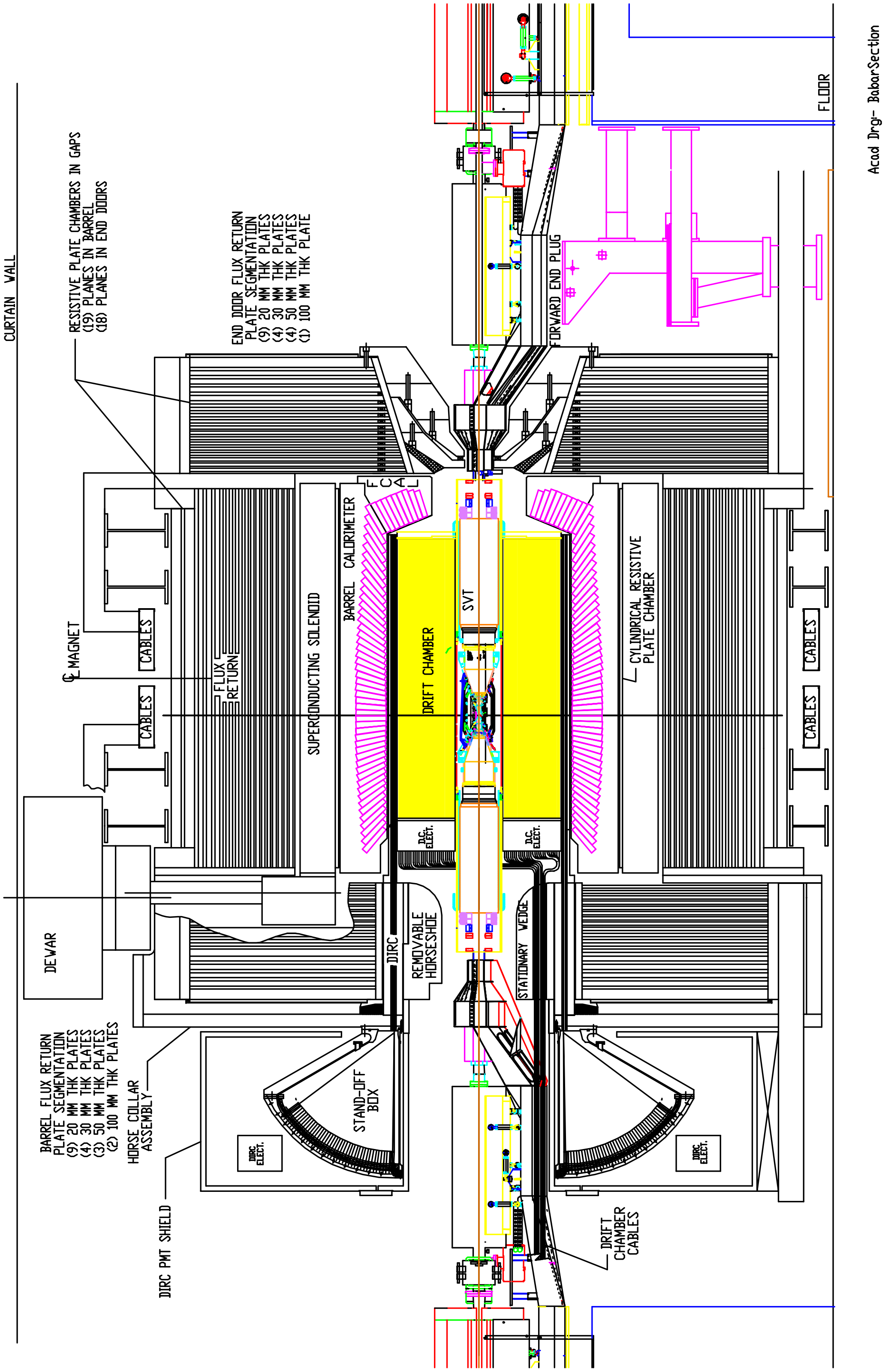

Figure 3.4: *The BABAR detector. The scale is approximately 62:1.*

inner three layers have six modules arranged in a barrel-like formation. The fourth and fifth layers consist of 16 and 18 modules respectively and are arranged in an arch-like structure in order to increase angular coverage and to avoid large track incidence angles. Figure 3.6 illustrates how the modules in the outer two layers are divided into two groups, ‘a’ modules and ‘b’ modules. The ‘a’-type modules are positioned at slightly smaller radii than the ‘b’-type modules to allow the detectors to overlap. The arrangement of the modules in the inner three layers also produces a small overlap of adjacent detectors.

The inner sides of the detector modules have silicon strip detectors running perpendicular to the beam direction to measure the z coordinate; the ϕ coordinate is measured by longitudinal strips which are mounted on the outer side of the modules. A summary of the SVT properties is presented in Table 3.4.

Table 3.4: *Parameters of the silicon vertex tracker layout.*

	Layer 1	Layer 2	Layer 3	Layer 4a	Layer 4b	Layer 5a	Layer 5b
Radius (mm)	32	40	54	124	127	140	144
Modules/layer	6	6	6	8	8	9	9
Wafers/module	4	4	6	7	7	8	8
Readout pitch (μm)							
z	100	100	100	210		210	
ϕ	55	55	55	80–100		80–100	
Intrinsic resolution (μm)							
z	12	12	12	25		25	
ϕ	10	10	10	10–12		10–12	

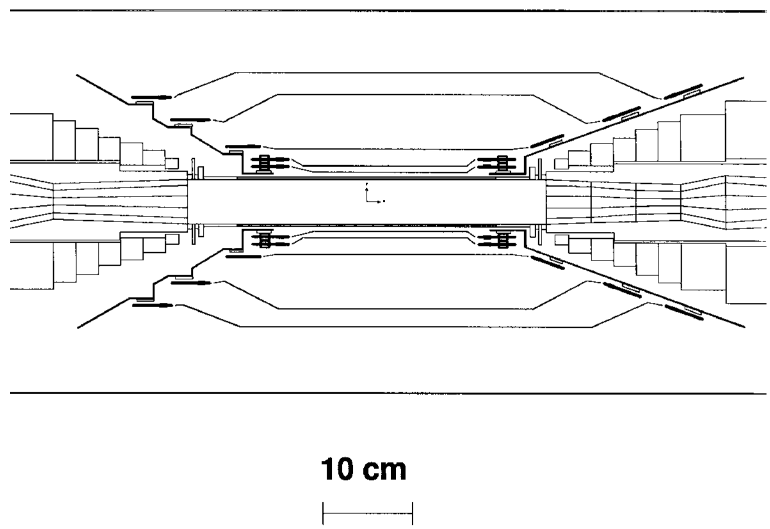

Figure 3.5: *Cross sectional view (in the y-z plane) of the silicon vertex tracker. The arch-like shape of the two outer layers is clearly visible.*

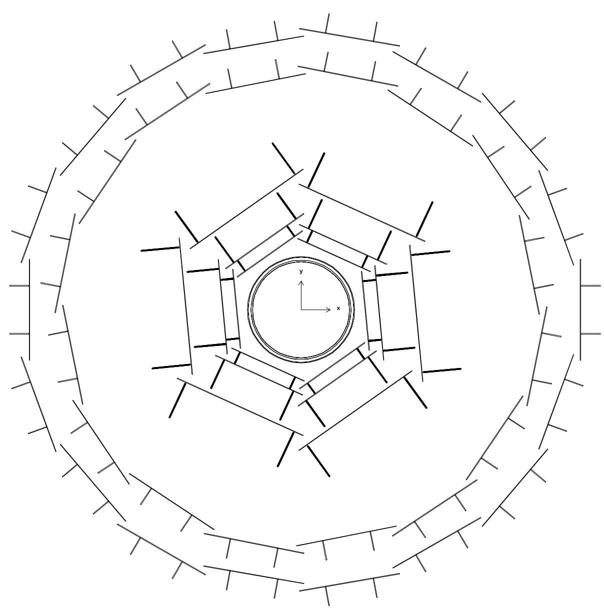

Figure 3.6: *Cross sectional view (in the x-y plane) showing the layout of the detector modules in the silicon vertex tracker. The arrangement is such that there is a small overlap of adjacent modules.*

3.2.1.3 Electronics and readout

The SVT has approximately 150,000 readout channels. Signals from all of the silicon strips need to be amplified and then electronically shaped. The time for which a signal is above some threshold is related (approximately logarithmically) to the charge which was induced on the strip. In the case of a Level-1 trigger accept (discussed in Section 3.2.6.2), the length of time over threshold is read out as a digital signal by the data acquisition system. The shaping and digitisation of the signals is performed in parallel for all channels and the digitised signal buffered for the duration of the Level-1 trigger latency. In order to achieve the high readout rates necessary, data acquisition, digitisation, buffering and readout must be able to occur simultaneously.

Front-end signal processing is performed by chips mounted on circuit boards located close to the beam line. The location of the boards means that it is necessary for the integrated circuits to be fabricated in a radiation hard CMOS technology. A system of 12 PIN photodiode sensors are mounted close to the first silicon layer in order to continuously monitor the exposure of the SVT to radiation.

3.2.1.4 Performance

The average hit reconstruction efficiency of the SVT is above 98%. An accurate alignment procedure gives rise to good hit resolution [24] as displayed in Figure 3.7.

Figure 3.8 shows the SVT impact parameter resolution as a function of track transverse momentum. The typical resolution for measuring two-track decay vertices such as $J/\psi \to \mu^+\mu^-$, is 50 μm, and the resolution on the separation between two B decay vertices is typically 110 μm. These figures are in good agreement with

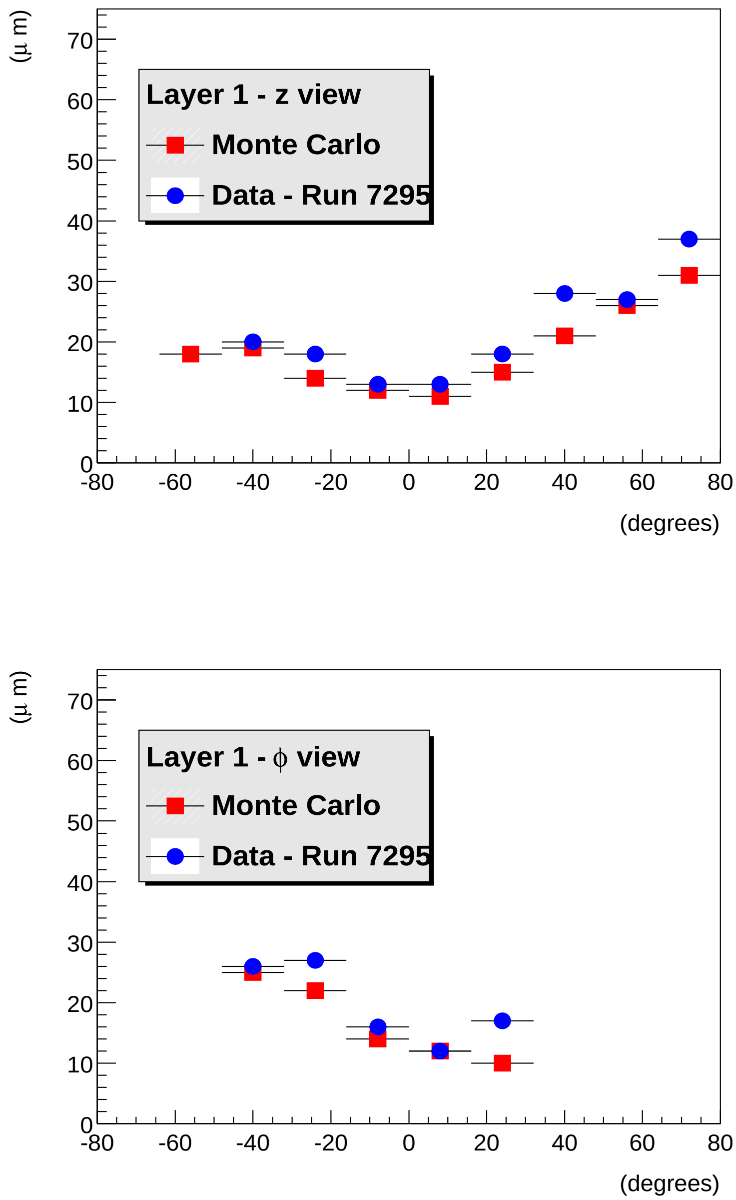

Figure 3.7: *SVT point resolution as a function of the incident track angle for the innermost layer. The agreement with the Monte Carlo is significant since a perfect alignment is assumed during the simulation process.*

the design goals.

3.2.2 The drift chamber

3.2.2.1 Overview

The drift chamber (DCH), in addition to being the main tracking device, also provides one of the principal triggers for data taking. Furthermore, by measuring the development of pulse height in individual cells and converting this information into a measurement of deposited energy, it is also possible to extract $\mathrm{d}E/\mathrm{d}x$ information, making the DCH a useful particle identification device. A detailed description of the DCH design can be found in [27].

3.2.2.2 Detector layout

The DCH (Figure 3.9) is a 2.8 m long cylinder, the inner and outer radii of which are 23.6 cm and 80.9 cm respectively. Due to the asymmetric beam energies of the PEP-II collider, the DCH was designed to minimise the material in the forward direction and is positioned asymmetrically about the interaction point.

The low-mass gas mixture used in the DCH consists of helium (80%) and isobutane (20%). Water vapour is present at 3000 ppm to prolong the life of the chamber. A low mass gas mixture is favourable in order to minimise multiple scattering. The sense wires are 20 μm gold-plated tungsten-rhenium while the field wires are 120 μm and 80 μm gold-plated aluminium. For a track at 90°, the wires and helium-isobutane gas mixture contribute a total of 0.3% radiation lengths.

Drift cells are arranged in 10 superlayers of 4 layers each. Axial and stereo super-

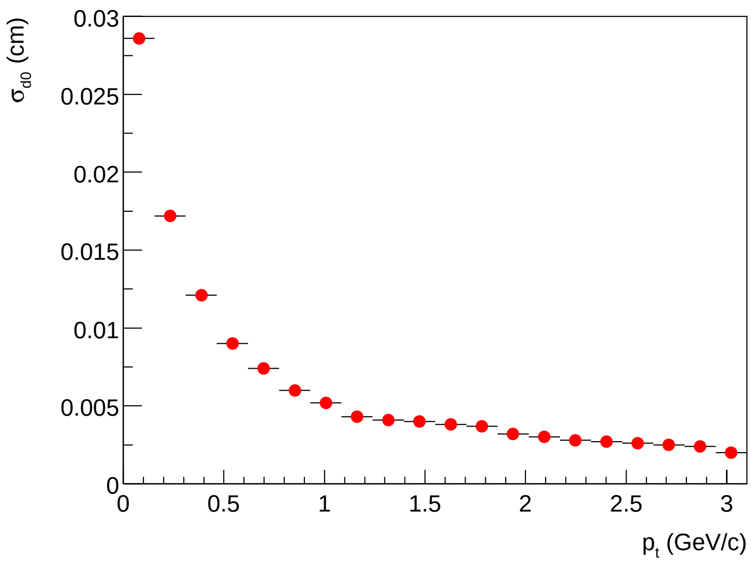

(a) r–ϕ plane

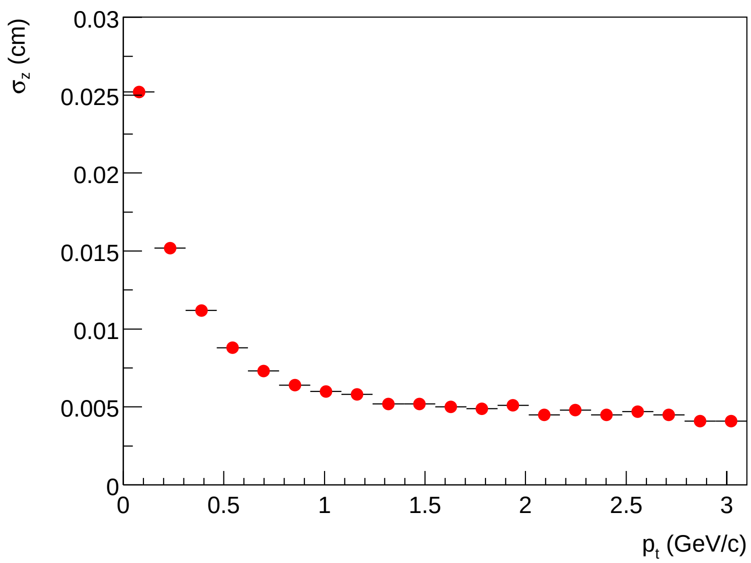

(b) z plane

Figure 3.8: *Impact parameter resolution as a function of track transverse momentum as measured from data.*

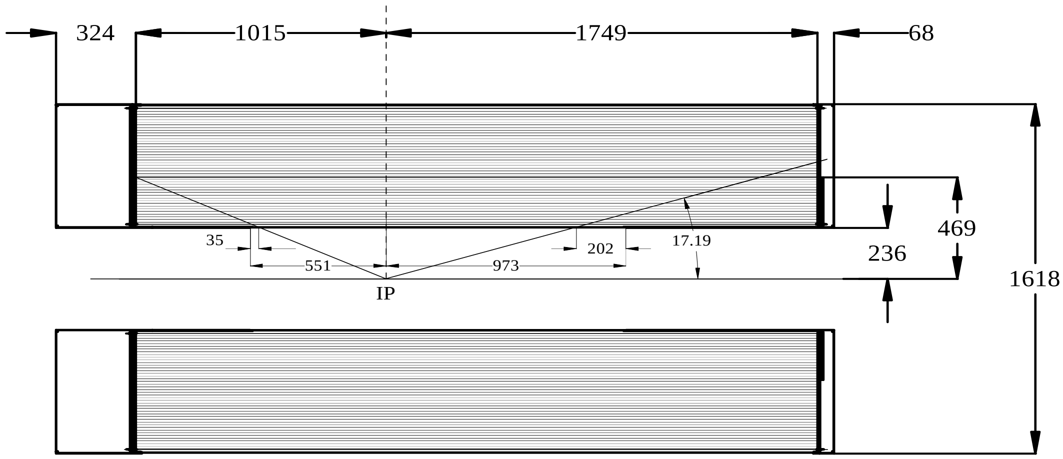

Figure 3.9: *Cross sectional side view of the drift chamber (with dimensions in millimetres). The chamber is positioned asymmetrically about the interaction point, labelled IP in the figure.*

layers alternate following the pattern shown in Figure 3.10. The 7104 hexagonal cells are typically $1.2 \times 1.8\,\mathrm{cm}^2$ in dimension and the stereo angle varies from 40 mr in the innermost stereo superlayer to 70 mr in the outermost superlayer.

3.2.2.3 Electronics and readout

It is essential that the DCH readout system satisfies a number of key requirements. The timing resolution should be sufficient to allow the distance of closest approach of a track to each wire to be determined with a precision better than the inherent chamber resolution. In addition, the charge deposition should be measured with an accuracy compatible with the statistical fluctuations in the formation of the primary clusters.

The DCH amplifier, digitiser and trigger-interface electronics are mounted on the rear end-plate, along with the high-voltage assembly. Locating the electronics at the rear of the chamber keeps the material in the forward direction to a minimum.

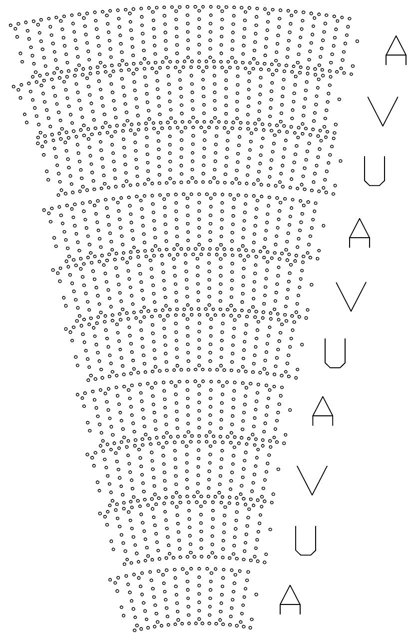

Figure 3.10: *Cell layout in the drift chamber. The superlayers of the chamber alternate in orientation: axial layers (A) are followed by a layer with a small positive stereo angle (U) and then a layer with a small negative stereo angle (V).*

The data from the time-to-digital converters (TDCs) and analogue-to-digital converters (ADCs) are written through a 12 μs trigger-latency buffer into four levels of event buffers in order to minimise dead time. The DCH electronics provide prompt trigger signals; information from all 7104 channels is sent at a sampling frequency of 3.75 MHz to the Level-1 trigger system (Section 3.2.6.2).

Monitoring of the DCH gas system is performed by humidity and temperature sensors; radiation monitors are used to keep track of the integrated radiation dose.

3.2.2.4 Performance

Figure 3.11 shows the single cell resolution for charged tracks; the weighted mean resolution is 125 μm. This compares favourably with the 140 μm average single point resolution required by the chamber design.

Figure 3.12 shows the achieved dE/dx resolution for Bhabha electrons. The observed resolution of 7.5% is slightly higher than the predicted value of 7%, but is expected to decrease as additional corrections — for example, to take into account entrance angle — are applied.

The statistical fluctuations in the formation of primary clusters introduce an average variation of 7% along the length of the track, so that the precision of a few percent on the integrated charge measurement does not degrade the dE/dx evaluation.

3.2.3 The DIRC particle identification system

3.2.3.1 Overview

The DIRC (Detector of Internally Reflected Čerenkov light) is a particle identification system which detects Čerenkov photons trapped by total internal reflection inside a synthetic quartz radiator. The DIRC is designed to provide excellent kaon identification over a wide momentum range. Kaons used for B tagging purposes generally have momentum up to 2 GeV/c, however, if one wants to distinguish between the two-body modes $B^0 \to \pi^+\pi^-$ and $B^0 \to K^+\pi^-$, the DIRC must be able to separate kaons and pions up to 4 GeV/c in the laboratory frame. The DIRC can also assist in muon identification for momenta less than 750 MeV/c, where the

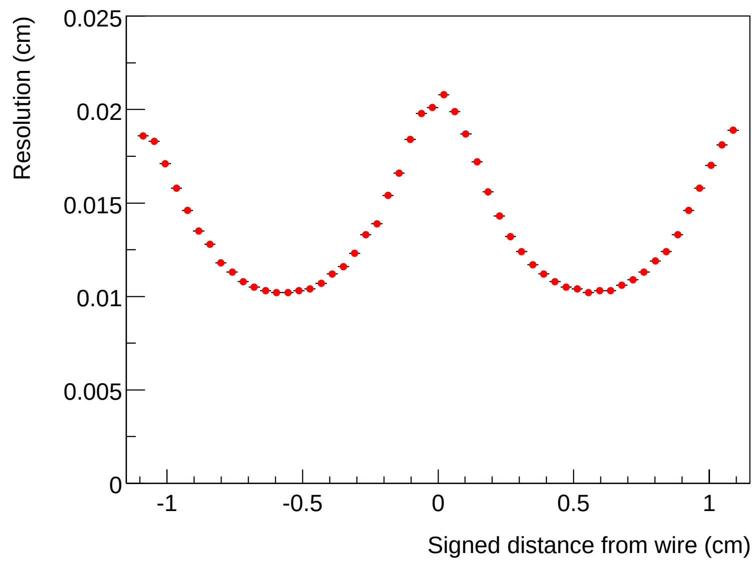

Figure 3.11: *Drift chamber single cell resolution. The weighted mean resolution is 125 μm.*

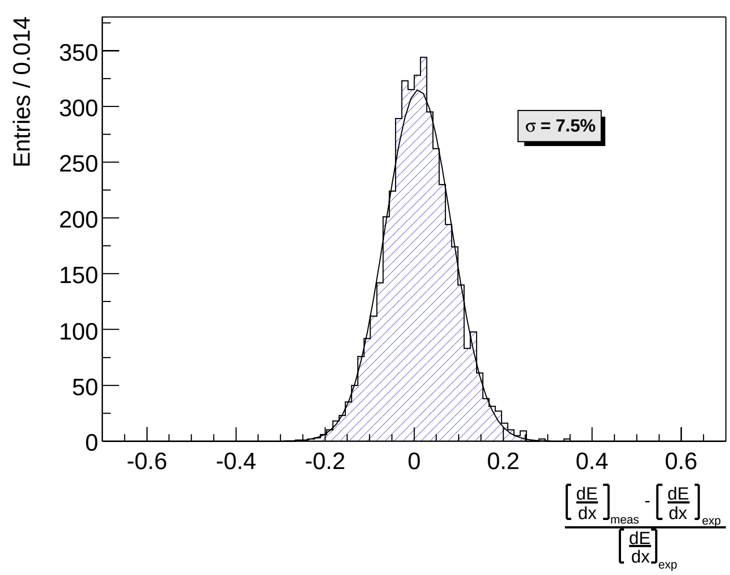

Figure 3.12: *Drift chamber* dE/dx *resolution for Bhabha electrons. The observed resolution in found to be 7.5%.*

instrumented flux return (described in Section 3.2.5) is inefficient.

3.2.3.2 Detector layout

The main components of the DIRC are shown in Figure 3.13. A total of 144 bars of synthetic quartz are arranged in a 12 sided barrel which occupies 8 cm of radial space outside of the DCH. Each bar is 1.7 cm thick, 3.5 cm wide and 4.9 m long. Čerenkov light undergoes a series of internal reflections and eventually emerges from the bars into an expansion medium of purified water which is contained in the 'stand-off box'. Forward-going photons are reflected by a mirror placed at the forward end of the bars as only the rear end of the DIRC is instrumented.

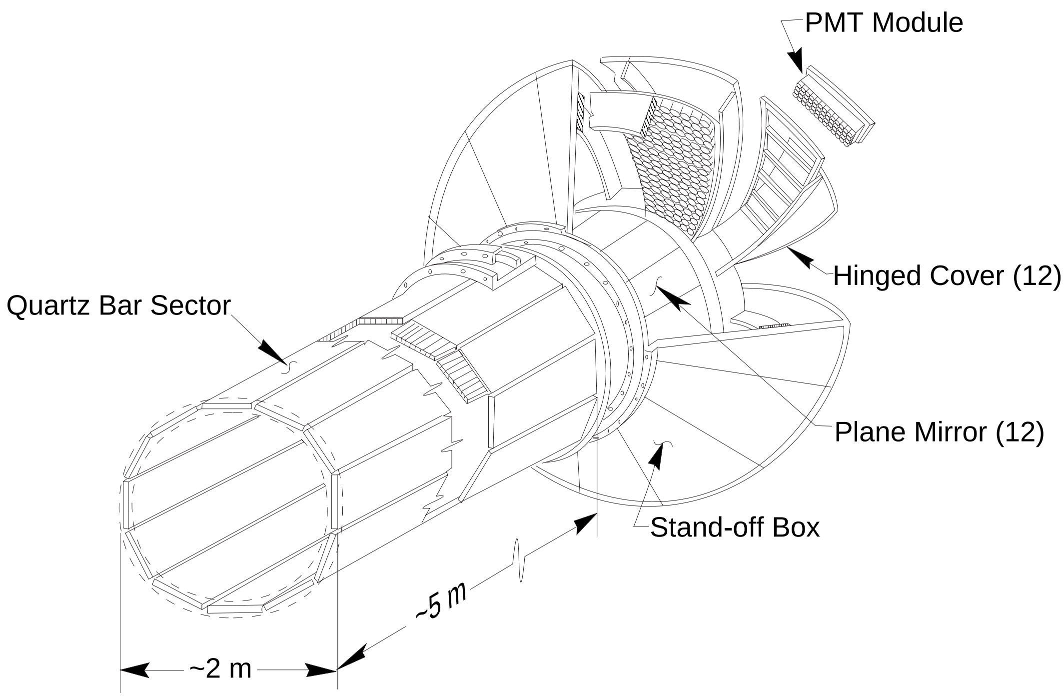

Figure 3.13: *Exploded view of the DIRC particle identification system.*

The Čerenkov angle at which the photon was produced is preserved during the propagation, as displayed in Figure 3.14. The arrival time of the photons, together with pattern recognition, can be used to resolve any ambiguity. Total internal reflection at the quartz-water interface is minimised because the refractive index of the purified water is well matched to that of the quartz.

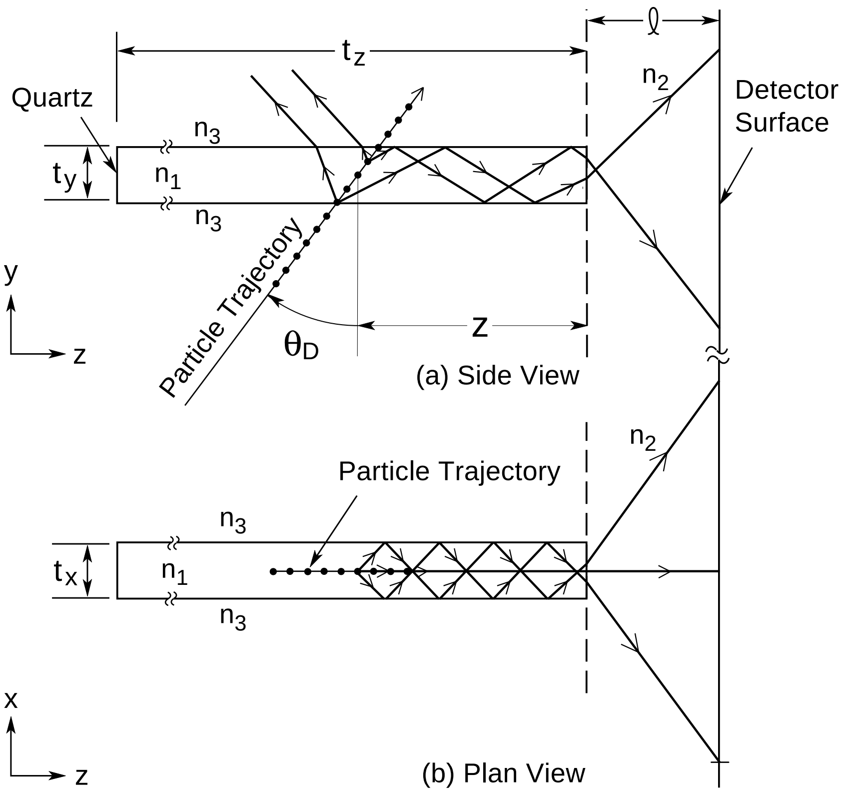

Figure 3.14: *Schematic diagram displaying total internal reflection in a DIRC quartz bar (situated at the top of the DIRC) viewed from (a) the side and (b) the top of the detector.*

Photons in the visible and near-UV range are detected by an array of closely packed 2.82 cm diameter photomultiplier tubes (PMTs) arranged on a roughly toroidal surface. About 11,000 PMTs are needed to cover the detection area, and magnetic shielding around the stand-off box is necessary in order to maintain the magnetic field at a level which is acceptable for PMT operation. Further details of the DIRC concept can be found in [28].

3.2.3.3 DIRC performance

The DIRC technique has many advantages. The radiator bar boxes occupy only 8 cm of radial space, making a relatively large volume available for the DCH, whilst keeping the volume (and therefore the cost) of the electromagnetic calorimeter at a reasonable level. For a particle at normal incidence, the material of the DIRC corresponds to 14% of a radiation length. In addition, the material of the radiator bars is situated close to the front face of the electromagnetic calorimeter so that the impact on calorimeter performance is minimised. The fact that DIRC performance increases with steeper angles of incidence — more light is generated and contained at steeper angles — is particularly desirable at an asymmetric B factory.

The angular resolution for a single photon is about 10.2 mr. For 30 photons per track, the per track resolution is about 2.8 mr, corresponding to an approximate separation of three standard deviations between charged K mesons and pions at 3 GeV/c. The time of a photomultiplier 'hit' is measured with a precision of 1.7 ns, sufficient to effectively suppress background photons and invalid photon solutions.

3.2.4 The electromagnetic calorimeter

3.2.4.1 Overview

The physics requirements of *BABAR* and in particular the requirement to detect photons down to energies around 20 MeV, led to an electromagnetic calorimeter (EMC) design [29] based on CsI crystals doped with thallium iodide at 1000 ppm. The properties of CsI(Tl) are summarised in Table 3.5. The angular coverage of the calorimeter corresponds to $-0.775 \leq \cos\theta \leq 0.962$ in the laboratory frame and $-0.916 \leq \cos\theta \leq 0.895$ in the center of mass frame. Shower leakage from the forward and backward edges somewhat reduce the useful physics coverage of the electromagnetic calorimeter.

Table 3.5: *Properties of CsI(Tl).*

Property	Value
Radiation length	1.85 cm
Molière radius	3.6 cm
Absorption length for 5 GeV pions	41.7 cm
Density	4.53 g/cm^3
$\mathrm{dE}/\mathrm{d}x\|_{\text{minimum ionising particle}}$	5.6 MeV/cm
Light yield temperature coefficient	0.1%/$^\circ C$
Peak emission wavelength	565 nm
Refractive index at emission maximum	1.79
Decay time	940 ns
Hygroscopic	Slightly
Radiation hardness	10^3-10^4 rad

3.2.4.2 Detector layout

The geometry of the EMC is illustrated in Figure 3.15. The calorimeter consists of a barrel section and a conic endcap which is situated in the forward direction (the direction of increasing z). The barrel section has an inner radius of 91 cm and an outer radius of 136 cm and is located asymmetrically about the interaction point.

The barrel consists of 5760 CsI(Tl) crystals arranged in 48 rows in polar angle θ, each row containing 120 identical crystals around the azimuthal angle ϕ. In an effort to minimise the volume of CsI, crystal lengths change with polar angle θ, taking into account the effect of the boost on the photon energy spectrum.

Crystals in the backward half of the barrel have a length of 16.1 radiation lengths. Towards the forward end of the barrel, crystal lengths increase in steps of 0.5 radiation lengths every seven rows up to a maximum of 17.6 radiation lengths.

Crystals in the barrel section are arranged in 280 modules of 7×3 crystals in θ and ϕ. In the endcap there are 20 modules each containing 41 crystals. The modules are similar in design for both regions, with a honeycomb of 300 μm carbon fibre composite attached to an aluminium 'strongback'.

The 820 crystals in the endcap are arranged in eight θ rings. A ninth inner ring is filled with lead shielding blocks. All endcap crystals are 17.6 radiation lengths, except for those occupying the two inner-most rings, which are shorter by one radiation length due to space limitations.

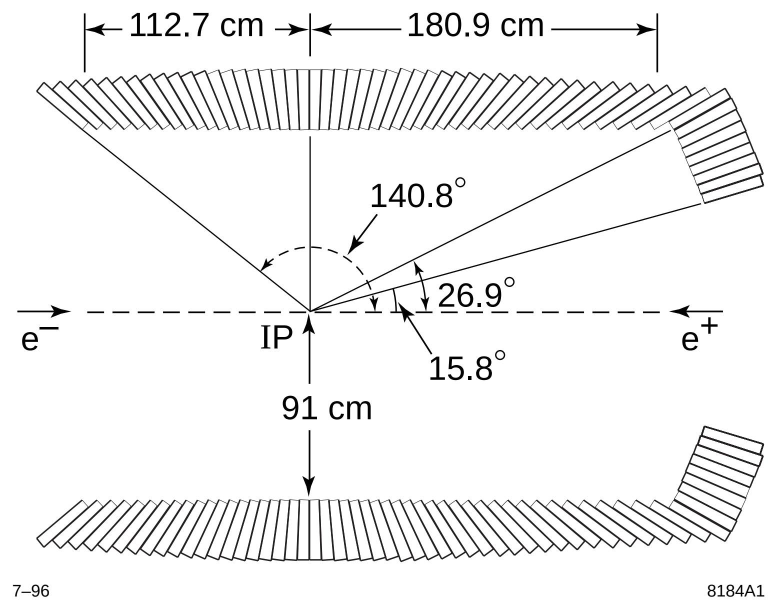

Figure 3.15: *Schematic cross-sectional diagram displaying the dimensions of the electromagnetic calorimeter. The interaction point is labelled IP.*

3.2.4.3 Electronics and readout

The front face and the sides of each crystal are covered with two 150 μm layers of Tyvek † and a 30 μm layer of aluminium foil. Two silicon PIN diodes (on a carrier plate) are glued to the back face of the crystal. The area of the rear face of the crystal surrounding the diodes is covered with a white plastic plate (coated with a reflective paint).

Each diode is connected to its own preamplifier by a 3 cm ribbon cable. The circuit board on which the preamplifiers are mounted is housed in a metal box which rests on the plastic reflector plate and is connected to the aluminium wrapping. Two separate readout diodes are used mainly for reliability reasons, but they also have the effect of increasing the signal to noise ratio.

3.2.4.4 Performance

The target energy resolution of the EMC for photons at a polar angle of 90° is

$$\frac{\sigma_E}{E} = \frac{1\%}{\sqrt[4]{E(\mathrm{GeV})}} \oplus 1.2\%. \tag{3.1}$$

The constant term arises from inter-calibration errors (0.25%), light collection non-uniformity (less than 0.5%) and leakage from the rear (less than 0.5%). The resolution will degrade as the polar angle increases or decreases from 90° as the amount of material in front of the calorimeter increases. Electronics noise is not included in this expression for the resolution.

The target angular resolution, again for a photon at a polar angle of 90°, is

$$\sigma_{\theta,\phi} = \frac{3\,\mathrm{mr}}{\sqrt{E(GeV)}} + 2\,\mathrm{mr} \tag{3.2}$$

† A white reflective material which ensures that as much scintillation light as possible is retained.

and is determined by the crystal size and the average distance from the interaction point to the face of the calorimeter.

The calibration and monitoring system consists of: a charge injection system to linearise the response of the front-end electronics to better than 0.1%, a liquid radioactive source system that uses 6.1 MeV photons from ^{16}N decay and a fibre-optic xenon light pulser system. Signals from data (π^0, radiative and non-radiative Bhabhas, $\gamma\gamma$ and $\mu\mu$ events) provide additional calibration points. Source and Bhabha calibrations are updated weekly to track the small changes in light yield which occur as the integrated radiation dose of the crystals increases. Light pulser runs are carried out daily to monitor relative changes at the $<$ 0.15% level.

The radioactive source system measures an average resolution at 6.1 MeV of σ_E/E = 5.0 $\pm$ 0.8%, while Bhabha electrons at 7.5 GeV give a resolution σ_E/E = 1.9 $\pm$ 0.07%. This implies that the second term from (3.1) which is expected to be of order 1.2% is in fact measured as 2.10$\pm$0.06%. This large constant term is thought to be the result of an as yet uncorrected coherent effect from cross-talk in the front-end electronics. The value calculated from data for the energy dependent term of (3.1) is in agreement with the expected value.

The average light yield per crystal is 7300 photo-electrons per MeV. In the absence of colliding beams, an electronic noise energy of approximately 250 keV per crystal has been measured with the source system after digital signal processing. For detection of photons with energy greater than 20 MeV, the efficiency of the calorimeter exceeds 96%.

3.2.5 The instrumented flux return

3.2.5.1 Overview

The outermost sub-detector, the instrumented flux return (IFR), serves as the flux return for the 1.5 T super-conducting coil and as a support structure for the rest of the BABAR detector. The instrumentation is in the form of resistive plate chambers (RPCs), which provide a means of muon identification and neutral hadron detection. The IFR, a cutaway view of which is displayed in Figure 3.16, is 6.35 m in length, 5.84 m in height and 6.75 m in width. The inner surface of each of the six sextants that make up the barrel section is at a radial distance of approximately 1.70 m from the beam line. A detailed description of the IFR design can be found in [28].

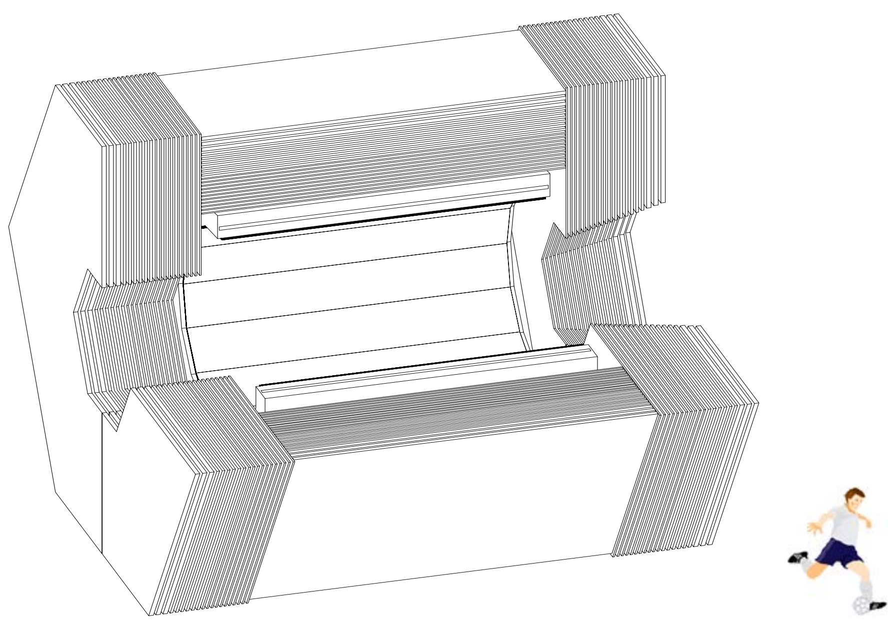

Figure 3.16: *Cutaway view of the instrumented flux return.*

3.2.5.2 Detector layout

The IFR consists of a barrel section and two (one forward and one backward) endcaps. An additional component, the inner RPC, is considered part of the IFR even though it is situated inside the coil.

The barrel section of the IFR is constructed from sextants which are 1.88 m in width at the inner surface, and 3.23 m in width at the outer surface. Each sextant extends 1.28 m outwards. The IFR endcaps are hexagonal in section and are split vertically so that they can be separated in order to allow access to the inner sub-detectors. The solid angle coverage of the endcaps extends down to 300 mr in the backward direction and 400 mr in the forward direction.

The IFR barrel consists of alternate layers of iron (18 layers) and RPCs (17 layers) in a graded design. A further two layers of RPCs inside the coil and one additional layer of RPCs in front and one outside of the iron, bring the total number of layers of active detectors in the barrel region to 21. Each endcap has 18 RPC detector layers, the first of which is behind the innermost layer of iron. The thickness of the iron layers is graded such that the instrumentation layers are more densely concentrated at smaller radial distances from the beam line. The first innermost nine iron plates are 2 cm thick, the next four are 3 cm thick and the next three are 5 cm thick. A final two layers, each 10 cm thick, bring the total depth of material for the barrel to 65 cm. The total depth of iron in each endcap is 60 cm since the penultimate layer of iron in each endcap is 5 cm thick.

3.2.5.3 Resistive plate chambers

Each layer of a barrel sextant houses three RPC modules, so that the barrel section of the IFR contains 342 RPC modules. Similarly each half of an endcap houses three RPC modules in each layer (another 216 modules). The RPC modules housed inside the coil are of a different design — each module is one quarter of a cylinder of radius 1.47 m. A total of 32 modules are arranged in two layers which are rotated through 30° relative to one another so that the joins between modules in the inner layer are not aligned with joins between modules in the outer layer.

Figure 3.17 shows a cross section through a *BABAR* RPC. The gas contained within the chamber is a mixture of isobutane (4.5%), argon (56.7%) and freon (38.8%). Two plates of 2 mm Bakelite coated with graphite form electrodes. The electrodes are covered with PVC insulation, and one is raised to a high potential (7.6 kV), whilst the other is connected to ground. The electrodes are maintained at constant separation by PVC spacers which form a 10 cm grid.

A charged particle traversing an RPC gap produces a quenched spark, which is detected on external aluminium pickup electrodes. The discharge (of order 100 pC) is very fast. The pulse rise time is around 2 ns and the duration is typically around 20 ns.

The aluminium pickup strips on either side of the chamber are arranged orthogonally so as to provide a three-dimensional position. Strips in the barrel have a pitch of 38.5 mm for measuring z and 19.7 mm to 33.5 mm for measuring ϕ. In the endcaps, the strip pitches are 38.0 mm and 28.4 mm for the measurement of x and y coordinates respectively.

The pickup strips are connected to 16-channel front-end readout cards (FECs). Adjacent strips are read out by different cards so that in the case of a card failure there are no dead areas. Two FECs signal off-detector time-to-digital converter (TDC) circuits to deliver timing information for the active strips, which is then employed in the trigger.

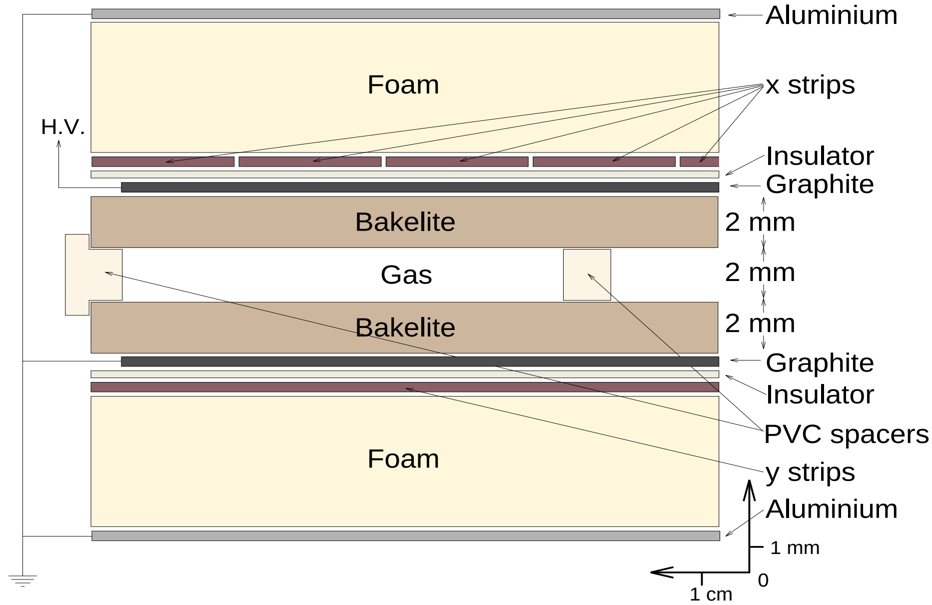

Figure 3.17: *Cross section through a resistive plate chamber. Within the IFR, a total area of approximately 2000* m^2 *is instrumented with RPCs.*

3.2.5.4 Performance

RPC efficiencies are measured in collision data and in cosmic ray runs which are taken weekly. The average chamber efficiencies are 78% in the barrel and 87% in the endcaps. These figures are lower than design values and values achieved in early testing of the RPCs (when efficiencies greater than 90% were achieved). An investigation into the poorer than expected performance is under way.

3.2.6 The trigger system

3.2.6.1 Overview

The *BABAR* trigger is responsible for selecting interesting physics events, which will subsequently be processed and written to the datastore. If competitive physics measurements are to be made, it is essential that a high efficiency is achieved and that this efficiency is well understood.

The *BABAR* trigger consists of two 'levels'. The Level-1 (hardware) trigger is designed to select candidate physics events at a rate of no more than 2 kHz, the maximum rate allowed by the data acquisition system. The Level-3 (software) trigger uses more complex algorithms (after event construction) to reduce the event rate to no more than 100 Hz, the maximum rate that the event processing farm and mass storage facility can tolerate.

3.2.6.2 Level-1

The Level-1 trigger consists of the drift chamber trigger (DCT), calorimeter trigger (EMT) and global trigger (GLT). The DCT and EMT construct 'primitive objects' which are then combined by the GLT to produce a whole range of 'trigger lines'. A Level-1 accept is generated if a GLT trigger line is active for a particular beam crossing. This accept signal must be distributed to the sub-system data acquisition systems with a latency of no more than 12 μs.

The main DCT primitive objects are 'short' and 'long' tracks, corresponding to tracks with a transverse momentum, $p_t >$ 120 MeV/c and $>$ 150 MeV/c respectively. In the case of the EMT, the basic trigger object is a 'tower', corresponding to three adjacent rows of crystals along the length of the calorimeter. A detailed description of the Level-1 trigger objects can be found in [30].

To allow cross-calibration of efficiencies for the EMT and DCT, the Level-1 trigger system is designed to be able to trigger independently from pure DCT and EMT triggers for most physics channels. $B\overline{B}$ events, for example, are triggered at greater than 99% efficiency from either the EMT or DCT. The combined efficiency for EMT and DCT triggers is greater than 99.9%. Tau and two-photon events are the exception, and rely mainly on DCT triggers.

In order to keep the Level-1 trigger rate at a practical level, it is necessary to 'pre-scale' some of the GLT trigger lines. The pre-scale factor determines what fraction of the accepts for a particular trigger line are logged, ensuring that processes with large cross sections, such as Bhabhas, do not dominate the data.

3.2.6.3 Level-2

Although no Level-2 trigger exists at present, future upgrades of the PEP-II collider could result in a situation in which the Level-1 trigger output rate is greater than the allowed 2 kHz. In this scenario, the implementation of an additional (Level-2) trigger system would be necessary in order to produce an event rate suitable for input to the Level-3 trigger.

3.2.6.4 Level-3

The Level-3 trigger consists of a set of software algorithms designed to reduce backgrounds while retaining physics events. In order to achieve the reduction in rate, the Level-3 algorithms use complete events rather than the elementary trigger objects constructed at the hardware level (Level-1) of the trigger.

For example, timing information is used to separate physics events from neighbouring bunch crossings and impact parameters are used to veto events which do not originate from the primary vertex. Level-3 'decisions' are based on generic track-cluster topologies rather than the identification of individual physics processes.

The Level-3 trigger does not significantly reduce the efficiencies delivered by the hardware trigger, but it is necessary to pre-scale Bhabha and two-photon events which have a total rate of approximately 200 Hz at design luminosity. A sample of Bhabha events, uniform in θ, are logged for calibration purposes. Additional samples of events along with some random triggers are also preserved for the purpose of calibration and monitoring.

4

BaBar software

Simulation, reconstruction and data-analysis software form an integral part of any modern high energy physics experiment. This chapter gives a summary of the main elements of the *BaBar* software, concentrating on the components which are of particular relevance to the analysis presented in this thesis.

4.1 The C++ programming language

BABAR software is written almost exclusively in the C++ object-oriented programming language. C++ was chosen over other object-oriented programming languages after consideration of the availability and cost of compilers, support for different platforms, development and debugging tools and interfaces to databases. A key point in the decision to use an object-oriented language for the experiment lay in the expected size of the project, $\mathcal{O}(10^6)$ or more lines of code. As a program grows in size and complexity, the design and structure of the code becomes more important than the programming language itself. By choosing to code a project in an object-oriented language, one can often minimise the increase in complexity with growing program size. Examples of how this can be achieved, with C++ in particular, are illustrated in the following sections.

4.1.1 Object-oriented programming

In object-oriented programming, the relationship between data and the operations which are performed on those data is emphasised. An object is an instance of a set of data and methods, collectively known as a *class*. Object-oriented languages are conducive to programs arranged around the defined data types which specify precisely which operations may be performed. This is not the case with structured programming languages, in which programs tend to be organised around code rather than data.

4.1.2 Inheritance

Because of the way that the C++ programming language facilitates code sharing and reuse, it is particularly effective in coding large projects. An important feature of C++ is that a new class is allowed to *inherit* from an existing one. The derived class may then build on the original class by reusing part or all of its functionality. Moreover, the original (inherited) methods can be overridden to provide an alternative implementation. Thus, through the use of classifications, it is possible for a class to inherit from a general base object and define only those qualities which make it unique within its classification.

4.1.3 Encapsulation

Encapsulation is the mechanism by which data and the methods which act on that data, are bound together and kept separate from other code. By linking together data and functions in this way, we are creating an object. Typically, the representation of the data within an object will be 'hidden' from external code. That is, client code which exists outside of the object is not allowed to access the object's *private* data. It is also possible for methods to be private to an object. It is usual to define public parts of an object which act as a controlled interface to the members of the object which are private. This philosophy has two main benefits, both of which are particularly important for large projects with many developers. First, private data are safe from outside interference and misuse. Second, client code is not dependent on the representation of data within an object (or any private methods). As long as the interface remains the same the two pieces of code remain compatible.

4.1.4 Polymorphism

Polymorphism is a feature of object-oriented programming which helps to reduce complexity by allowing the same interface to be used to access a general class of actions. One way in which C++ achieves polymorphism is through the use of function overloading; two or more functions are allowed to share the same name, as long as the arguments of the overloaded functions vary in type or number (or both). Function overloading is useful in situations when, for example, an equivalent operation is to be performed on variables of different data types.

Polymorphism can also be achieved as a result of inheritance (if a function defined for a parent class is also defined for a derived class) and in the case of templated classes [31].

4.2 Simulation

4.2.1 Event generators

The data simulation process for *BABAR* begins with the generation of 4-vectors (representing the products of a particular process) using one of a number of possible event generation programs. Before they are used in the simulation process, the beam energies are smeared using a Gaussian of width 5.5 MeV for the high-energy beam and 3.1 MeV for the low-energy beam. Gaussian distributions of width 160 μm and 6 μm are used to smear the x and y coordinates of the interaction point respectively. The z coordinate is modelled as a flat distribution, 1 cm in length.

Tau-pair production and τ decay are modelled by `KORALB` [32] and `TAUOLA` [33] respectively. The TAUOLA library implements a Kühn and Santamaria model $\pi\pi^0$ spectral function with parameters (shown in Table 4.1) based on one of the fits by Kühn and Santamaria [20] to $e^+e^- \to \pi^+\pi^-$ data. This fit did not allow for a possible $\rho(1700)$ contribution. Since KORALB and TAUOLA are Fortran programs,

Table 4.1: *Parameters used in the modelling of $\tau^- \to \pi^-\pi^0\nu_\tau$ decays during Monte Carlo generation. Units for all masses and widths are MeV/c^2.*

Parameter	Value
M_ρ	773
Γ_ρ	145
β	-0.145
$M_{\rho'}$	1370
$\Gamma_{\rho'}$	510

additional code is necessary to interface them to the *BABAR* C++ software framework. Generated 4-vector 'events' must be processed by additional software to simulate interactions with the material of the detector.

4.2.2 Detector model

The *BABAR* detector simulation package, BBSIM [34], is based on the CERN detector description and simulation tool, GEANT3 [35]. GEANT3 provides tools to construct the detector geometry, to simulate the interactions and decays of each particle species and to display detector components, particle trajectories and track hits. Output from BBSIM includes generator-level and GEANT3-level Monte Carlo truth along with any particle 'hits' recorded for the active detector components. Each 'hit' contains information (such as particle position, direction and Monte Carlo track number) needed to perform a detector response simulation.

4.2.3 Detector response simulation and reconstruction

Simulation of detector response and addition of background hits is performed by the `SIMAPP` program [34]. The 'hits' resulting from the detector modelling are converted to digitised data in the same format as output from the real detector.

In order to produce a realistic level of background in the detector, background hits are extracted from data rather than being simulated. Hits are added to the Monte Carlo events by mixing in data from random triggers. A simulation production block corresponds to approximately one month of event generation, so care must be taken to ensure that fluctuations in machine background are considered. The background events obtained from the data are shuffled to ensure that even small Monte Carlo samples have background hits representative of running conditions throughout the month. Finally, event reconstruction is performed by the `BEAR` program [36] and output written to an object database ready for use in data analysis.

4.3 Online prompt reconstruction

In the case of real data, output from the data acquisition system is processed automatically by a Unix compute farm. All colliding beam events are 'filtered' (to remove background events) and possibly 'tagged' (indicating that they are candidates for a process of interest for a particular physics analysis). Interesting events are written out to an object database. Information on which filter was passed, and which 'tag bits' were set are made available for off-line analysis of the event. The reconstruction executable, `ELF`, closely resembles the `BEAR` program [36] which is used for the reconstruction of simulated data. Additional code allows prompt reconstruction to control the job and provides a means for reading data files of the format written by the data acquisition system.

The online prompt reconstruction system is designed to keep up with data acquisition with minimum latency. Typically, data will be processed within a day of being logged.

5

Electron control sample for particle identification

One important aspect of particle identification is the testing of algorithms for efficiency and purity. Monte Carlo data are useful to an extent, but control samples extracted from real data must be used if a realistic assessment of performance is to be obtained. In producing such a control sample it is of course important that candidate particles are selected from the data without the use of the particle identification routines to be tested. This is important if we hope to achieve an unbiased measure of the performance of an algorithm.

5.1 Motivation for producing the sample

The identification of electrons [†] is of crucial importance, not only for the studies of semileptonic charm and beauty decays, but also for the tagging of B decays. Well-calibrated electron selection algorithms also play a role in the analysis presented in this thesis. The single prong decay of the τ to an electron can provide a useful 'tag' for τ-pair events; the branching fraction for $\tau^- \to e^- \bar{\nu}_e \nu_\tau$ is $\sim$ 17%. Tau-pair event tagging is discussed further in Section 6.2.4.

While the identification of high energy electrons is fairly straightforward, identifying electrons for flavour tagging is more difficult, and requires a high purity and high efficiency over a wide momentum range. Figure 5.1(a) illustrates how the momentum distribution of leptons from $b \to c$ transitions is peaked at 1.5 GeV/c in the centre of mass system, while the distribution for leptons produced by the cascade of c quarks is peaked at 0.5 GeV/c. The momentum spectrum for electrons from τ decays is shown in Figure 5.1(b).

Bhabha events provide a large sample of electrons with momenta typically greater than 3 GeV/c. At the low end of the momentum spectrum, photon conversions can be utilised in order to produce a pure electron sample with a mean momentum of approximately 300 MeV/c. The two photon process $e^+e^- \to e^+e^-e^+e^-$ provides a sample of electrons at intermediate momenta (typically 0.5–1 GeV/c). This region of the momentum spectrum is particularly important for electron identification as it corresponds to the region of interest for flavour tagging with *BABAR*.

[†] Electron is used to refer to both particle and antiparticle unless otherwise stated.

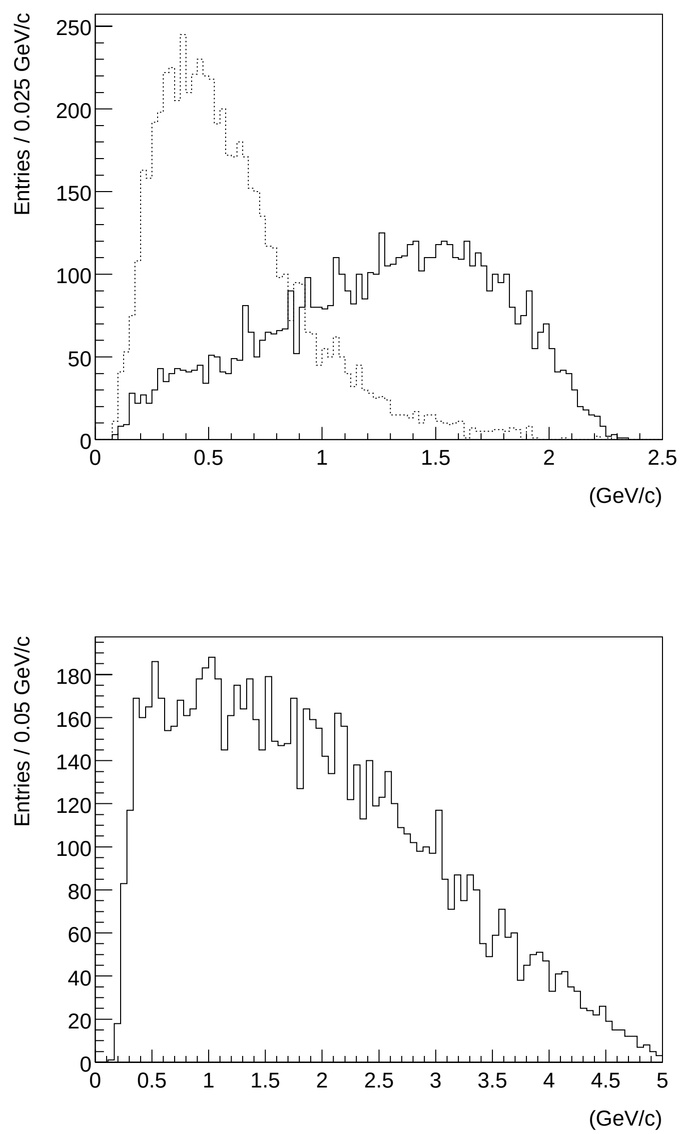

Figure 5.1: *Monte Carlo simulation of lepton momentum in the centre of mass system for (a) leptons produced by $b \to c$ transitions (solid line) and by the cascade decays of c quarks (dotted line) and (b) for electrons from τ decays.*

5.2 Event properties

At the lowest order, the two-photon process $e^+e^- \to e^+e^-e^+e^-$ is a pure $\mathcal{O}(\alpha^4)$ QED reaction and is therefore, in principle, well understood. The four main diagrams contributing at the lowest order are displayed in Figure 5.2 [37]. The classical 'two-photon' diagram is the one labelled multiperipheral. The permutations arising due to the four electron final state result in 36 Feynman diagrams contributing in total. All 36 diagrams are displayed in [38]. Although all four diagrams are included in the Monte Carlo simulation, for the class of events of interest in this study (two final state particles within the acceptance of the detector) the cross section is dominated by the multiperipheral diagram [39].

In the multiperipheral case, as a consequence of the fermion propagator and the fact that the photons are very close to the beam direction, the angular distribution of the electrons in the $\gamma\gamma$ centre of mass system is highly peaked in the forward and backward directions (with the angle with respect to the beamline $\sim$0° or $\sim$180°).

If W is the invariant mass of the $\gamma\gamma$ pair and m the mass of the fermion in question, then the differential cross section is given by [40]

$$\frac{\mathrm{d}\sigma(\gamma\gamma \to ff)}{\mathrm{d}\Omega} = \frac{\alpha^2}{2W^2}\sqrt{1-\frac{4m^2}{W^2}}G_F(W,\theta), \tag{5.1}$$

where α is the electromagnetic coupling constant and

$$G_F(W,\theta) = 2 + 4\left(1-\frac{4m^2}{W^2}\right)\frac{\left(1-\frac{4m^2}{W^2}\right) sin^2\theta\cos^2\theta + \frac{4m^2}{W^2}}{\left[1-\left(1-\frac{4m^2}{W^2}\right)\cos^2\theta\right]^2}. \tag{5.2}$$

For $W \gg 2m$ we get for $\theta = 90°$

$$G_F(W,\theta) = 2 + 4\left(\frac{2m}{W}\right)^2 \approx 2, \tag{5.3}$$

and for $\theta = 0,\ 180°$

$$G_F(W,\theta) = 2 + 4\left(\frac{W}{2m}\right)^2 \approx \left(\frac{W}{m}\right)^2. \tag{5.4}$$

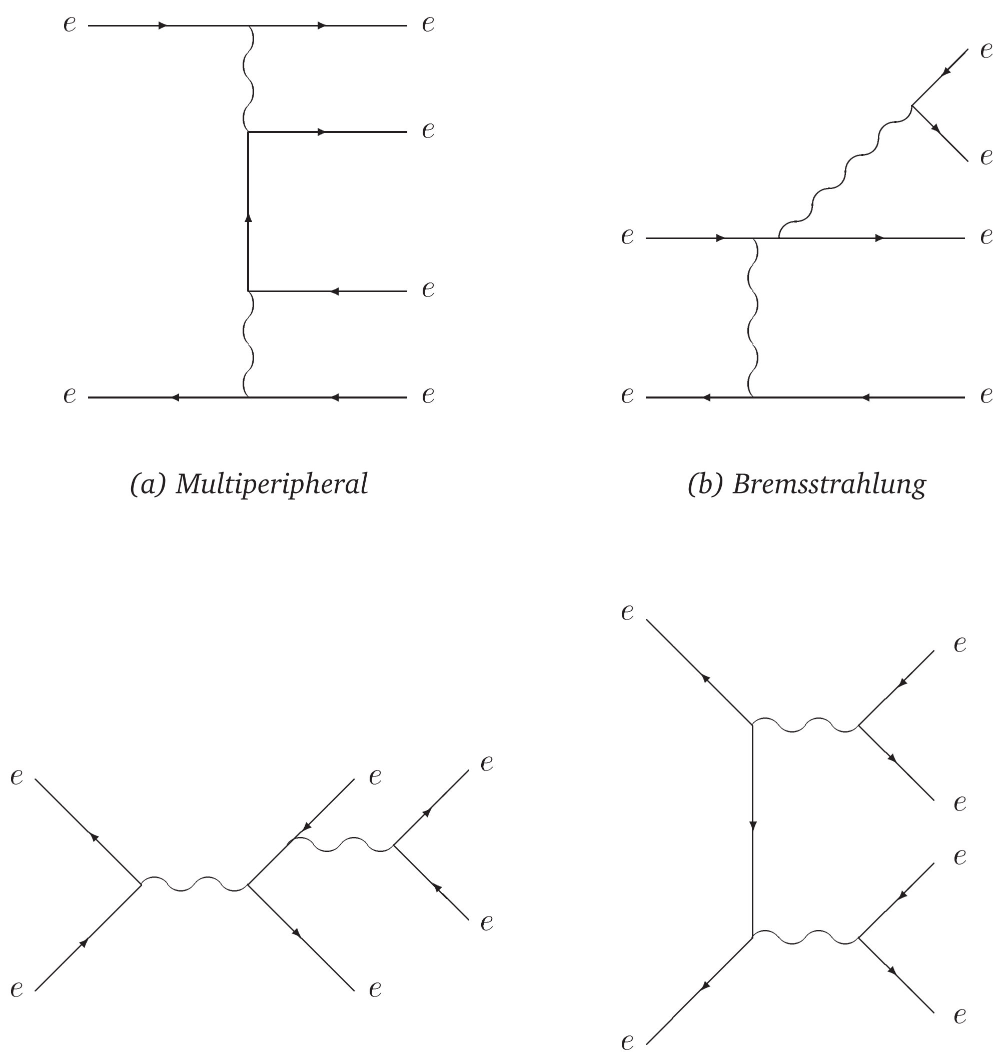

(a) Multiperipheral *(b) Bremsstrahlung*

(c) Annihilation *(d) Conversion*

Figure 5.2: *The four main diagrams contributing at the lowest order to the process* $e^+e^- \to e^+e^-e^+e^-$.

Thus the peak gets more and more pronounced with increasing W.

Characteristic event properties mean that an event selection relying heavily on kinematic variables can be used to identify $e^+e^- \to e^+e^-e^+e^-$ events.

5.3 The Monte Carlo sample

Monte Carlo $e^+e^- \rightarrow e^+e^-e^+e^-$ events are produced with `DIAG36` [41], a Fortran generator which is interfaced to the *BABAR* reconstruction software. Figure 5.3

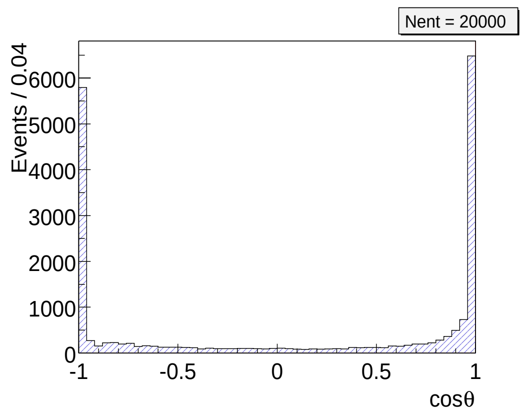

(a)

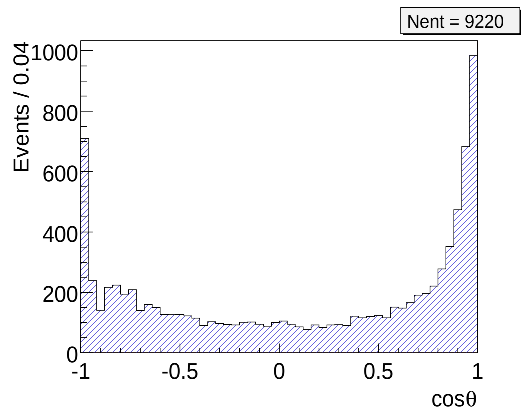

(b)

Figure 5.3: *Angular distribution of tracks from Monte Carlo $e^+e^- \rightarrow e^+e^-e^+e^-$ events; θ is the polar angle in the coordinate system described in Chapter 3. (a) Shows the angular distribution of all generated tracks, (b) shows the distribution only for those tracks with momentum less than 1 GeV/c so that there are no entries due to scattered beam particles.*

shows the angular distribution of the particles in the generated events. Figure 5.3(b) shows the distribution for only the lower momentum particles, illustrating how the high momentum beam particles are scattered at very small angles, giving rise to the large peaks at $\cos\theta$ of $\pm$ 1 in Figure 5.3(a). As described in Section 4.2, the 4-vectors produced by the generator are processed with `BBSIM` (the *BABAR* detector simulation package), and then `SIMAPP` (digitisation simulation) and `BEAR` (reconstruction).

Simulated $e^+e^- \rightarrow e^+e^-e^+e^-$ events are combined with additional Monte Carlo data, taking into account relative production cross sections, in order to produce a generic sample of simulated data suitable for conducting an investigation into possible sources of background.

5.4 Trigger efficiency

After taking into account the limited angular acceptance of the detector, the effective cross section[‡] for $e^+e^- \to e^+e^-e^+e^-$ events at *BABAR* is 10.28 nb. This is over an order of magnitude lower than the total cross section for this process, which is strongly peaked in the forward and backward directions. This effective cross section is further reduced as a result of the Level-1 and Level-3 triggers.

The Level-1 trigger efficiency for $e^+e^- \to e^+e^-e^+e^-$ events, as determined from Monte Carlo, is 38.6%. After taking into account the efficiency of the Level-3 trigger (again determined from simulated events), the overall efficiency for logging $e^+e^- \to e^+e^-e^+e^-$ events is 30.8%.

5.5 Event selection

A control sample which is to be used to test particle identification algorithms must be as pure as possible. The event selection used in producing the control sample is therefore tuned for high purity rather than for high efficiency.

In $e^+e^- \to e^+e^-e^+e^-$ events, the scattered beam electrons usually escape detection as they are at low angles to the beamline. This results in two well separated tracks in an event and little other detector activity. For this reason, in selecting candidate

[‡] As reported by the event generator.

Table 5.1: *Event selection cuts (described in Section 5.5).*

Cut parameter	Event accepted for values
Acolinearity	> 0.1 rad
Acolinearity in centre of mass system	> 0.1 rad
Visible momentum in centre of mass system	< 3.0 GeV/c
Acoplanarity	< 0.05 rad
Magnitude of $\cos\theta_{miss}$	> 0.985

$e^+e^- \to e^+e^-e^+e^-$ events, exactly two reconstructed tracks are required. Further cuts are applied in order to minimise contamination from background events that have a similar topology. A summary of the event selection cuts described below is given in Table 5.1.

Cosmic ray events are vetoed by requiring that the acolinearity — the three dimensional angle between the two tracks — of the event is greater than 0.1 radians in the laboratory frame. By performing the same cut in the centre of mass system (Figure 5.4), a large fraction of the contamination μ-pair events is removed. Figure 5.5 illustrates how requiring the total visible momentum in the centre of mass system to be less than 3 GeV/c removes a significant fraction of the contamination from τ-pairs in addition to much of the remaining μ-pair background.

The direction of the missing momentum in the event provides a strong method of discrimination between $e^+e^- \to e^+e^-X$ (where X is $\ell^+\ell^-$ or γ) events and other events with a similar topology. In $\tau^+\tau^- \to \ell^+\ell^-\nu_\ell\bar{\nu_\ell}\nu_\tau\bar{\nu_\tau}$ events for example, the missing momentum vector arising as the neutrinos escape detection in the detector will not generally be aligned with the beamline. In addition, because the photons are produced at very low angles to the beam particles, the two observed tracks in $e^+e^- \to e^+e^-e^+e^-$ events ought to be back to back in the x-y plane, since the

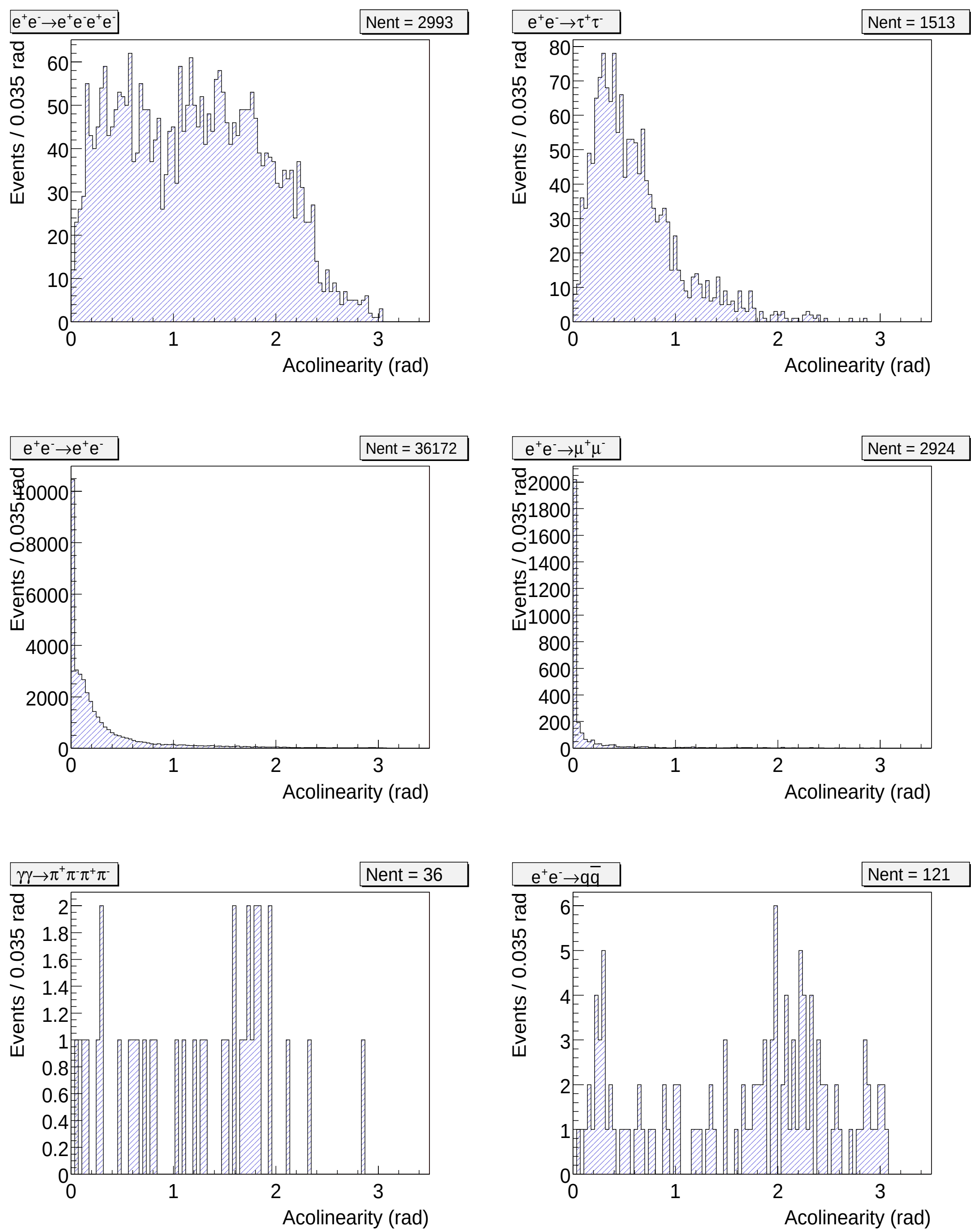

Figure 5.4: *Acolinearity in the centre of mass system for signal and background events.*

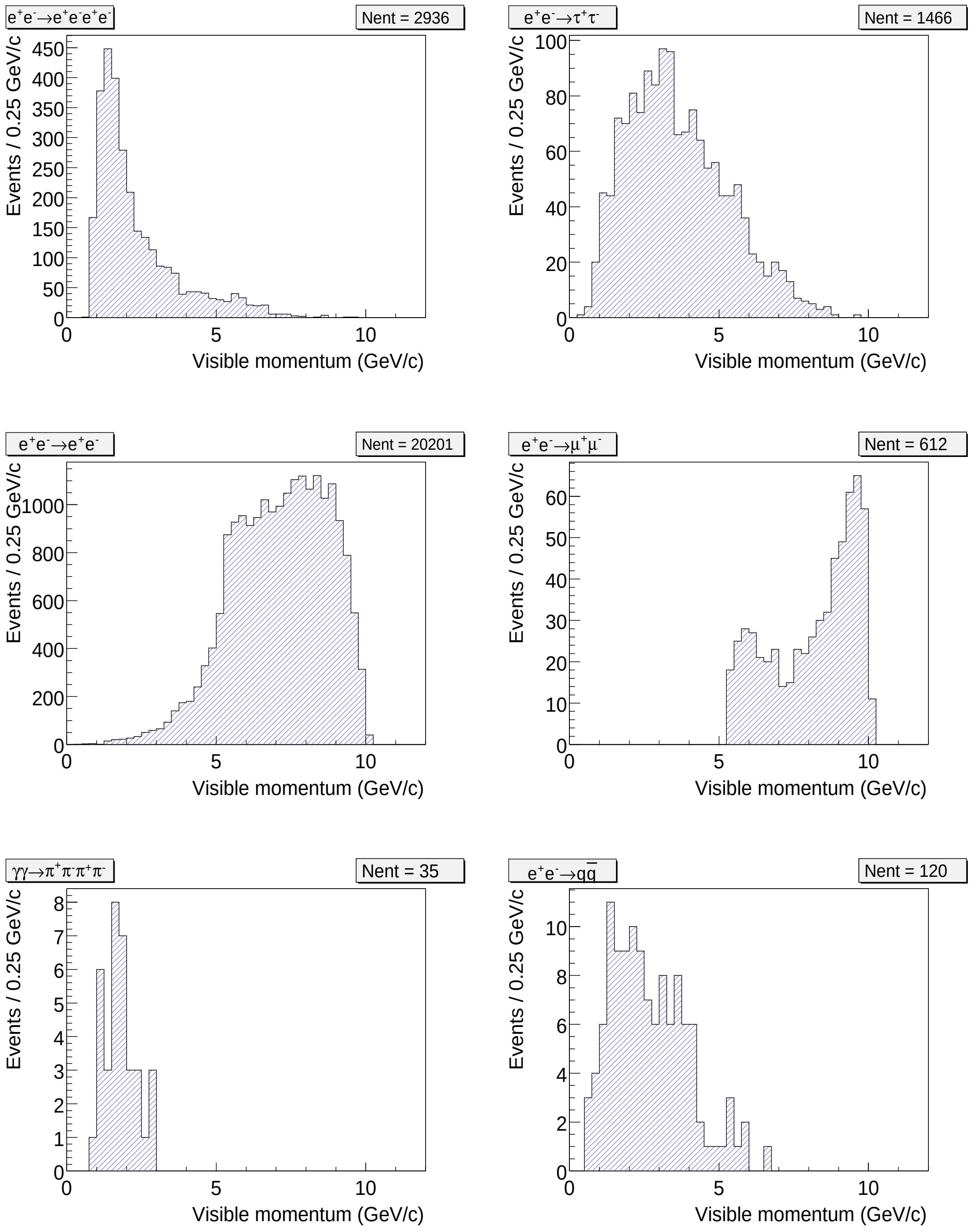

Figure 5.5: *Total visible momentum in the centre of mass system for signal and background events.*

p_t in the event should be balanced. A cut on the acoplanarity[§] of the event in the laboratory (shown for the various event types in Figure 5.6) is used to reject events which don't appear to have balanced p_t.

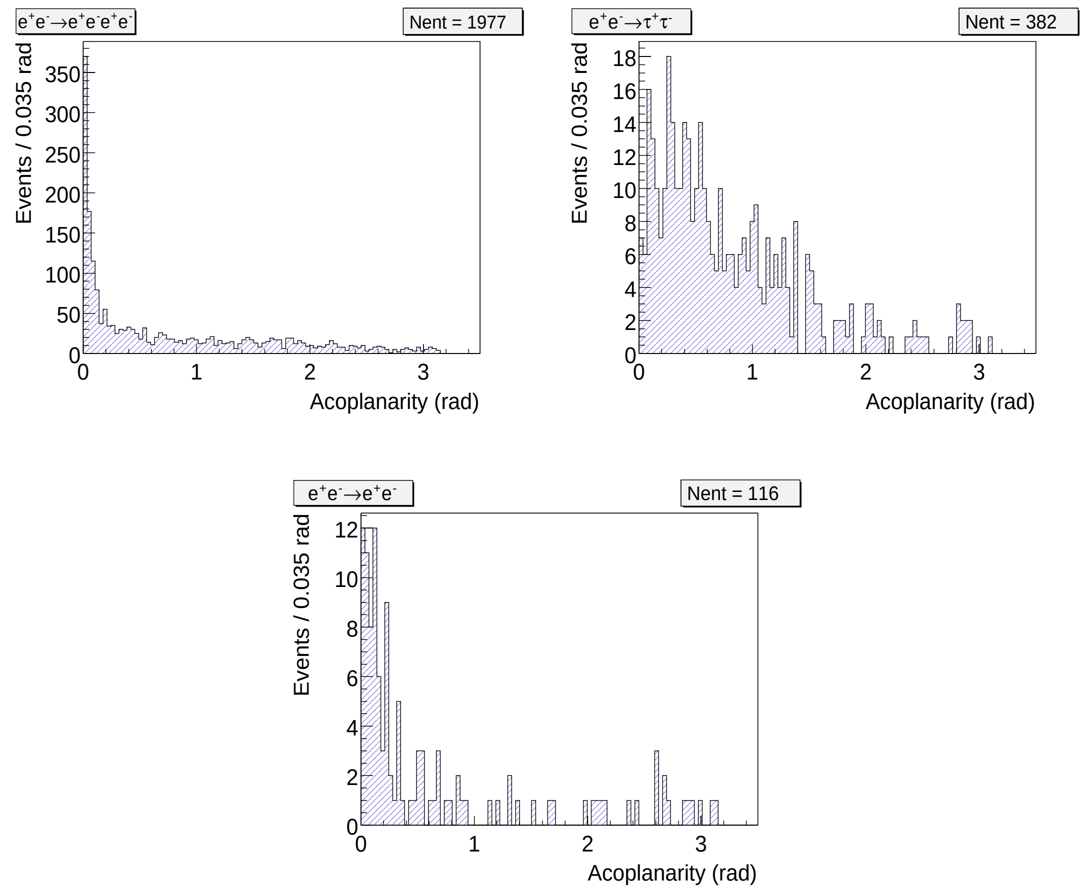

Figure 5.6: *Acoplanarity plotted for signal events and the dominant remaining types of background.*

Figure 5.7 shows $|\cos\theta_{miss}|$ for Monte Carlo $e^+e^- \rightarrow e^+e^-e^+e^-$ events and the remaining background events, where θ_{miss} is the angle of the event missing momentum vector. Events that do not have a missing momentum vector at a low angle to the beamline are rejected by cutting at 0.985.

[§] Defined as $\pi - \phi_{xy}$ where ϕ_{xy} is the two-dimensional angle between the two tracks in the x-y plane.

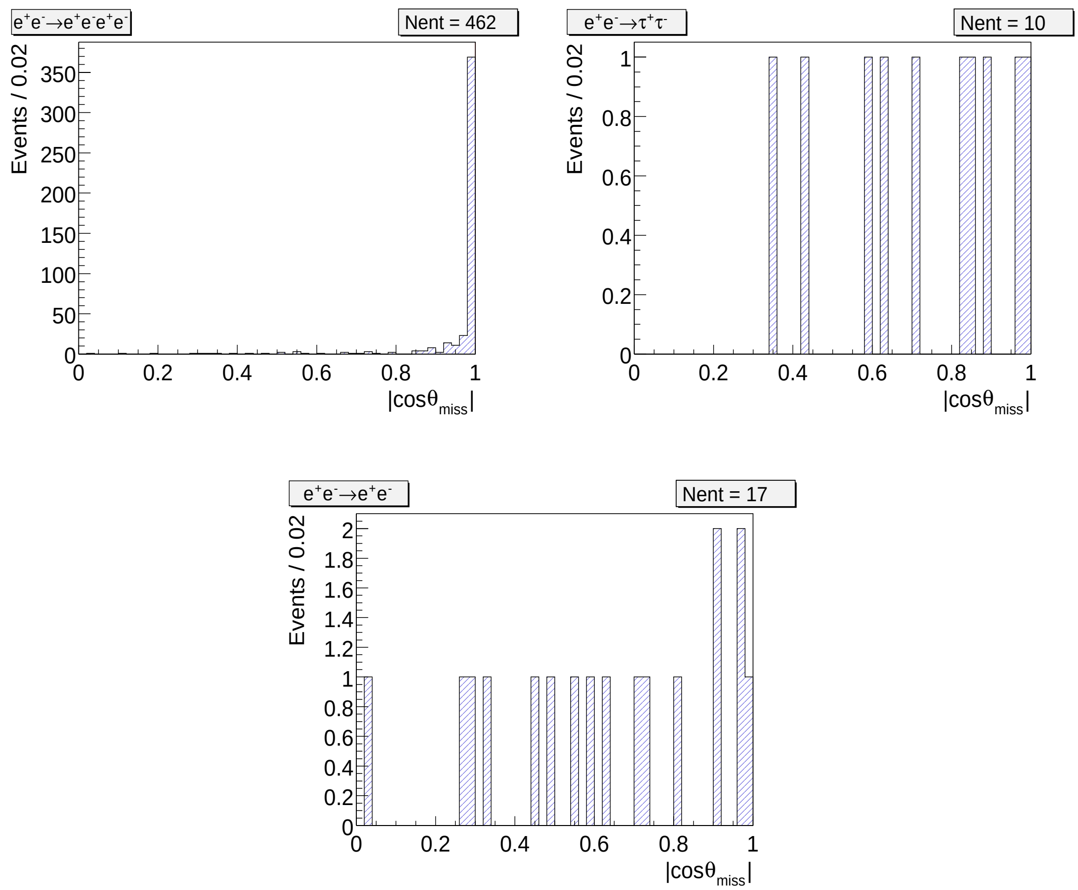

Figure 5.7: *Magnitude of $\cos\theta_{miss}$, where θ_{miss} is the angle of the missing momentum vector for the event with respect to the beam line.*

It is worth noting at this point that no attempt is made to reject $e^+e^- \to e^+e^-\mu^+\mu^-$ events during event selection. Since the kinematics are similar for both $e^+e^- \to e^+e^-e^+e^-$ and $e^+e^- \to e^+e^-\mu^+\mu^-$ events, we have to rely on the individual candidate selection (Section 5.6) to make sure that muons do not contaminate the control sample.

It is also worth noting that the cuts on event properties are necessarily tight; contamination, particularly from τ-pairs, must kept to a minimum. Selection of τ-pair events in which one τ-decay results in an electron, and one τ-decay does not produce an electron will quite likely result in some contamination of the final sample.

Table 5.2: *Electron candidate selection cuts.*

Cut parameter	Event accepted for values
$(\mathrm{dE/d}x)_{DCH}$	> 450
EMC cluster lateral moment†	> 0.1 and < 0.7
E/p	> 0.8
IFR strips hit	Equal to 0

†See Appendix A for details of the cluster lateral moment parameter.

The reason for this will become evident as the electron candidate selection is described in the following section.

The efficiency of the event selection as detailed above is 14.1% and the resulting event sample is 99.1% pure (if the contribution from $e^+e^- \to e^+e^-\mu^+\mu^-$ events is ignored).

5.6 Electron candidate selection

In order to extract an electron control sample from a given set of candidate $e^+e^- \to e^+e^-\ell^+\ell^-$ events, one must be careful not to introduce a bias through the selection criteria. For this reason, pairs of track candidates are considered; if a candidate passes the selection criteria, then the partnering candidate is added to the sample.

An existing cut-based electron selector (details of which can be found in [42]) is used as the basis for the algorithm used to select electron candidates from the $e^+e^- \to e^+e^-\ell^+\ell^-$ events. In order to increase the purity of the sample, the cut on the E/p ratio is tightened from 0.6 to 0.8. The candidate selection cuts defined for the new selector are shown in Table 5.2.

The efficiency of the candidate selection for signal events passing the event selection is 96.1%; the contamination from muons from $e^+e^- \rightarrow e^+e^-\mu^+\mu^-$ events is low, representing less than 0.5% of the final sample. The only other remaining 'contamination' of the sample is a 0.2% contribution of electrons from Bhabha events.

Taking into account the efficiencies of the Level-1 trigger and Level-3 trigger, the event selection and the candidate selection, the overall efficiency for selecting electrons from $e^+e^- \rightarrow e^+e^-e^+e^-$ events is 4.1%. The resulting control sample is over 99% pure.

5.7 Properties of the sample

Particle identification control samples for *BABAR* are produced by the `BetaPidCalib` package [43]. Selection algorithms are added as modules which provide an accept or reject decision for each candidate in an event. In the case of a candidate passing the selection, it is added to the appropriate particle list by the underlying `BetaPidCalib` framework. Control sample lists are produced for e, μ, π, K and p particle types. The study described here resulted in the implementation of such a module, `BtaPideeeeCalibSample`, which is now included as part of the control sample production running.

Various properties of an electron sample produced from *BABAR* data are presented in Figures 5.8, 5.9 and 5.10. The sample was produced from 358 pb^{-1} of data, corresponding to ten days of data taking.

Figure 5.8 shows the momentum distributions for selected electron and positron candidates. The distributions are peaked about 1 GeV/c, providing candidates in

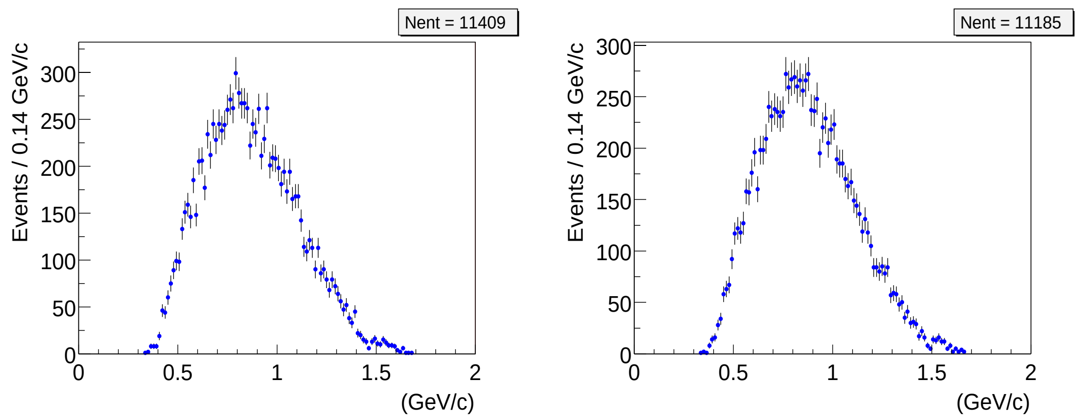

(a) Electron candidates *(b) Positron candidates*

Figure 5.8: *Momentum distribution in the centre of mass frame for selected candidates.*

the important intermediate momentum range (described in Section 5.1). As expected there are no significant differences between the two distributions.

The distribution of the selected candidates in polar angle in the laboratory frame is displayed in Figure 5.9. The angular distribution of the candidates is clearly

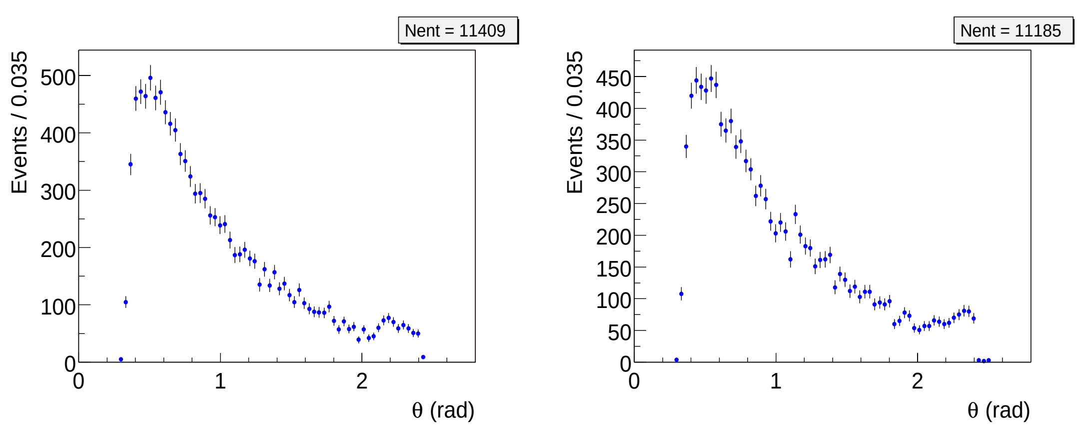

(a) Electron candidates *(b) Positron candidates*

Figure 5.9: *Theta distribution (in the laboratory frame) of selected candidates.*

peaked in the forward direction as expected.

The E/p distributions for electron and positron candidates from the control sample are shown in Figure 5.10. Again, the distributions for positively and negatively

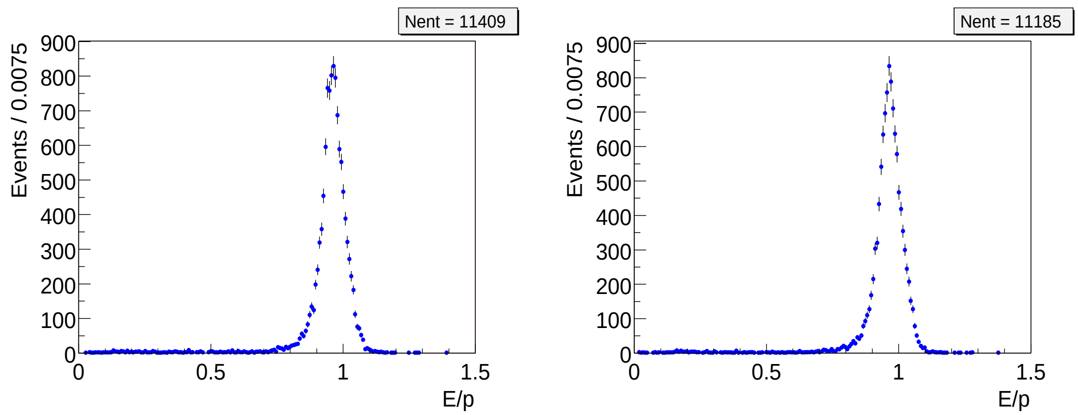

(a) Electron candidates *(b) Positron candidates*

Figure 5.10: *E/p distributions for selected candidates.*

charged candidates are similar. Peaking near unity, the distributions are consistent with resulting from a high purity sample. The fact that the peak is at a value slightly less than unity can be attributed to energy leakage from the back and edges of the calorimeter. Values of E/p greater than unity are possible if a high energy electron emits a bremsstrahlung photon in the inner detector. If the energy deposit in the calorimeter resulting from the photon is merged with the electron shower, it is possible that the resulting E/p ratio will be greater than unity.

5.8 Summary

A cut-based selection algorithm was added to the `BetaPidCalib` package, in order to automate the generation of an electron control sample from $e^+e^- \rightarrow e^+e^-e^+e^-$ events.

The resulting electron sample proved useful in the initial period of running of the experiment, when it was widely used (see for example [24, 44]). Control samples extracted from data will continue to be important as the algorithms used to identify electrons become more sophisticated.

6

Selection of $\tau^- \to \pi^-\pi^0\nu_\tau$ candidate events

This chapter describes the procedure for selecting $\tau^- \to \pi^-\pi^0\nu_\tau$ candidate events from the data set. Details of a filter used to pre-select events are included, as is a description of requirements imposed during the selection of suitable charged and neutral candidates. Particulars of the procedure for reconstructing neutral pion and charged ρ meson candidates are presented, and finally the techniques used for rejecting background events and subtracting any remaining fake candidates are discussed.

6.1 Data samples

For convenience, the vast *BABAR* data set is used as the basis for numerous more manageable subsets of events, known as skims. Each subset is composed of events which are candidates for containing a particular physical process. The analysis described here is based on data taken from the *TauQED* skim.

6.1.1 The data sample

The analysis described here is based on 19.2 fb^{-1} of data, 17.4 fb^{-1} of which was collected 'on-peak', at the $\Upsilon(4S)$ mass. The remainder of the sample was collected 'off-peak', at a centre of mass energy 40 MeV below the resonance. By running below the $\Upsilon(4S)$ peak, *BABAR* can study the non-$B\overline{B}$ contribution to on-peak data, a method used for background subtraction in many B-physics analyses. The data were logged during the year 2000 run of the experiment.

6.1.2 The Monte Carlo samples

A Monte Carlo sample is produced by combining simulated events according to their relative cross sections at *BABAR* (Table 6.1). Details of the Monte Carlo generators used to produce the various samples can be found in [28]. Gamma-gamma and μ-pair events are not simulated in large numbers and as a result the generic Monte Carlo sample does not include $e^+e^- \to \mu^+\mu^-$ events, nor events which model gamma-gamma processes. Instead, the available Monte Carlo events for these processes are used to independently check the level of contamination remaining after imposing all selection requirements. These checks show that gamma-gamma and $e^+e^- \to \mu^+\mu^-$ events introduce negligible contamination to the final sample of signal events.

Bhabha events are another special case. The large cross section for Bhabhas means that even if a significant number of Monte Carlo Bhabhas were available, it would still not be feasible to produce a simulated sample corresponding to the integrated luminosity of the data. Approximately 760 million simulated Bhabhas would be required (compared to 22 million μ-pairs); around one million events each of Bhabhas and μ-pairs are available as part of the *BABAR* simulation production. Again, the available Monte Carlo events are used to confirm that Bhabhas result in negligible contamination to the final sample of signal events.

Table 6.1: *Production cross sections for various processes at $\sqrt{s} = M(\Upsilon(4S))$. The $e^+e^- \rightarrow e^+e^-$ cross section is the effective cross section within the experimental acceptance.*

$e^+e^- \rightarrow$	Cross section (nb)
$b\bar{b}$	1.05
$c\bar{c}$	1.30
$s\bar{s}$	0.35
$u\bar{u}$	1.39
$d\bar{d}$	0.35
$\tau^+\tau^-$	0.94
$\mu^+\mu^-$	1.16
e^+e^-	~ 40

6.1.3 The TauQED skim

Numerous event selections, defined by the *Tau and QED Physics Group*, are used to produce a collection of events that are of particular interest for τ and two-photon physics studies. These selections, performed during data reconstruction, result in the flagging of candidate τ-pair and two-photon events. Selected events are used to create the data skim. The τ-pair topologies accounted for by the TauQED skim selections include 1-1 (one-on-one), 1-3, 3-3 and 1-5 configurations. The notation 1-3, for example, indicates that one τ decays to a single prong final state, apparent as a single charged track in the detector and that the other τ decays to a three prong final state, producing three charged tracks in the detector.

Table 6.2 shows the efficiency of the TauQED selection for various Monte Carlo processes. Although the efficiency for τ pair selection may appear low, at less than 50%, one must remember that the high luminosity of the PEP-II machine, along with the finite data storage capacity, mean that the selection is necessarily tight in order to keep the event rate from the TauQED stream within specified limits.

Table 6.2: *Trigger and TauQED skim selection efficiencies for various processes. Ten thousand Monte Carlo events are used to simulate each process.*

$e^+e^- \to$	Passing Level-1 (%)	AND Level-3 (%)	AND TauQED skim (%)
e^+e^-	100.0	45.3	2.6
$\mu^+\mu^-$	72.8	72.5	5.1
$\tau^+\tau^-$	86.4	81.3	46.8
$\gamma\gamma$	19.2	15.2	1.6
$u\bar{u}/d\bar{d}/s\bar{s}$	98.0	94.8	6.6
$c\bar{c}$	99.9	98.4	4.5
$B\bar{B}$	100.0	99.8	1.5

6.1.4 The BGFTau filter

Of all the event selection modules used to create the TauQED skim, the module most relevant to this analysis is the *BGFTau* filter, which is used to select events with a 1-1 topology. The filter is optimised to be efficient in selecting τ-pairs whilst reducing backgrounds from, for example, Bhabhas, μ-pairs and two-photon events [45]. The fraction of simulated events passing both the trigger simulation and the BGFTau selection is displayed in Table 6.3.

As a starting point, the BGFTau selection [46] requires an event to contain exactly two charged tracks (defined according to the criteria of Table 6.4, discussed in Section 6.2.1) with zero net charge. A large fraction of the Bhabha events passing the initial topology requirements are removed from the sample by requiring that at least one of the tracks has an E/p ratio (the ratio of energy deposited in the electromagnetic calorimeter to the track momentum, as measured in the drift chamber) less than 0.8. To reduce Bhabha contamination further, the sum of the energy deposited in the EMC by the two charged candidates is required to be less than 5 GeV. Requiring the sum of track momentum magnitudes to be less than 9 GeV/c largely removes μ-pair contamination.

Two-photon contamination is reduced by requiring that

$$R = \frac{p_{t_a} + p_{t_b}}{E_{cm} - p_a - p_b} > 0.07,$$

where p_{t_a} and p_{t_b} are the transverse momentum magnitudes of the two tracks, p_a and p_b the magnitudes of the momenta of the two tracks (all in the centre of mass system) and E_{cm} the centre of mass energy of the colliding beams. The effectiveness of this requirement is illustrated by Figure 6.1 which shows the distribution of R for τ-pair and leptonic two-photon events.

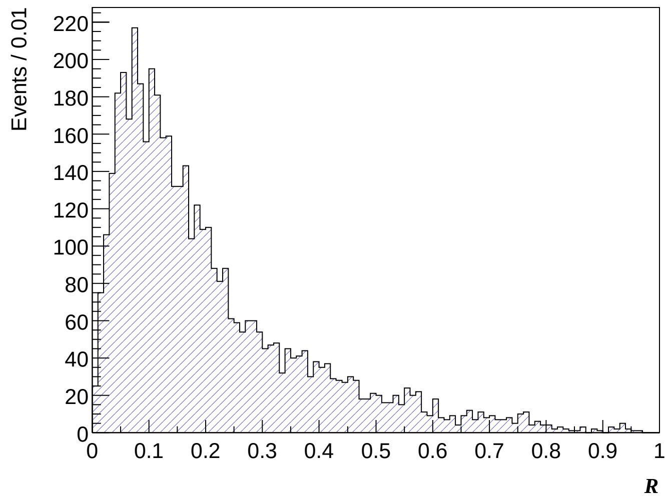

(a) Distribution of the ratio R for $e^+e^- \to \tau^+\tau^-$ events.

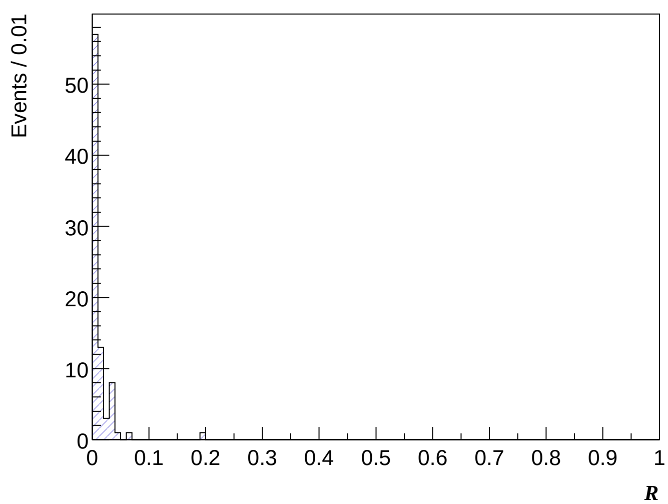

(b) Distribution of the ratio R for $e^+e^- \to e^+e^-\ell^+\ell^-$ events.

Figure 6.1: *A cut (rejecting events for values less than 0.07) on the ratio, R (see text), is used to reduce two-photon contamination.*

Table 6.3: *Fraction of simulated events passing Level 1, Level 3 and the BGFTau filter.*

$e^+e^- \to$	Passing BGFTau (%)
e^+e^-	2.1
$\mu^+\mu^-$	4.6
$\tau^+\tau^-$	35.7
$\gamma\gamma$	1.5
$u\bar{u}/d\bar{d}/s\bar{s}$	2.7
$c\bar{c}$	1.3
$B\bar{B}$	0.1

6.2 Event selection

The BGFTau filter is used to extract a sample of τ-pairs with a 1-1 topology from the data. In the case of simulated data, in addition to passing the BGFTau filter, candidate events are also required to pass a simulation of the Level-1 and Level-3 triggers. Contamination from Bhabhas, μ-pairs and two-photon processes is reduced by requiring that the missing momentum vector for the event is within the angular acceptance of the EMC (so that $-0.91 \leq \cos\theta_{miss} \leq 0.89$, see Figure 6.2(a)), and has a transverse component greater than 0.5 GeV/c (Figure 6.3(a)). The absence of Bhabha, μ-pair and gamma-gamma events from the Monte Carlo sample is illustrated by the clear disagreement of the distributions for data and Monte Carlo in Figures 6.2(a) and 6.3(a). Figure 6.2(b) shows the cosine of the polar angle of the missing momentum for the limited number of simulated Bhabha, μ-pair and gamma-gamma events available. The distributions are sharply peaked in the forward and backward directions, corresponding to the regions where the excesses are observed in the data. Figure 6.3(b) shows the magnitude of the transverse component of missing momentum for the same simulated events. Again, the distributions are peaked in regions corresponding to the excesses in the data distribution.

Having selected a sample of 1-1 τ-pairs, a τ^- decaying to $\pi^-\pi^0\nu_\tau$ (a charged ρ candidate) is defined as signal and in order to reduce background contributions, a tag decay of the τ^+ is also required. A tag decay is defined to be one of the following three modes: $\tau^+ \to e^+\nu_e\bar{\nu_\tau}$ (electron tag), $\tau^+ \to \mu^+\nu_\mu\bar{\nu_\tau}$ (muon tag), $\tau^+ \to \pi^+\pi^0\bar{\nu_\tau}$ (rho tag). In cases where both of the prongs contain a charged ρ candidate, the event is considered twice; each of the ρ mesons is considered a signal decay in turn.

6.2.1 Charged candidate selection

Tracks satisfying a standard selection [46] are considered 'good'. The requirements which must be satisfied in order for a track to pass the selection are shown in Table 6.4. If it is to be used in an attempt to reconstruct a signal system, an event must contain two such good tracks, separated by an angle of at least 90° in the centre of mass system.

6.2.2 Neutral candidate selection

Clusters of energy deposition in the calorimeter are considered neutral candidates if they are not associated with a charged track and have an energy of at least 20 MeV. Details of the procedure for associating tracks with calorimeter clusters can be found in Appendix B. Furthermore, each cluster should be made up of energy contributions from more than one electromagnetic calorimeter channel. This requirement minimises the chance of a noisy channel resulting in fake neutral

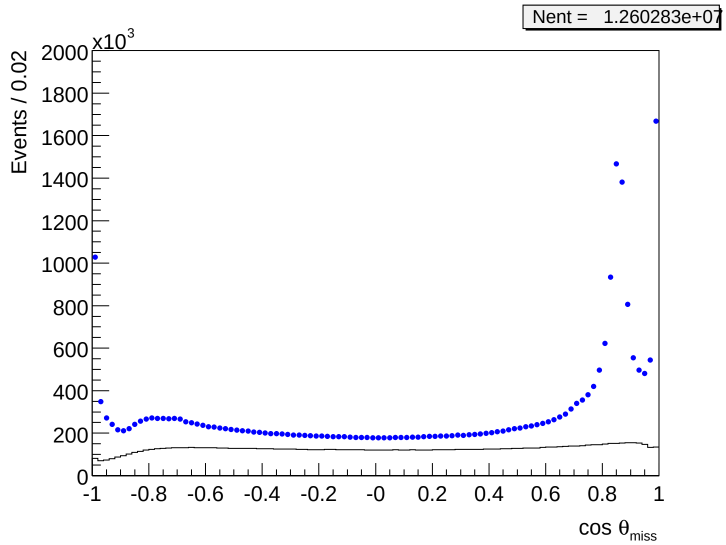

(a) Direction of event missing momentum for data (points) and the generic Monte Carlo sample (histogram). The clear excess visible in the data is due to Bhabha, μ-pair and gamma-gamma events which are not simulated in the Monte Carlo (see text).

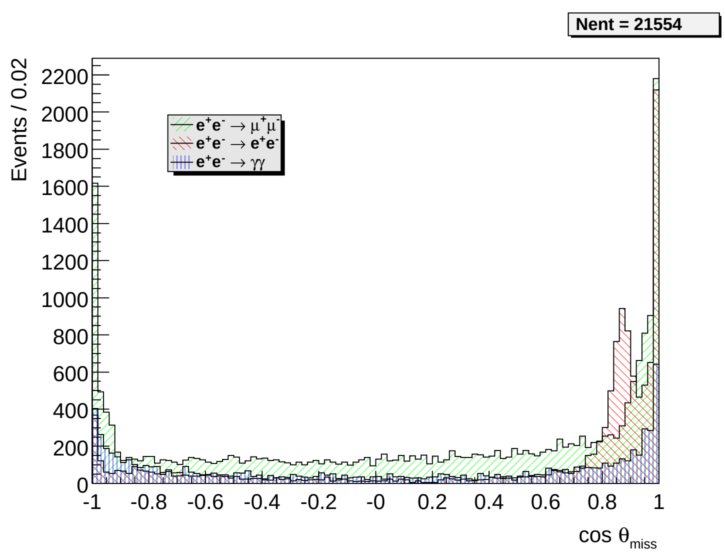

(b) Direction of event missing momentum for Monte Carlo Bhabhas, μ-pairs and two-photon events.

Figure 6.2: *Direction of event missing momentum.*

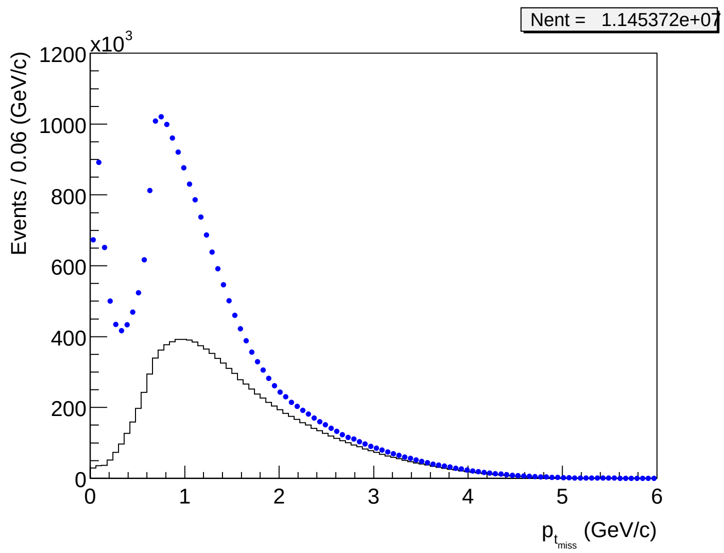

(a) Magnitude of the transverse component of event missing momentum for data (points) and Monte Carlo (histogram).

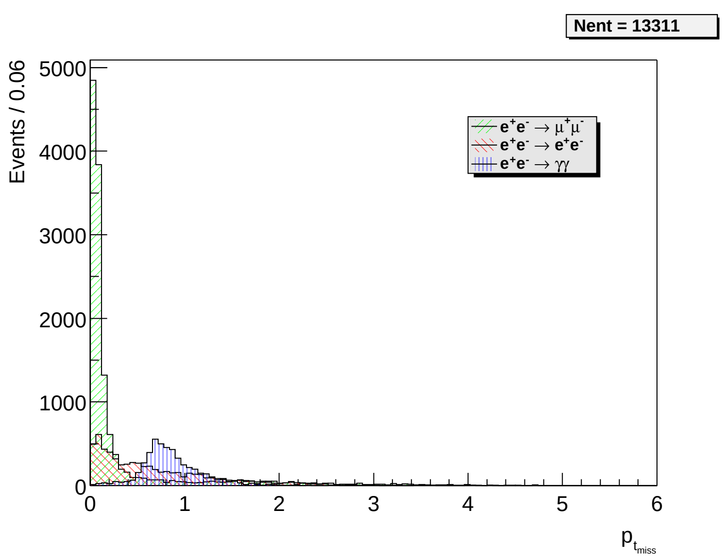

(b) Magnitude of the transverse component of event missing momentum for Monte Carlo Bhabhas, μ-pairs and two-photon events.

Figure 6.3: *Magnitude of the transverse component of event missing momentum.*

Table 6.4: *Requirements which must be satisfied if a reconstructed track is to be considered 'good' (Section 6.2.1). Distances are with respect to the interaction point.*

Parameter	Value
Minimum transverse momentum	0.1 GeV/c
Maximum momentum	10 GeV/c
Maximum distance of closest approach in x-y plane	1.5 cm
Minimum distance of closest approach in z	-10 cm
Maximum distance of closest approach in z	10 cm
Minimum number of DCH hits	20

candidates.

Figure 6.4 shows the energy distribution of all photon candidates. There is clearly an excess in the data relative to the Monte Carlo. One should not be surprised by this difference however, as the Monte Carlo sample does not account for Bhabha events (which are still present in significant numbers after the initial selection cuts). Section 6.2.6 contains details of cuts to veto remaining background events.

The excess in the data is also illustrated by Figures 6.5 and 6.6, which show the cosine of the polar angle and the number of crystals per cluster of the γ candidates.

6.2.3 Neutral pion reconstruction

Pairs of neutral candidates satisfying the requirements detailed in Section 6.2.2 are used to reconstruct π^0 candidates. The resulting invariant mass spectrum is displayed in Figure 6.7. Again there is a clear excess of gamma-gamma pairs in the data relative to the Monte Carlo, although the excess appears to be due to

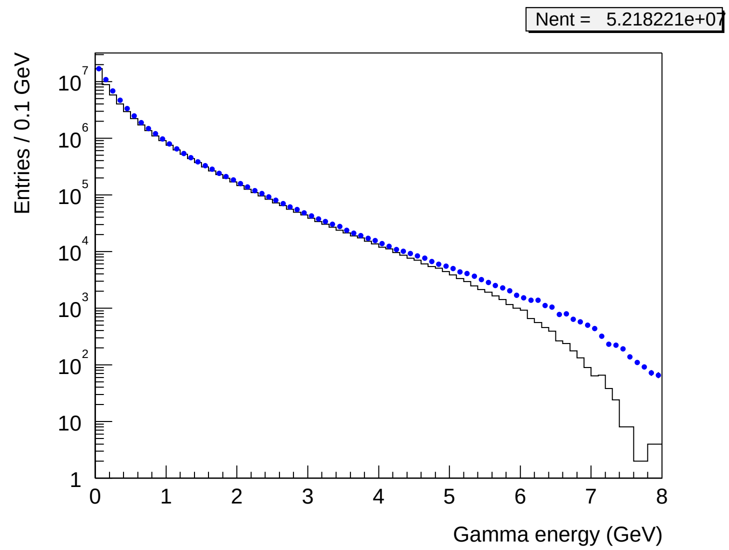

Figure 6.4: *Neutral candidate energy plotted for the data (points) and generic Monte Carlo sample (histogram).*

background candidates; the number of neutral pions appear to be consistent.

Neutral pions reconstructed from two photon candidates in this way are described as being *resolved*. Neutral pion candidates with an opening angle between the two photon candidates which is smaller than the calorimeter angular resolution (so that the two electromagnetic showers appear as one merged deposit) are described as *unresolved*. At *BABAR*, neutral pions with an energy greater than about 1.5 GeV (corresponding to approximately one third of all neutral pions resulting from the decay $\tau^- \to \pi^-\pi^0\nu_\tau$) tend to be unresolved.

The asymmetry of the gamma-gamma invariant mass peak arises as a result of energy leakage from the calorimeter. In a study of energy deposition in the CsI calorimeter crystals [47], a logarithmic normal distribution was found to best describe the data. The peak region of such a function is approximately Gaussian with a tail on the low mass side. A fit of a logarithmic normal distribution to the gamma-gamma invariant mass spectrum for data is shown in Figure 6.8(a). The mass

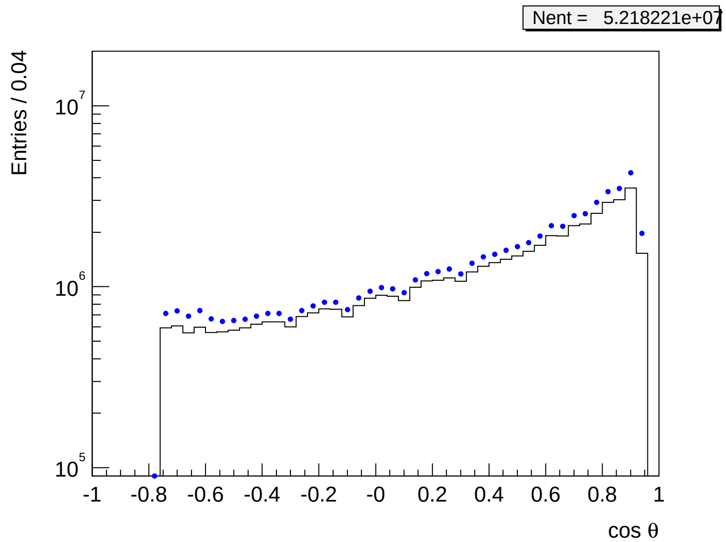

Figure 6.5: *Distribution in* $\cos\theta$ *of all* γ *candidates from the data (points) and generic Monte Carlo sample (histogram).*

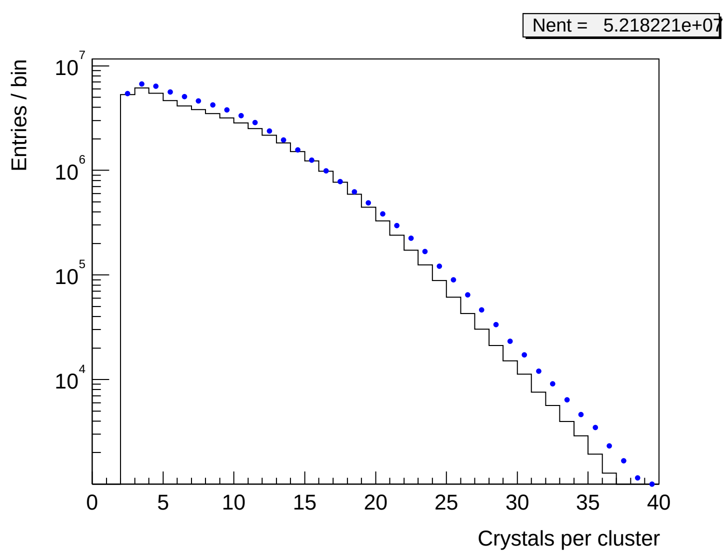

Figure 6.6: *Number of crystals per cluster for all gamma candidates from the data (points) and the generic Monte Carlo sample (histogram).*

resolution obtained from the fit is 6.5 MeV/c^2. A similar fit to the gamma-gamma invariant mass spectrum obtained from the Monte Carlo simulation (shown in Figure 6.8(b)) yields a width of 6.1 MeV/c^2.

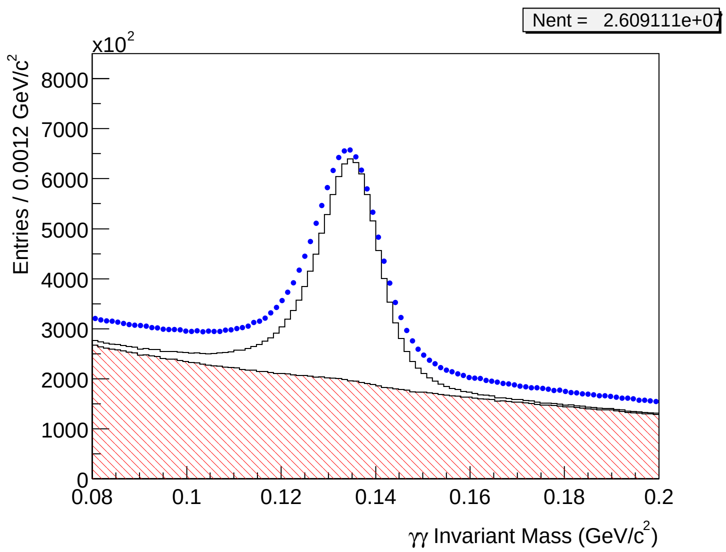

Figure 6.7: *Gamma-gamma invariant mass plotted for data (points) and Monte Carlo (open histogram). The contribution to the Monte Carlo distribution from fake π^0 candidates is also displayed (hatched histogram).*

6.2.4 The event tag

Cut-based particle identification algorithms are used to select electrons and muons for tagging purposes. Electron candidates are required to pass the 'tight' criterion of an electron selector [42] which makes use of information from the DCH and EMC. The E/p ratio (the ratio of energy deposited in the EMC to the track momentum as measured by the DCH), is required to be in the range 0.75–1.30. The EMC cluster should be constructed using information from at least four calorimeter channels, and have a value for the lateral shower shape parameter (Appendix

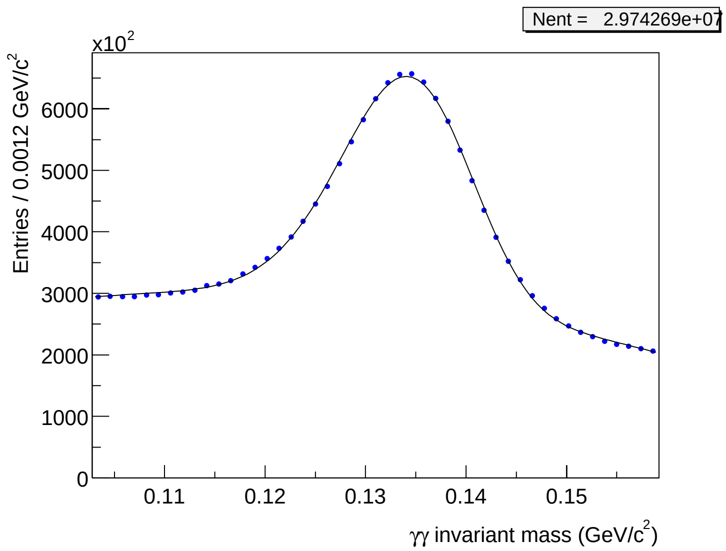

(a) Data

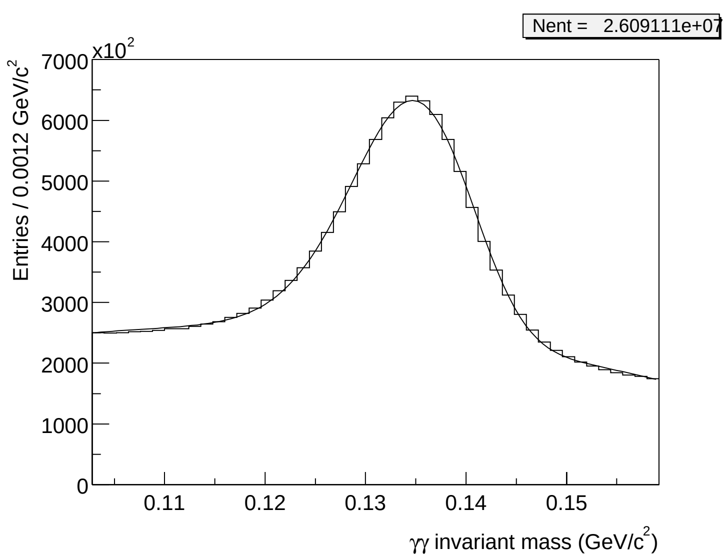

(b) Monte Carlo

Figure 6.8: *Gamma-gamma invariant mass distributions for data and Monte Carlo, fitted with a logarithmic normal distribution plus second order polynomial.*

A) in the range 0.0–0.6. The DCH measurement of dE/dx should be in the range 500–1000 (arbitrary units), consistent with the electron hypothesis.

The muon selector [48] is also used in tight mode, making use of information from the DCH, EMC and IFR. The energy deposited in the EMC is required to be in the range 0.05–0.4 GeV for candidates within the angular acceptance of the calorimeter (consistent with the minimum ionisation energy). The candidate is required to penetrate the IFR with a measured number of interaction lengths greater than two. In addition, the IFR cluster should be well matched to a track produced in the DCH. An algorithm is used to extend, or 'swim', tracks from the inner detector into the IFR. These extrapolated tracks are used to match DCH tracks to RPC hits; the χ^2 for the match is required to be less than five. In addition, the IFR cluster should have an average strip multiplicity per layer, N_{av}, less than eight, and σ_{mult} less than four, where

$$\sigma_{mult} = \left[\Sigma_i \frac{(N_{strips}(i) - N_{av})^2}{N_{layers} - 1}\right]^{\frac{1}{2}}. \tag{6.1}$$

If a track does not pass either the electron or the muon selection requirements, it is combined with a π^0 candidate (whose mass must be in the range 117-147 MeV/c^2, corresponding to -3σ to $+2\sigma$) in an attempt to reconstruct a charged ρ meson. If more than one π^0 candidate satisfies the requirements, then the one closest in angle to the initial track momentum is chosen. A track-π^0 combination is considered a ρ tag if the invariant mass of the combination is between 0.55 and 1.20 GeV/c^2.

The efficiencies and purities of the electron, muon and ρ tags as determined from Monte Carlo $e^+e^- \to \tau^+\tau^-$ events are shown in Table 6.5. Efficiency is defined as the total number of tagging modes correctly identified, divided by the total number of tagging modes present in the events considered. Purity is defined as the total number of tagging modes correctly identified, over the total number of tagging modes selected.

Table 6.5: *Efficiencies of the tag selectors.*

Tag mode	Efficiency (%)	Purity (%)
$\tau^+ \to e^+\nu_e\bar{\nu_\tau}$	91.8	91.0
$\tau^+ \to \mu^+\nu_\mu\bar{\nu_\tau}$	78.0	83.1
$\tau^+ \to \pi^+\pi^0\bar{\nu_\tau}$	44.8	48.1

6.2.5 Rho meson reconstruction

The reconstruction of the signal ρ meson is performed in a manner similar to that for the tagging ρ. The reconstructed gamma-gamma invariant mass must again be in the range 117-147 MeV/c^2. If this requirement is satisfied, a π^0 mass constraint is used to perform a kinematic fit in order to redetermine the photon energies and angles. The effect of this fitting procedure on the mass resolution is shown in Figure 6.9. Figure 6.9(a) shows the generated minus reconstructed $\pi^-\pi^0$ mass achieved for Monte Carlo data without kinematic fitting of the π^0. Figure 6.9(b) shows the same quantity when the kinematic fit is performed. The width of the peak is reduced from 16.7 MeV/c^2 to 14.0 MeV/c^2 as a result of the fitting procedure. Again, in the case of multiple ρ candidates, the one with the smallest track-π^0 angle is selected.

Attempts to use unresolved neutral pions to construct ρ meson candidates proved unsatisfactory. Unmatched energy deposits of at least 1.5 GeV were considered to be unresolved π^0 candidates if attempts to construct a ρ meson candidate from resolved π^0 candidates were unsuccessful. The mass spectrum resulting from such cases is shown in Figure 6.10(a). For comparison the invariant mass spectrum produced from resolved neutral pions is displayed in Figure 6.10(b). In the case of unresolved neutral pions, backgrounds are not well simulated by the Monte Carlo (particularly in the important invariant mass region near the τ mass). For

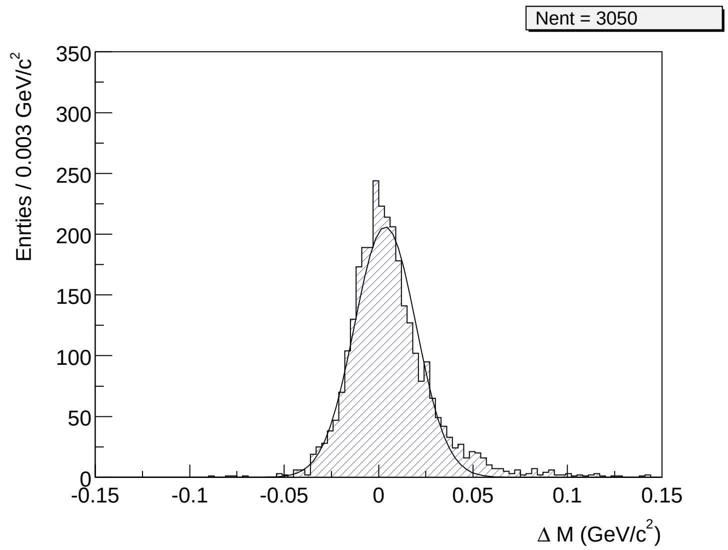

(a) Without kinematic fit.

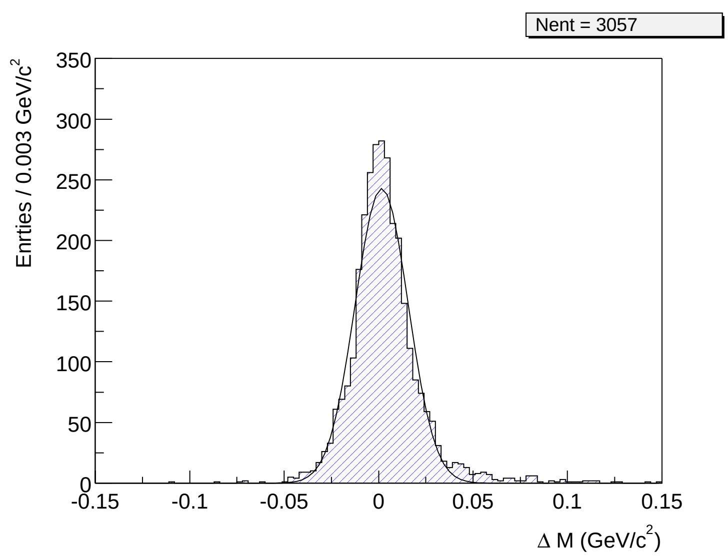

(b) With kinematic fit.

Figure 6.9: *Generated minus reconstructed mass of the $\pi^-\pi^0$ system, for all ρ mesons with a generated mass in the range 750-850 MeV/c^2. Constraining the π^0 mass and performing a kinematic fit to redetermine photon energies and angles improves the mass resolution. The curves show fits using a Gaussian distribution.*

this reason, only neutral pions which produced two distinct clusters in the EMC were used in attempts to reconstruct the $\pi^-\pi^0$ system.

6.2.6 Background rejection

Following the reconstruction of signal and tagging systems, some additional cuts are applied in an attempt further to veto background events.

In order to reduce contributions from background non-τ and non-signal τ events (for example events which have additional neutral pions in the final state) a requirement is made on the number of 'unused' neutrals. Any events containing one or more unused neutral clusters with energy greater than 50 MeV are vetoed.

A cut on the E/p ratio of the charged track used to construct the ρ meson candidate is also applied. A high value of E/p for this track may indicate an electron rather than a pion has been observed (as would be the case for any remaining Bhabha contamination, for example). Figure 6.11 shows the E/p distribution of the 'pions' in the data and Monte Carlo. Much of the electron contamination is removed by requiring a value of E/p less than 0.8.

Figure 6.12 shows the energy distribution of the reconstructed $\pi^-\pi^0$ systems. Any entries for values greater than the centre of mass beam-energy are clearly due to background. Events containing systems with excessive energy are vetoed. A similar argument holds for the total energy of the tagging system (Figure 6.13).

After performing the background rejection cuts, the agreement in the properties of remaining neutral pions reconstructed from data and simulation is good, as displayed in Figure 6.14.

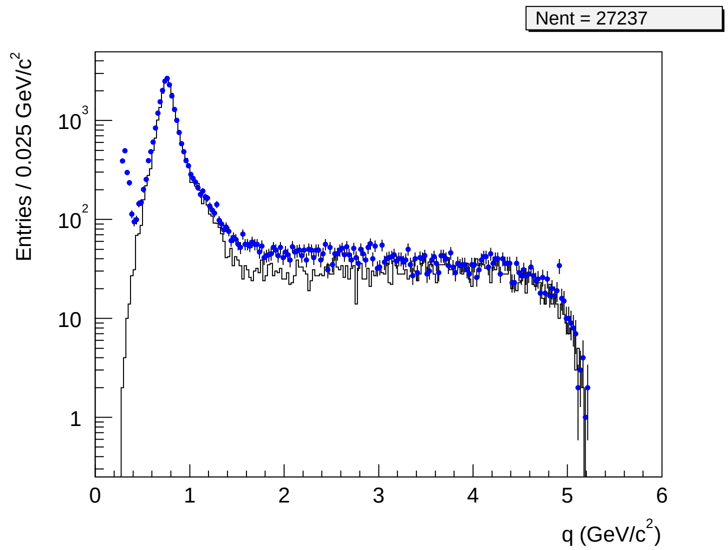

(a) Unresolved π^0 candidates.

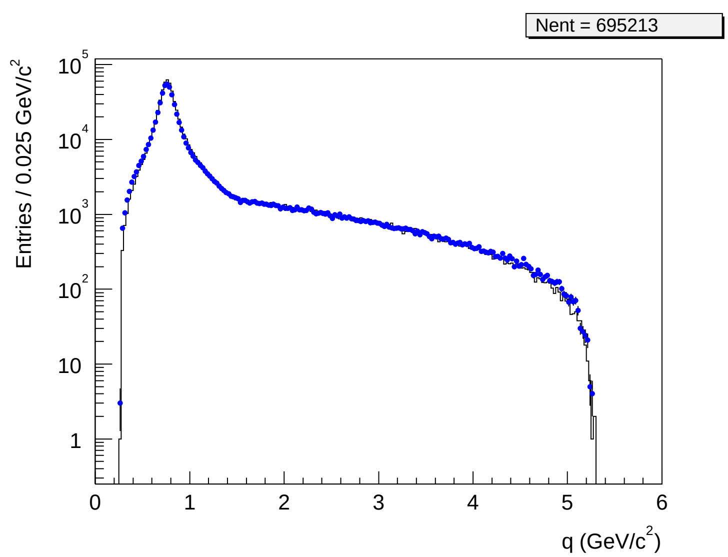

(b) Resolved π^0 candidates.

Figure 6.10: *Invariant mass spectra for $\pi^-\pi^0$ systems reconstructed from (a) unresolved and (b) resolved π^0 candidates. The points show the data, while the histograms show the Monte Carlo.*

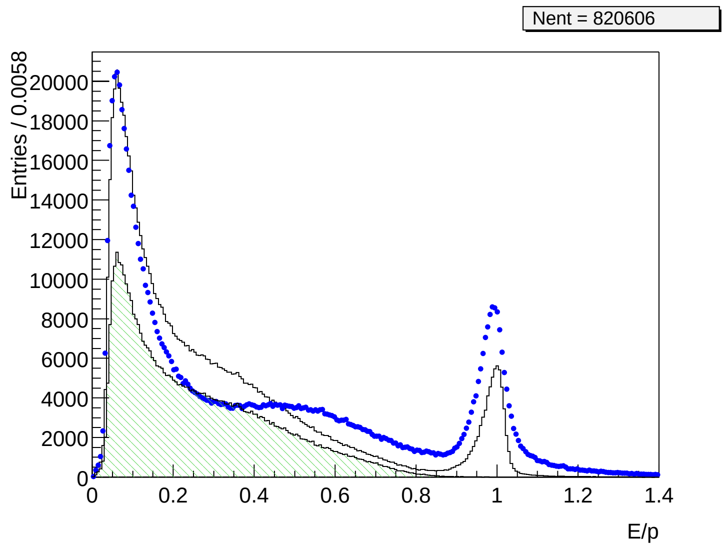

Figure 6.11: *Distribution of the E/p ratio for all charged tracks used to construct ρ meson candidates, plotted for data (points) and Monte Carlo (open histogram). The hatched histogram displays the distribution for signal events.*

6.3 Background subtraction

6.3.1 Background contributions

Figure 6.15 shows the non-signal $\pi^-\pi^0$ background contributions to the reconstructed $\pi^-\pi^0$ mass spectrum. It is clear that the majority of fake candidates are reconstructed from τ-pair events. Only a small number of background events from other sources (predominantly from $e^+e^- \to u\bar{u}/d\bar{d}/s\bar{s}$ and $e^+e^- \to \mu^+\mu^-$) remain in the final sample.

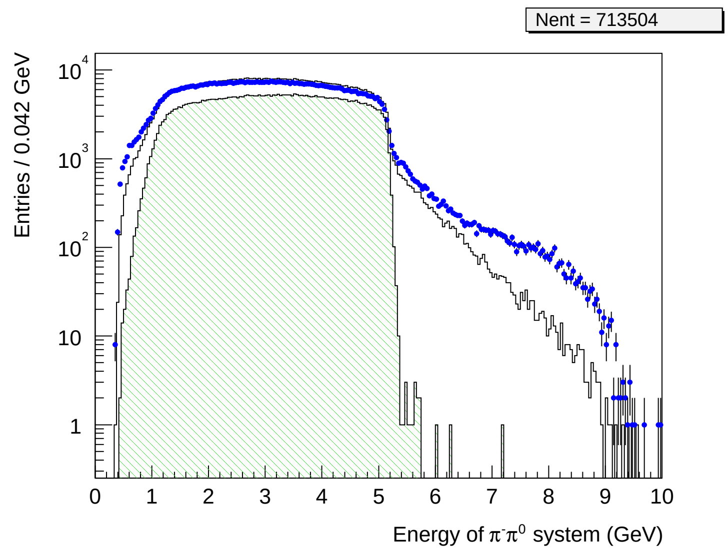

Figure 6.12: *Energy distribution of all reconstructed $\pi^-\pi^0$ systems, displayed for data (points) and Monte Carlo (open histogram). The hatched histogram displays the distribution for signal events.*

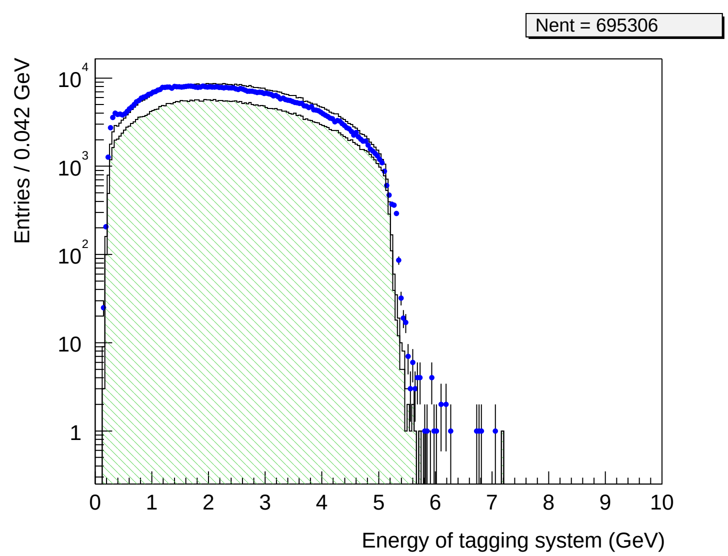

Figure 6.13: *Energy distribution of all reconstructed tagging systems, displayed for data (points) and Monte Carlo (open histogram). The hatched histogram displays the distribution for signal events.*

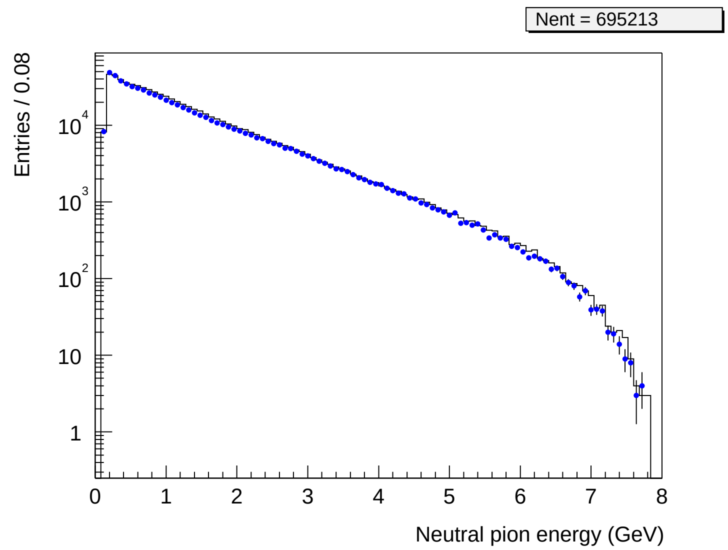

Figure 6.14: *Energy of π^0 candidates in events passing all event selection cuts, shown for data (points) and Monte Carlo (histogram).*

6.3.2 Background subtraction

The non-signal $\pi^-\pi^0$ background spectrum from the generic Monte Carlo sample is used to correct the data for background contributions. The correction is performed by carrying out a bin-by-bin subtraction.

For a sufficiently large number of events, we would expect the non-signal $\pi^-\pi^0$ background spectrum to be smooth. In order to remove statistical bin-to-bin fluctuations from the important region near the τ mass, a polynomial is used to fit the Monte Carlo background spectrum and the contents of each bin modified so that it is equal to the value of the fitted function at the bin centre. Figure 6.16 shows the polynomial fit to the Monte Carlo background spectrum.

Figure 6.17 shows the modified background and the invariant mass spectrum reconstructed from data. Apart from in the highest mass region, there is excellent agreement for invariant masses greater than the τ mass where candidates must

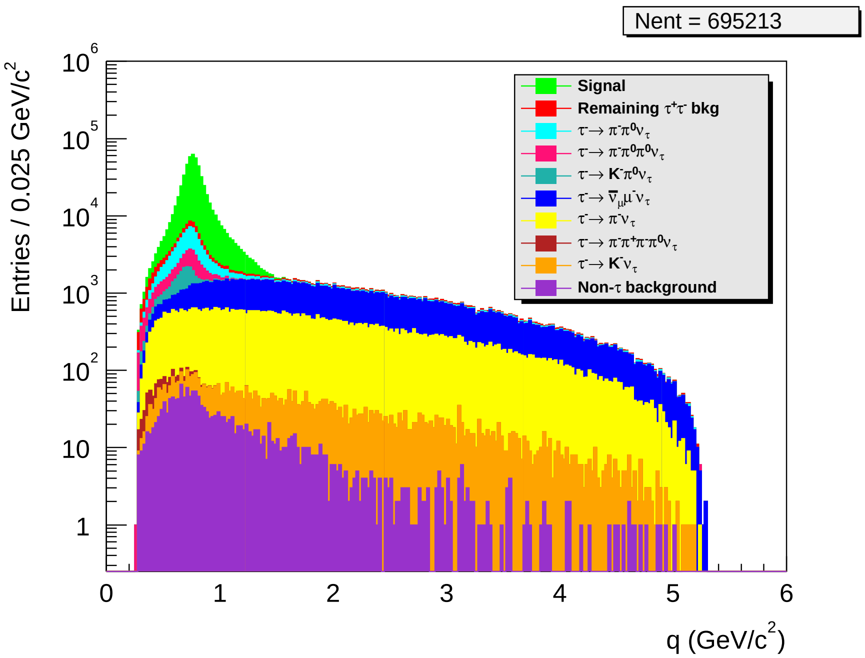

Figure 6.15: *Background contributions to the $\pi^-\pi^0$ invariant mass spectrum. From foreground to background (bottom to top in the legend) contributions from various channels are plotted cumulatively. Background contributions from $\tau^- \to \pi^-\pi^0\nu_\tau$ arise when a signal mode is reconstructed incorrectly (a background gamma ray may be used in reconstructing the π^0 candidate for example).*

correspond to background contributions.

The mass peak after background subtraction is displayed Figure 6.18. The limited number of entries for invariant masses greater than the τ mass suggest that there is no significant background remaining after the subtraction procedure. One of course expects positive (and negative) numbers of entries for bins at masses greater than the τ mass due to statistical fluctuations in the bin contents of the data mass spectrum. Figure 6.19 shows the peak after background subtraction plotted on a linear scale (so that error bars in the region of the peak are visible).

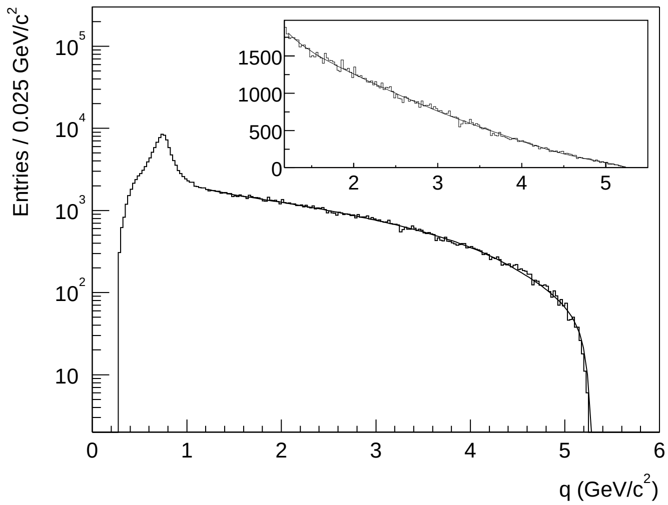

Figure 6.16: *Polynomial fit to the Monte Carlo background spectrum. The fit is performed for invariant masses greater than 1.2 GeV/c^2. The histogram is reproduced and displayed in the inset (with a linear scale) for invariant masses in the range 1.2-5.5 GeV/c^2.*

6.3.3 Error propagation

Error bars on the background-subtracted mass spectrum result from the combination of statistical errors on the data points of the Monte Carlo background spectrum and the initial data spectrum. For the mass region of the Monte Carlo background spectrum which was smoothed (after the polynomial fitting procedure), bin contents are assumed to be error free so that only the data errors contribute. Errors and their treatment are discussed further in Section 7.1, which contains a description of the fitting procedure.

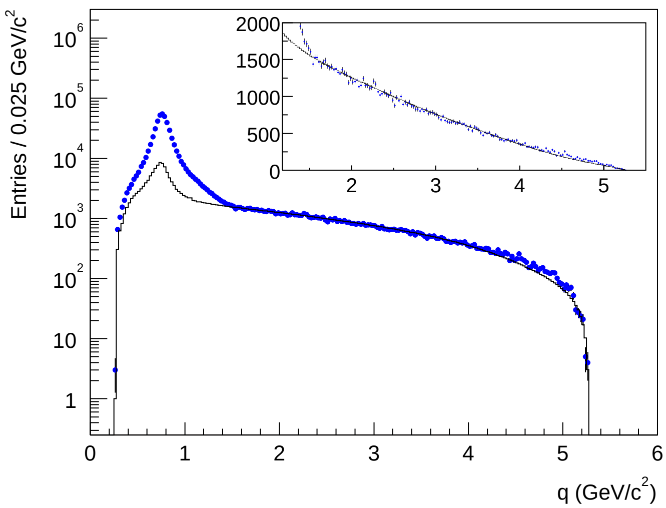

Figure 6.17: *Invariant mass spectrum reconstructed from data (points) and smoothed Monte Carlo background spectrum (histogram). There is clearly a good agreement for invariant masses greater than the τ mass, where only fake candidates can contribute to the data spectrum. Again, the plot is reproduced and displayed in the inset (with a linear scale) for invariant masses in the range 1.2-5.5 GeV/c^2.*

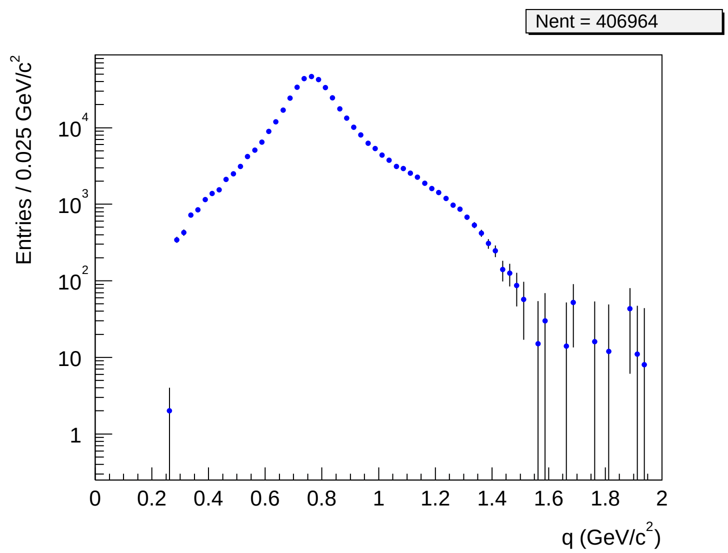

__Figure 6.18:__ The $\pi^-\pi^0$ invariant mass spectrum after background subtraction.

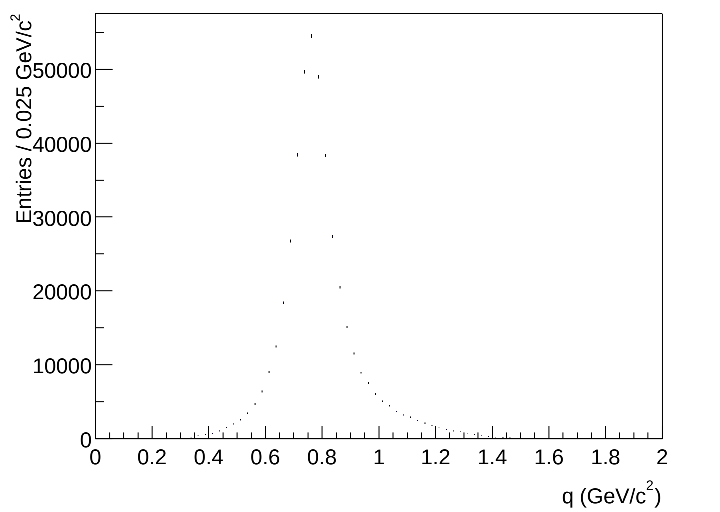

__Figure 6.19:__ The $\pi^-\pi^0$ invariant mass spectrum after background subtraction. This time a linear scale is used so that error bars in the region of the peak are visible.

6.4 Selection efficiency

Figure 6.20 shows the efficiency of the selection as a function of generated $\pi^-\pi^0$ mass. The efficiency is approximately linear, decreasing slightly with decreasing mass. A more marked fall in efficiency occurs for invariant masses less than 0.6 GeV.

If one wishes to study the shape of the $\pi^-\pi^0$ mass spectrum, the measured spectrum clearly needs to be modified to take into account the variation in selection efficiency as a function of mass. Details of the correction procedure are presented in Chapter 7.

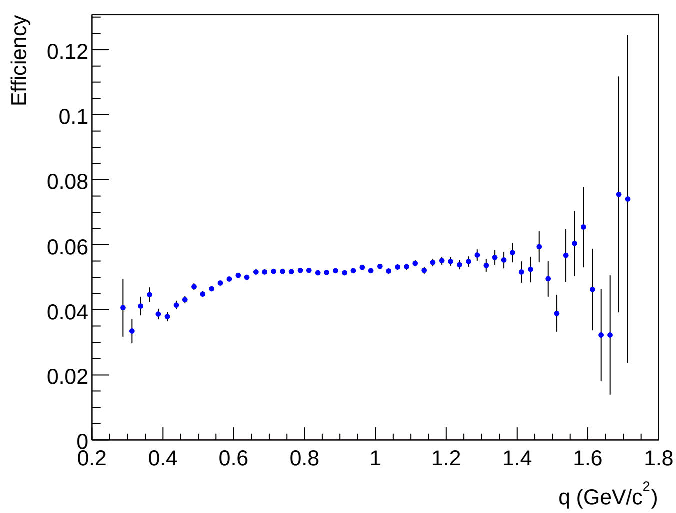

Figure 6.20: *Reconstruction efficiency as a function of generated $\pi^-\pi^0$ mass, as determined from the $\tau^+\tau^-$ Monte Carlo sample.*

The effects of the various event selection cuts on the efficiency of the sample are illustrated in Table 6.6. Following the event selection cuts, further cuts are applied to individual candidate systems (recall that up to two candidate systems per event are possible). The effects of these cuts on the efficiency of the sample are shown in

Table 6.6: *Efficiency at various stages of the event selection procedure. The values quoted refer to the fraction of events, containing at least one signal mode, that pass the cuts.*

Cut	Efficiency (%)
Tag filter	48.9
Good track cut	48.0
Angle in CMS	45.8
p_{miss} in EMC	42.4
$p_{t_{miss}}$ requirement	40.3

Table 6.7. It is clear that the process of reconstructing the neutral pion and charged ρ meson candidates results in a substantial decrease in efficiency. Although the π^0 reconstruction efficiency is 62% (recall that no attempt is made to reconstruct unresolved π^0 which account for approximately one third of all neutral pions), a considerable number of fake neutral pions result in fake ρ meson candidates and hence further decrease the overall reconstruction efficiency. The purity of the final sample is 65%.

It is worth noting at this point, that, even though the selection efficiency for signal decays is slightly lower than the value achieved by the CLEO collaboration, the BABAR $\pi^-\pi^0$ mass spectrum (shown in Figure 6.18) contains over four times the number of events present in the equivalent CLEO spectrum (and over an order of magnitude more than the number present in the equivalent ALEPH spectrum).

Table 6.7: *Efficiency at various stages of the candidate selection procedure (after π^0 and track candidates have been combined in order to construct charged ρ meson candidates).*

Cut	Efficiency (%)
Require a ρ candidate	10.7
Pass L1 simulation	10.6
Pass L3 simulation	10.6
Passes tag requirement	10.6
Remaining neutral energy veto	5.8
E/p of ‘pion’	5.5
Energy of signal/tag systems	5.5
Neutral pion energy	5.4

7

Results and conclusion

7.1 Fitting procedure

The background-subtracted invariant mass spectrum of the $\pi^-\pi^0$ system is fitted for the models described in Section 2.4. However, as a result of detector resolution effects, the measured $\pi^-\pi^0$ invariant mass spectrum is broader than the true mass spectrum. Furthermore, the efficiency of the charged ρ selection varies with mass. Because fits are performed to the measured mass spectrum (which is not corrected for efficiency or resolution effects), it is necessary to *smear* the fit functions to take into account the distortions due to detector effects.

The effects of inefficiencies and finite resolution on an invariant mass distribution during the measurement process can be understood in terms of a linear equation

$$Ax = b, \tag{7.1}$$

where $x = x_1, ..., x_n$ is the binned true mass distribution to be determined and $b = b_1, ..., b_m$ is the measured distribution. $A = A_{11}, ..., A_{mn}$ is the detector response matrix which may be produced by simulating the measurement process using Monte Carlo techniques. The matrix element A_{ij} gives the probability that an event with a true mass in bin j is reconstructed in bin i. For example, if we generate the distribution and perform our detector simulation, every entry in a measured bin can be traced back to its origin, giving us a well-defined set of linear relations between the generated and measured distributions, as in (7.1).

The smearing of the fit functions is performed using a detector response matrix (shown in Figure 7.1) derived from a histogram of generated versus reconstructed $\pi^-\pi^0$ mass obtained from Monte Carlo (shown in Figure 7.2).

For both the Kühn and Santamaria and Gounaris and Sakurai models, fits are performed with the $\rho(1700)$ coupling parameter γ (Section 2.4.2) set to zero and again with it allowed to float as a parameter of the fit. The overall normalisation of the functions is also allowed to float as a parameter of the fit. The `TMinuit` C++ class (a conversion of the original Fortran version of the `MINUIT` program [49]) is used to perform the χ^2 minimisation.

Because of uncertainties in the background subtraction method, fits are performed over a limited region of the mass spectrum, from 0.5 GeV/c^2 to 1.5 GeV/c^2. Any contribution to the line shape from the $\rho(1700)$ should be apparent even without fitting to the end point of the spectrum since the resonance is expected to be broad (with a width of approximately 235 MeV). In the cases where a contribution from

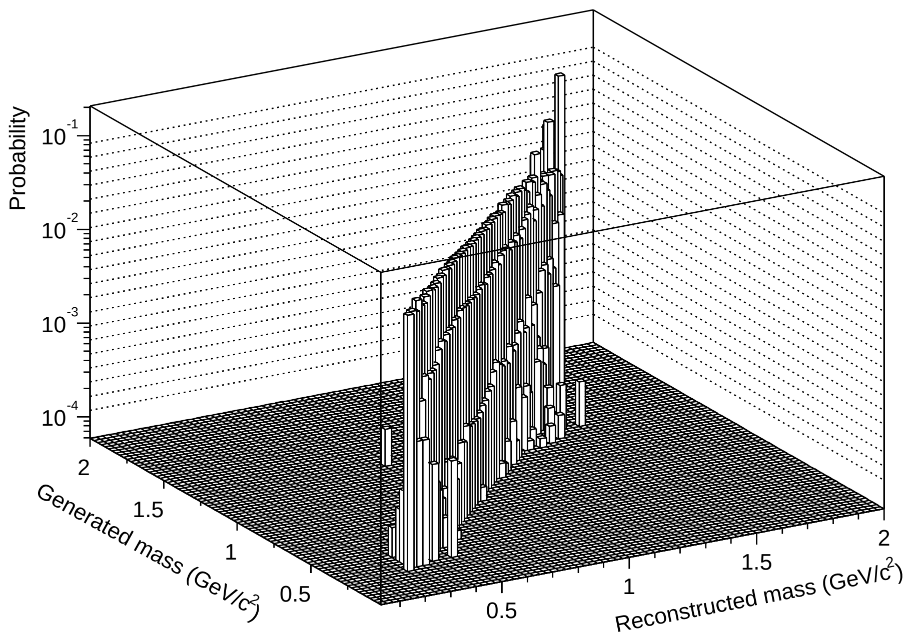

Figure 7.1: *Detector response probability matrix constructed from $\tau^- \to \pi^-\pi^0\nu_\tau$ Monte Carlo.*

the $\rho(1700)$ is included in the fit, its mass and width are fixed to values presented by the Particle Data Group.

The finite size of the sample of simulated events results in uncertainties in the elements of the detector response matrix. These uncertainties are combined with the statistical errors on data points in the invariant mass spectrum during the χ^2 minimisation.

As a test of the fitting procedure, the invariant mass spectrum from the generic Monte Carlo sample is used in a fit to the Kühn and Santamaria model. Figure 7.3(a) shows that the smeared function is a good fit to the Monte Carlo spectrum, with a χ^2 per degree of freedom of 30.0/34. The residual for each bin, Figure 7.3(b), is formed by subtracting the value of the smeared function evaluated at

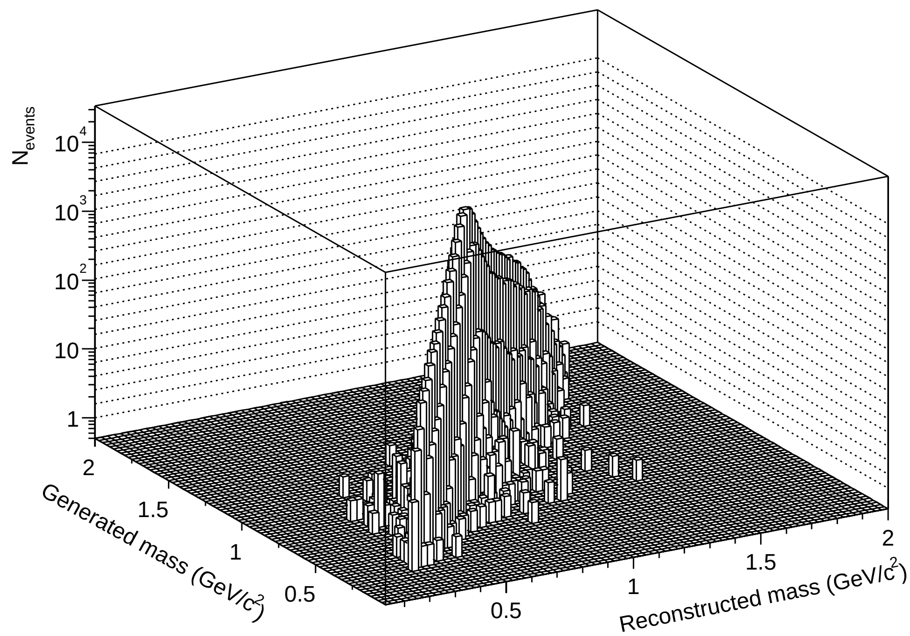

Figure 7.2: *'Number of events' response matrix constructed from $\tau^- \to \pi^-\pi^0\nu_\tau$ Monte Carlo.*

the bin centre, from the number of entries in the bin. Because the residual values near the peak are significantly larger than those at higher invariant masses, the residuals for the high invariant mass region are reproduced, with a larger scale, in the inset of Figure 7.3(b).

The parameters extracted from the fit (Table 7.1) are in reasonable agreement with the parameters used as input to the simulation process, although there do appear to be some small systematic shifts.

Inspection of the data spectrum reveals a problem due to remaining backgrounds at low invariant masses, which distorts the spectrum close to the $\rho(770)$ peak. Evidence of the unsimulated backgrounds can be seen in Figure 7.4, which shows data and Monte Carlo spectra (after background subtraction).

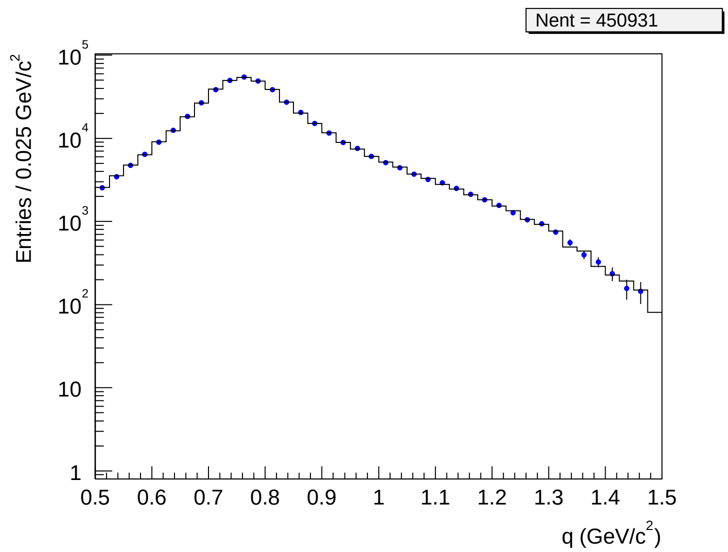

(a) Background subtracted Monte Carlo mass spectrum (data points) and fit (histogram) to the Kühn and Santamaria model with γ set to zero (so that there is no contribution from the ρ(1700)).

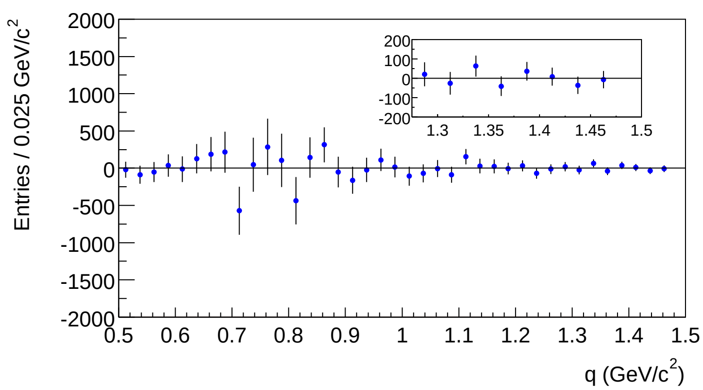

(b) Residuals for the fit shown in (a). The high mass region (where the residual is typically small) is magnified and displayed in the inset.

Figure 7.3: *Monte Carlo fit to the Kühn and Santamaria model with γ set to zero (so that there is no contribution from the ρ(1700)).*

Table 7.1: *Parameters extracted from a Kühn and Santamaria fit to the Monte Carlo (Figure 7.3(a)). Units for all masses and widths are MeV/c^2.*

Parameter	Fitted Value	Input to simulation
M_ρ	774.0 ± 0.4	773.0
Γ_ρ	147.8 ± 0.7	145.0
β	-0.1349 ± 0.0071	-0.1450
$M_{\rho'}$	1360 ± 10	1370
$\Gamma_{\rho'}$	512.5 ± 39.0	510.0

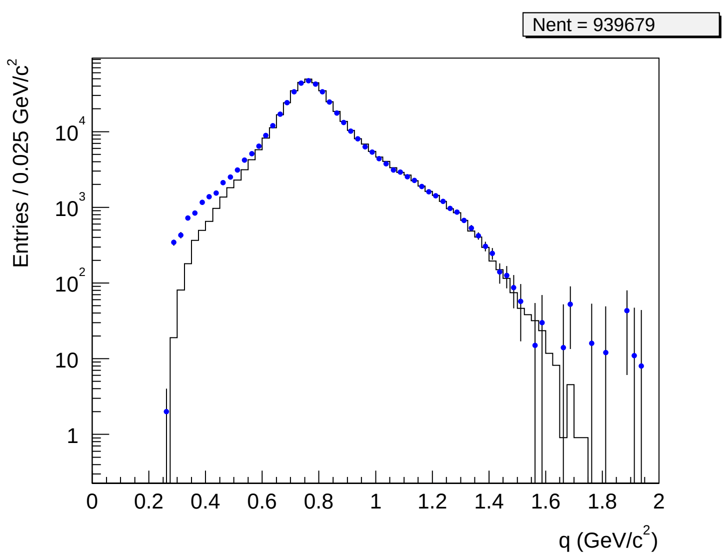

Figure 7.4: *Data (points) and Monte Carlo (histogram) mass spectra after background subtraction. There is a clear excess in the data spectrum for low invariant masses.*

An additional term in the fit is used to parameterise the remaining low mass background. The background term (shown in (7.2)) consists of rapidly rising and exponentially decreasing factors, along with an overall normalisation, resulting in three additional parameters (a, b and c) in each fit. The additional term is of the form,

$$\text{BKG} = a(q - m_t)^b \exp\left[-c(q - m_t)\right], \tag{7.2}$$

where q is the $\pi^-\pi^0$ invariant mass and m_t is the threshold for $\pi^-\pi^0$ production. The background contribution to the spectrum, although falling away rapidly with increasing mass, still contributes near to the $\rho(770)$ mass peak, and it was found necessary to fix the $\rho(770)$ resonance parameters in the fits. These parameters have in any case already been well measured in τ decays.

The constants a, b and c are determined by fitting the mass spectrum using the Kühn and Santamaria model. Minimising χ^2 results in the values:

$$a = 5.45 \times 10^7,\ b = 3.35,\ c = 14.31.$$

All subsequent fits are performed with the parameters fixed at these values.

For convenience, the resonance parameters extracted from all fits are summarised in Table 7.2, and their correlations are given in Tables 7.3 and 7.4.

7.1.1 The model of Kühn and Santamaria

Figure 7.5(a) displays the fit of the $\pi^-\pi^0$ mass spectrum to the model of Kühn and Santamaria, while Figure 7.5(b) shows the fit residuals. From Figures 7.5(a) and 7.5(b), it is clear that the largest contributions to the χ^2 value are from the points around the $\rho(770)$ mass. Away from the $\rho(770)$ peak, the points contribute to the χ^2 value at a level which would typically be expected for a good fit (the χ^2 contribution for the mass range 0.9-1.5 GeV is 21.2 for 24 bins).

A possible explanation for the poor quality of the fit in the region of the $\rho(770)$ peak is the fact that the simulated background peaks near the ρ mass, and the background subtraction process will therefore be sensitive to the values for the $\rho(770)$ mass and width used in the simulation.

Figure 7.6(a) shows another Kühn and Santamaria fit, this time with a contribution from the $\rho(1700)$ allowed. The fit residuals, shown in Figure 7.6(b), are similar to the residuals for the Kühn and Santamaria fit without a $\rho(1700)$ contribution.

7.1.2 The model of Gounaris and Sakurai

Figure 7.7(a) displays the fit of the $\pi^-\pi^0$ mass spectrum to the model of Gounaris and Sakurai, with the residuals for the fit shown in Figure 7.7(b). The resonance parameters extracted from the fit are shown in Table 7.2.

Figure 7.8(a) displays the fit of the $\pi^-\pi^0$ mass spectrum to the model of Gounaris and Sakurai including a contribution from the $\rho(1700)$. The residuals for this fit are shown in Figure 7.8(b).

7.2 Comparison with previously published results

Fits to both the Kühn and Santamaria and Gounaris and Sakurai models confirm that contributions from Breit-Wigner line shapes of the $\rho(770)$ and $\rho(1450)$ resonances are required to describe the $\pi^-\pi^0$ invariant mass spectrum. For the case when only two interfering resonances contribute to the models for the weak pion form factor, both the Kühn and Santamaria and the Gounaris and Sakurai models give acceptable fits (yielding values for χ^2/dof of 57.4/36 and 58.1/36 respectively); there is no clear preference for either model. This result is in agreement

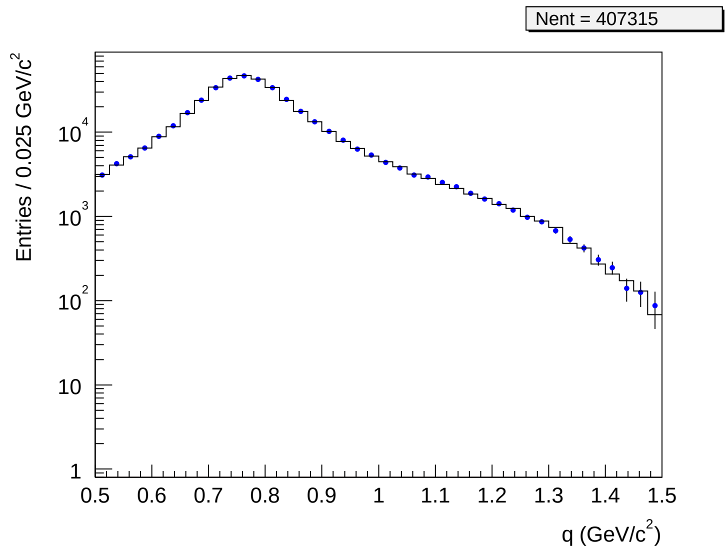

(a) Background subtracted mass spectrum (data points) and fit (histogram) to the Kühn and Santamaria model with γ set to zero (so that there is no contribution from the ρ(1700)).

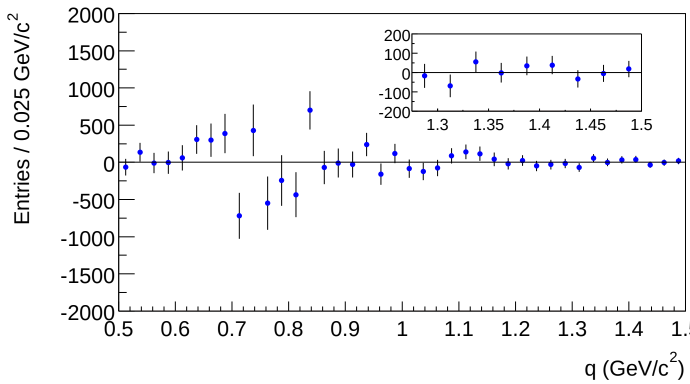

(b) Residuals for the fit shown in (a). The high mass region (where the residual is typically small) is magnified and displayed in the inset.

Figure 7.5: *Kühn and Santamaria model with γ set to zero (so that there is no contribution from the ρ(1700)).*

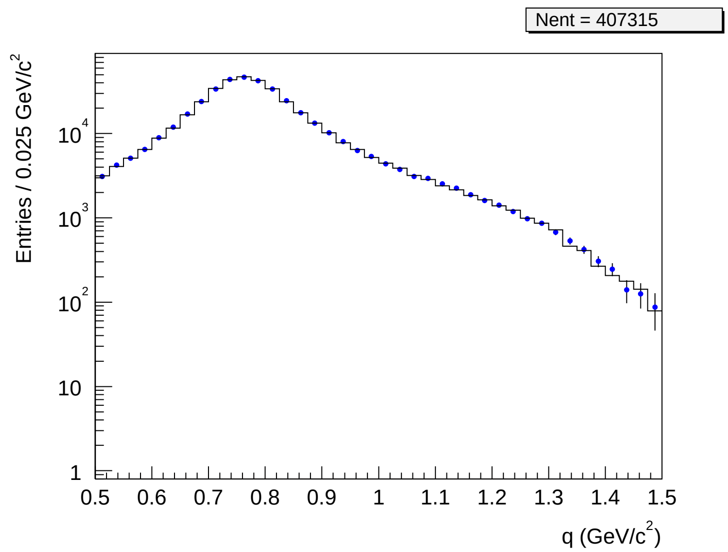

(a) Background subtracted mass spectrum (data points) and fit (histogram) to the Kühn and Santamaria model with non-zero γ (so that a ρ(1700) contribution is included).

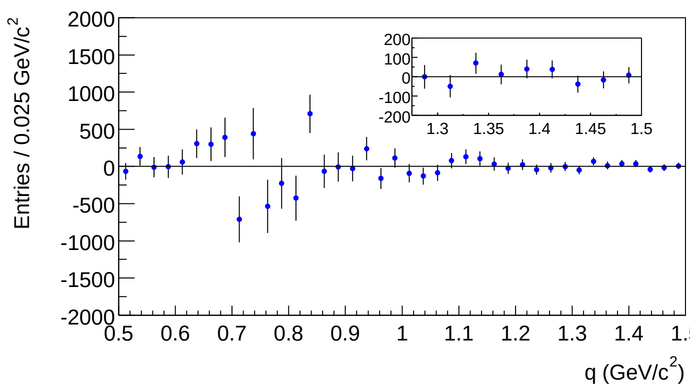

(b) Residuals for the fit shown in (a). The high mass region (where the residual is typically small) is magnified and displayed in the inset.

Figure 7.6: *Kühn and Santamaria model with a ρ(1700) contribution.*

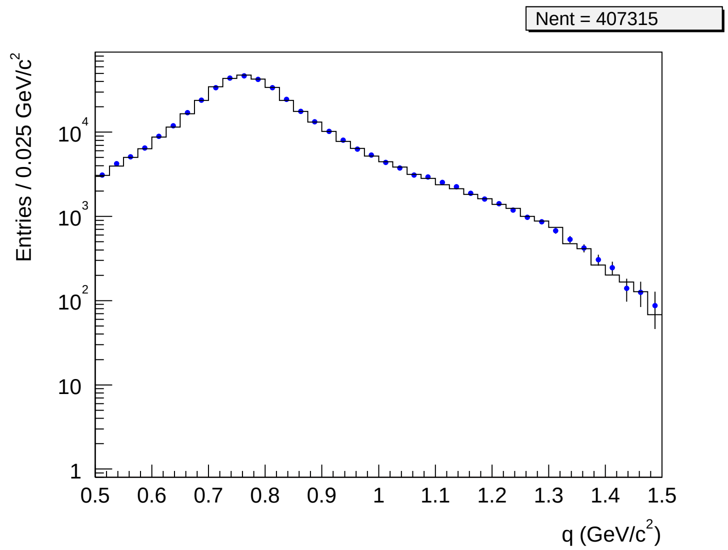

(a) Background subtracted mass spectrum (data points) and fit (histogram) to the Gounaris and Sakurai model with γ set to zero (so that there is no contribution from the ρ(1700)).

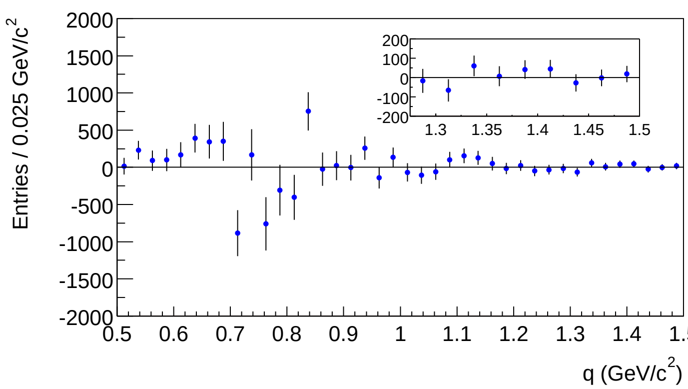

(b) Residuals for the fit shown in (a). The high mass region (where the residual is typically small) is magnified and displayed in the inset.

Figure 7.7: *Gounaris and Sakurai model with γ set to zero (so that there is no contribution from the ρ(1700)).*

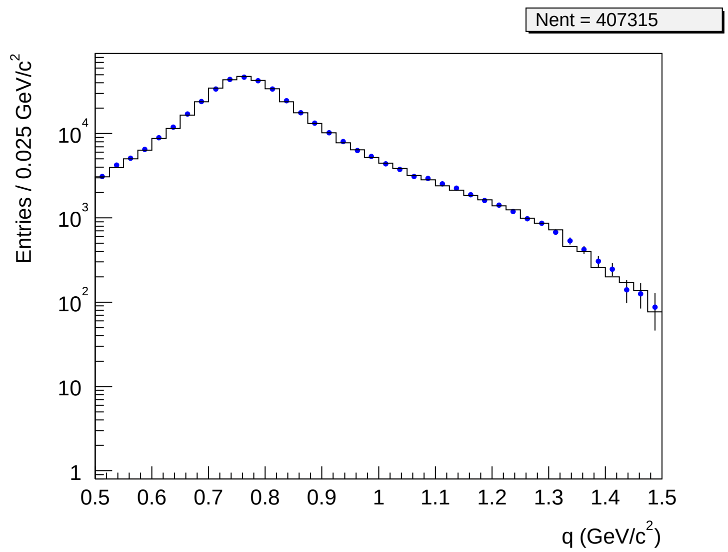

(a) Background subtracted mass spectrum (data points) and fit (histogram) to the Gounaris and Sakurai model with γ non-zero (so that the ρ(1700) contribution is included).

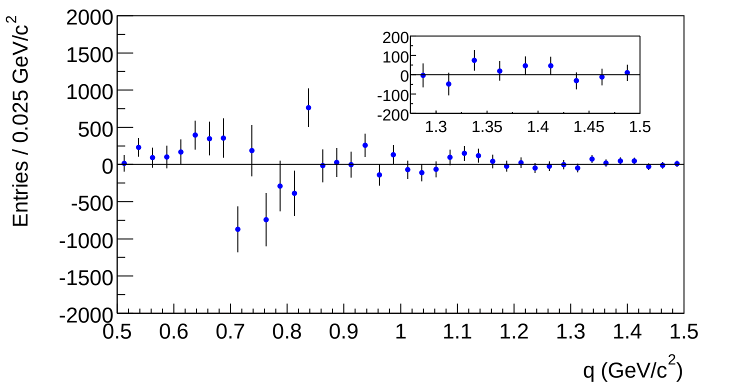

(b) Residuals for the fit shown in (a). The high mass region (where the residual is typically small) is magnified and displayed in the inset.

Figure 7.8: *Gounaris and Sakurai model with a ρ(1700) contribution.*

with the findings of the CLEO collaboration who also found their data well described by both the Kühn and Santamaria and Gounaris and Sakurai models. The ALEPH collaboration however found that the Gounaris and Sakurai model was preferred over the Kühn and Santamaria model.

The results from the two-resonance fits are displayed, along with the corresponding values reported by the CLEO collaboration, in Table 7.5. All parameters are in agreement with those reported by CLEO. For comparison, Table 7.6 shows current Particle Data Group values for $\rho(770)$ and $\rho(1450)$ resonance parameters.

Introducing a contribution from the $\rho(1700)$ resonance leads to marginally improved fits, in agreement with the observations recorded by the ALEPH and CLEO collaborations. For $\rho(1700)$ parameters set to values of $M_{\rho(1700)} = 1700\,\text{MeV}/c^2$ and $\Gamma_{\rho(1700)} = 235\,\text{MeV}$, the Kühn and Santamaria and Gounaris and Sakurai models yield χ^2/dof values of 56.7/35 and 58.0/35 respectively. Including an additional interfering resonance also influences the fitted parameters of the $\rho(1450)$. Parameters extracted from the three resonance fits are displayed in Table 7.7.

7.3 Fully corrected mass spectrum

In order to extract the physical mass distribution (and hence the fully corrected partial width as a function of $\pi^-\pi^0$ mass for the signal decay) it is necessary to *unfold* the measured spectrum from the effects of measurement distortion. The `GURU` software package [50] contains routines which perform the relevant procedure, a description of which is contained in the following sections.

7.3.1 The problem

Because the matrix A (described in Section 7.1) is numerically singular, the direct inversion of (7.1) leads to unstable and therefore useless results. The following sections outline the steps in solving (7.1). The method, based on the *singular value decomposition* of the response matrix A, overcomes the problem of rapidly oscillating solutions through the use of a regularisation method. A more complete description of the process can be found in [50].

7.3.2 The correction method

The unfolding algorithm can be divided into a number of distinct operations. The details and purpose of each of these operations are outlined below.

7.3.2.1 Singular value decomposition

In order to extract the statistically significant information in A, a singular value decomposition method can be applied. The matrix A is decomposed through

$$A = USV^T, \tag{7.3}$$

where U is an $m \times m$ orthogonal matrix, V is an $n \times n$ orthogonal matrix and S is a diagonal $m \times n$ matrix with non-negative diagonal elements so that

$$UU^T = U^TU = I, \quad VV^T = V^TV = I, \tag{7.4}$$

$$S_{ij} = 0 \ \text{for} \ i \neq j, \quad S_{jj} \equiv s_j \geq 0. \tag{7.5}$$

The quantities s_j are known as the singular values of the matrix A. An attractive feature of the singular value decomposition method is that an efficient Fortran subroutine developed for the CERN program library is available.

Once the matrix is decomposed into the form of (7.3), progress can be made towards a solution. The factorisation of the matrix in this way means that its properties can be readily analysed and manipulation is made less difficult.

7.3.2.2 Normalisation of the unknowns

One of the most important tasks performed by the unfolding routine is the optimisation of the system by rescaling it, so that significant information is not suppressed and non-significant information is not enhanced.

This optimisation is achieved by considering a new unknown vector

$$w_j = \frac{x_j}{x_j^{ini}}, \tag{7.6}$$

which measures the deviation of x from the Monte Carlo input vector x^{ini} (which represents the binned generator level mass distribution shown in Figure 7.9). Multiplying each column of the probability matrix A by the corresponding number of events generated in the bin x_j^{ini} yields

$$\sum_{j=1}^{n_x} A_{ij} w_j = b_i, \tag{7.7}$$

where A_{ij} is no longer the probability, but the actual number of events which were generated in bin j and ended up in bin i. At the end of the unfolding procedure, in order to obtain the correctly normalised unfolded solution, it is necessary to multiply the unfolded vector w by x^{ini}

$$x_j = w_j x_j^{ini}, \qquad j = 1, ..., n_x. \tag{7.8}$$

Normalising in this manner has two main benefits. First, if the initial Monte Carlo distribution is physically motivated so that it is similar to the one being unfolded, the vector w should be smooth with small bin-to-bin variation and thus require

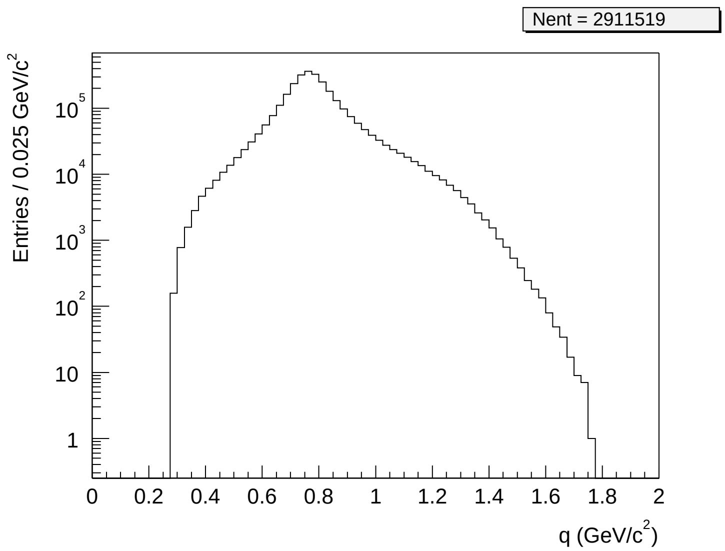

Figure 7.9: *Generator-level Monte Carlo mass spectrum. The binned distribution corresponds to the vector x^{ini} in (7.6).*

less terms in the decomposition into orthogonal functions. As a result, more accurate unfolding should be possible, as fewer unknowns are required in order to obtain the unfolded solution. The second benefit is related to the singular value analysis. In forming a probability matrix (Figure 7.1), some elements may result from a single event and thus contain the largest possible value of one. The corresponding equations will receive an unjustifiably high weight. At the same time, statistically well-determined elements will have values less than one as a result of finite resolution and limited acceptance. By choosing a number-of-event matrix (Figure 7.2), we give larger weights to the better determined equations, as the elements of A are large if the generated statistics are large.

7.3.2.3 Rescaling equations

Considering the initial problem from another viewpoint, (7.1) represents the solution of the least-square problem

$$\sum_{i=1}^{n_b}\left(\sum_{j=1}^{n_x} A_{ij}x_j - b_i\right)^2 = \text{ min}, \tag{7.9}$$

which is adequate if the errors on the elements of vector b are identical. This is not generally the case and for this reason the `GURU` package considers the more general weighted least-squares problem

$$\sum_{i=1}^{n_b}\left(\frac{\sum_{j=1}^{n_x} A_{ij}x_j - b_i}{\Delta b_i}\right)^2 = \text{ min}, \tag{7.10}$$

where Δb_i is the error in b_i. The general case of (7.10) can be written as

$$(Ax-b)^T B^{-1}(Ax-b) = \text{ min}, \tag{7.11}$$

where B is the covariance matrix of the measured vector b.

If B is not diagonal, equation rescaling becomes slightly more complicated. Singular value decomposition of B yields

$$B = QRQ^T, \quad R_{ii} \equiv r_i^2 \neq 0, \quad R_{ij} = 0 \text{ for } i \neq j, \quad B^{-1} = QR^{-1}Q^T. \tag{7.12}$$

From (7.11), it can be shown that after rescaling,

$$(\tilde{A}w - \tilde{b})^T(\tilde{A}w - \tilde{b}) = \text{ min}, \tag{7.13}$$

where

$$\tilde{A}_{ij} = \frac{1}{r_i}\sum_m Q_{im}A_{mj}, \quad \tilde{b}_i = \frac{1}{r_i}\sum_m Q_{im}b_m \tag{7.14}$$

and the minimisation leads to the following system

$$\sum_j \tilde{A}_{ij}w_j = \tilde{b}_i. \tag{7.15}$$

The covariance matrix of $\tilde{b}$, $\tilde{B}$, is now explicitly made equal to the unit matrix, I, and all equations have equal importance.

7.3.2.4 Regularisation and unfolding

Having made the transition from (7.1) to (7.15) the main problem with small singular values still remains. The exact solution of (7.15) will still lead to a rapidly oscillating distribution, which may have a smaller amplitude, but is still useless. However, having expressed the problem in a more convenient form, one can now attempt to avoid these unstable results. In order to suppress the oscillatory component, a *regularisation* or *stabilisation* term is added:

$$(\tilde{A}w - \tilde{b})^T(\tilde{A}w - \tilde{b}) + \tau \cdot (Cw)^T Cw = \text{ min.} \tag{7.16}$$

The matrix C defines an *a priori* condition on the solution and the regularisation parameter τ determines the weight of this condition. Because the solution w ought to be smooth, the 'curvature' of the discrete distribution w_j is defined as the sum of the squares of its second derivatives,

$$\sum_i [(w_{i+1} - w_i) - (w_i - w_{i-1})]^2, \tag{7.17}$$

so that the choice

$$C = \begin{pmatrix} -1 & 1 & 0 & 0 & & & \cdots & & \\ 1 & -2 & 1 & 0 & & & \cdots & & \\ 0 & 1 & -2 & 1 & & & \cdots & & \\ & & & & \ddots & & & & \\ & \cdots & & & & 1 & -2 & 1 \\ & \cdots & & & & 0 & 1 & -1 \end{pmatrix} \tag{7.18}$$

will suppress solutions w having large curvatures.

The choice of the parameter τ is now essential. Choosing a value which is too small will produce a solution which contains meaningless fluctuations. A value of τ which is too large will however result in significant physical information being lost. A simulated test distribution, b^{test}, (for which the solution x^{test} is known) can be used to select the optimum value for the parameter τ.

7.3.3 Treatment of errors

The unfolding procedure implements a full propagation of errors from the measured distribution to the unfolded one. During unfolding however, a systematic uncertainty is introduced as a result of the limited statistics used to produce the detector response matrix. Off-diagonal elements of the matrix, along with on-diagonal elements corresponding to low and high masses, lead to the largest systematic errors, since these elements are calculated using small numbers of Monte Carlo events.

In order to estimate the effect on the final mass spectrum, the unfolding procedure can be carried out with a response matrix in which each element is modified. The modification is carried out so that if A_{ij} is an element of the matrix,

$$A_{ij} \rightarrow A_{ij} + R\,\sigma(A_{ij}), \tag{7.19}$$

where $\sigma(A_{ij})$ is the statistical error on the element A_{ij} and R is a random number taken from a normal distribution, centred about zero, with variance one. If this process is repeated a number of times, a distribution of values for each bin in the mass spectrum can be produced. An example of such a distribution is displayed in Figure 7.10, a fit to the histogram provides an estimate of the uncertainty introduced in the value for the contents of the corresponding bin in the final invariant mass spectrum.

The resulting bin-by-bin estimate of the uncertainty (as a percentage) is displayed in Figure 7.11. The estimated uncertainty is clearly larger for lower and higher mass bins (those which have the lowest statistics in the corresponding detector response matrix). One could clearly reduce the fractional error introduced by increasing the number of Monte Carlo events available (or by using the same number of events with a more efficient selection algorithm).

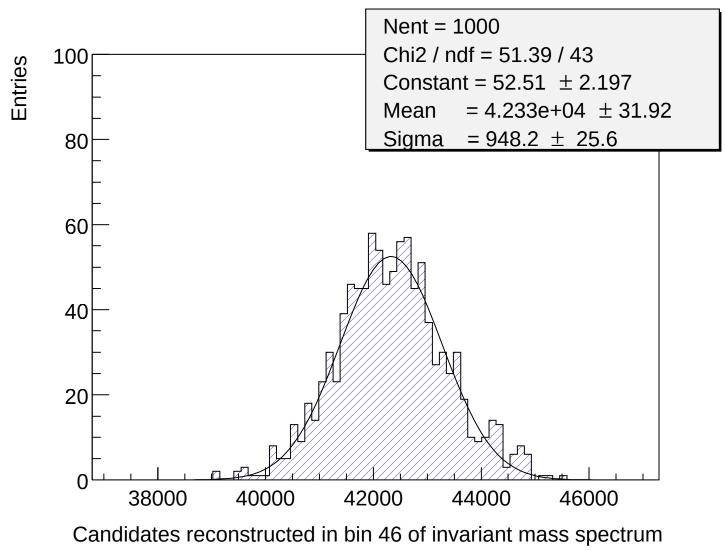

Figure 7.10: *The spread in values achieved for the 46th bin of the $\pi^-\pi^0$ mass spectrum as a result of performing the unfolding procedure 1000 times. Each time a slightly different detector response matrix is used. Each different matrix is the result of modifying each element of the original matrix by a random number times the statistical error on that element (see (7.19)).*

By including all normalisation factors and taking into account the bin width, the partial width for $\tau^- \to \pi^-\pi^0\nu_\tau$ can be extracted from the unfolded spectrum provided by the GURU program, and is shown in (Figure 7.12). It should be noted that there are strong correlations between the data points due to the unfolding procedure.

The additional backgrounds at low invariant masses (Section 7.1) in the data spectrum, combined with the decrease in reconstruction efficiency with decreasing mass (and hence larger efficiency correction at low masses), lead to a shape which has a clear excess in low mass bins, evident as a shoulder in the distribution.

The covariance matrix resulting from the unfolding procedure error propagation is not diagonal. A full covariance matrix (Figure 7.13) is made available in the output from the GURU program, so that bin-to-bin correlations can be considered during any subsequent fitting procedure (the error bars shown in Figure 7.12 do not take into account the off-diagonal terms of the covariance matrix, but do include the estimated systematic error resulting from the unfolding procedure). However, before the unfolded spectrum can be fitted to the models with any confidence, further understanding of the contribution of backgrounds at low invariant masses will be needed, and additional Monte Carlo must be made available, as the GURU algorithm ideally requires a factor of two more Monte Carlo than data.

7.4 Conclusions

An analysis has been developed to select $\tau^- \to \pi^-\pi^0\nu_\tau$ events from *BABAR* data in order to investigate structure in the $\pi^-\pi^0$ invariant mass spectrum. From fits to several models for the weak pion form factor, parameters for the $\rho(1450)$ resonance are obtained. The strength of coupling to the $\rho(1700)$ is also determined for the models in question, and although there is some evidence for a $\rho(1700)$ contribution to the weak pion form factor, the results are inconclusive.

A detailed investigation into the sources of background is clearly necessary if the effects of the background subtraction are to be well understood, particularly at low invariant masses where there appears to be a considerable contribution to the mass spectrum from unsimulated backgrounds. Such detailed studies should also allow the efficiency and purity of the selected sample to be improved.

Further *BABAR* data, together with much larger Monte Carlo samples should allow further progress in determining the strength of any coupling to a $\rho(1700)$, and lead to a detailed understanding of systematic errors. Such developments should eventually allow fits to unfolded data distributions and a measurement of F_π.

An investigation into constants used in the generation of the τ-pair Monte Carlo is necessary, and should it be required, any subsequent Monte Carlo production should make use of modified constants. The $\rho(770)$ parameters used in the simulation are clearly of particular interest.

A software package has been developed to provide a framework for any future studies. The necessary C++ classes are included, as are numerous software tools.

This thesis demonstrates that the *BABAR* experiment has the potential to produce precision measurements in τ physics for many years to come.

Table 7.2: *Results from the Kühn and Santamaria and Gounaris and Sakurai fits to the $\pi^-\pi^0$ mass spectrum. Units for all masses and widths are MeV/c^2.*

Parameter	Kühn and Santamaria model		Gounaris and Sakurai model	
	without $\rho(1700)$	with $\rho(1700)$	without $\rho(1700)$	with $\rho(1700)$
M_ρ	$\equiv 775.0$	$\equiv 775.0$	$\equiv 775.0$	$\equiv 775.0$
Γ_ρ	$\equiv 150.0$	$\equiv 150.0$	$\equiv 150.0$	$\equiv 150.0$
β	-0.107 ± 0.003	-0.097 ± 0.006	-0.087 ± 0.003	-0.083 ± 0.004
$M_{\rho'}$	1372 ± 9	1360 ± 10	1375 ± 10	1365 ± 10
$\Gamma_{\rho'}$	416 ± 23	396 ± 23	402 ± 29	382 ± 21
γ	—	-0.010 ± 0.005	—	-0.004 ± 0.003
$M_{\rho''}$	—	$\equiv 1700$	—	$\equiv 1700$
$\Gamma_{\rho''}$	—	$\equiv 235$	—	$\equiv 235$
χ^2/dof	57.4/36	56.7/35	58.1/36	58.0/35

Table 7.3: *Correlation matrix for the Kühn and Santamaria fit without a ρ(1700) contribution.*

$$
\begin{array}{cc}
\begin{array}{c} \text{Norm.} \\ \beta \\ M_{\rho'} \\ \Gamma_{\rho'} \end{array} &
\begin{pmatrix}
1.00 & & & \\
0.95 & 1.00 & & \\
-0.14 & -0.19 & 1.00 & \\
-0.59 & 0.68 & 0.69 & 1.00
\end{pmatrix} \\
 & \begin{array}{cccc} \text{Norm.} & \beta & M_{\rho'} & \Gamma_{\rho'} \end{array}
\end{array}
$$

Table 7.4: *Correlation matrix for the Kühn and Santamaria fit with a ρ(1700) contribution.*

$$
\begin{array}{cc}
\begin{array}{c} \text{Norm.} \\ \beta \\ M_{\rho'} \\ \Gamma_{\rho'} \\ \gamma \end{array} &
\begin{pmatrix}
1.00 & & & & \\
0.30 & 1.00 & & & \\
0.11 & -0.55 & 1.00 & & \\
-0.44 & -0.61 & 0.66 & 1.00 & \\
0.29 & 0.81 & 0.61 & 0.29 & 1.00
\end{pmatrix} \\
 & \begin{array}{ccccc} \text{Norm.} & \beta & M_{\rho'} & \Gamma_{\rho'} & \gamma \end{array}
\end{array}
$$

Table 7.5: *Comparison of results from fits to BABAR data with parameters extracted from fits performed by the CLEO collaboration (ALEPH did not quote results for fits to models with two resonances only). Units for all masses and widths are MeV/c^2.*

Parameter	BABAR	CLEO
Kühn and Santamaria model		
M_ρ	$\equiv 775$	774.9 ± 0.5
Γ_ρ	$\equiv 150$	149.0 ± 1.1
β	-0.107 ± 0.003	-0.108 ± 0.007
$M_{\rho'}$	1372 ± 9	1364 ± 7
$\Gamma_{\rho'}$	416 ± 23	400 ± 26
χ^2/dof	57.4/36	27.0/24
Gounaris and Sakurai model		
M_ρ	$\equiv 775$	775.3 ± 0.5
Γ_ρ	$\equiv 150$	150.5 ± 1.1
β	-0.087 ± 0.003	-0.084 ± 0.006
$M_{\rho'}$	1375 ± 10	1365 ± 7
$\Gamma_{\rho'}$	402 ± 29	356 ± 26
χ^2/dof	58.1/36	26.8/24

Table 7.6: *Current Particle Data Group values for resonance parameters. Units are MeV/c^2.*

Parameter	Value
M_ρ	769.3 ± 0.8
Γ_ρ	150.2 ± 0.8
$M_{\rho'}$	1465 ± 25
$\Gamma_{\rho'}$	310 ± 60

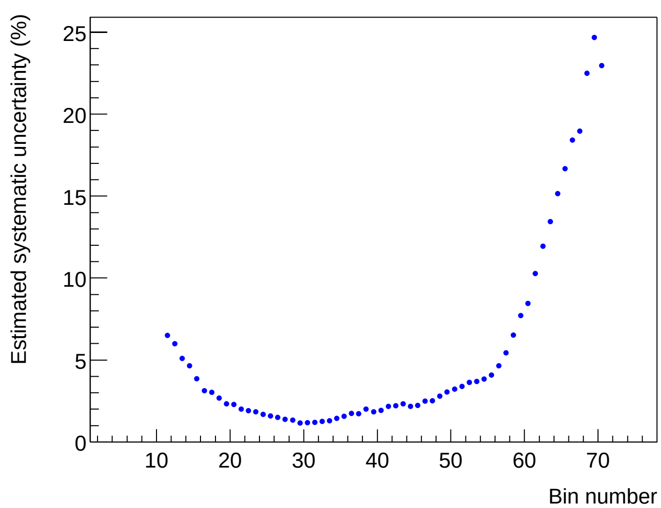

Figure 7.11: *Estimated systematic uncertainty (as a percentage) for each bin of the unfolded mass spectrum. This uncertainty arises due to statistical limitations in the detector response matrix.*

Table 7.7: *Comparison of results from fits to BABAR data with parameters extracted from fits performed by the ALEPH and CLEO experiments. A contribution from the $\rho(1700)$ is included in the fits.*

Parameter	BABAR	ALEPH	CLEO
Kühn and Santamaria model			
M_ρ	$\equiv 775$	774.9 ± 0.9	774.6 ± 0.5
Γ_ρ	$\equiv 150$	144.2 ± 1.5	149.0 ± 1.2
β	-0.097 ± 0.006	-0.094 ± 0.007	-0.167 ± 0.008
$M_{\rho'}$	1360 ± 10	1363 ± 15	1408 ± 12
$\Gamma_{\rho'}$	396 ± 23	$\equiv 310$	502 ± 32
γ	-0.010 ± 0.005	-0.015 ± 0.008	0.050 ± 0.010
$M_{\rho''}$	$\equiv 1700$	$\equiv 1700$	$\equiv 1700$
$\Gamma_{\rho''}$	$\equiv 235$	$\equiv 235$	$\equiv 235$
χ^2/dof	56.7/35	81/65	23.2/23
Gounaris and Sakurai model			
M_ρ	$\equiv 775$	776.4 ± 0.9	775.1 ± 0.6
Γ_ρ	$\equiv 150$	150.5 ± 1.6	150.4 ± 1.2
β	-0.083 ± 0.004	-0.077 ± 0.008	-0.121 ± 0.009
$M_{\rho'}$	1365 ± 10	1400 ± 16	1406 ± 13
$\Gamma_{\rho'}$	382 ± 21	$\equiv 310$	455 ± 34
γ	-0.004 ± 0.003	-0.001 ± 0.009	-0.032 ± 0.009
$M_{\rho''}$	$\equiv 1700$	$\equiv 1700$	$\equiv 1700$
$\Gamma_{\rho''}$	$\equiv 235$	$\equiv 235$	$\equiv 235$
χ^2/dof	58.0/35	54/65	22.9/23

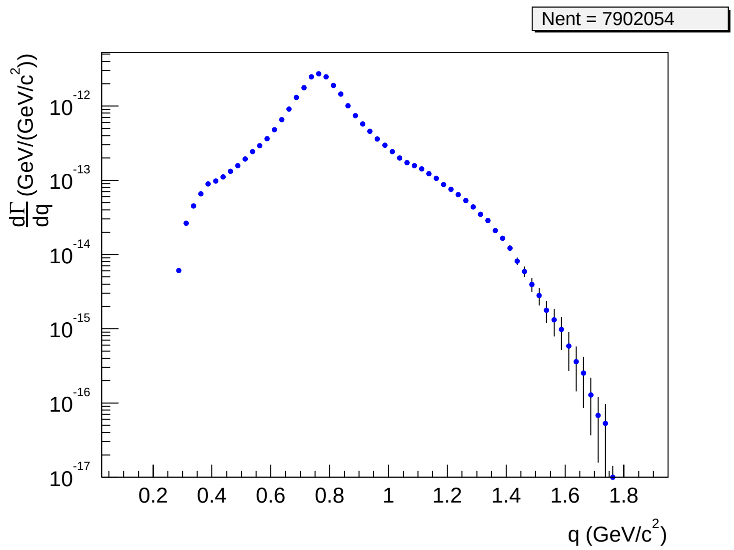

Figure 7.12: *Fully corrected partial width for $\tau^- \rightarrow \pi^-\pi^0\nu_\tau$ as a function of $\pi^-\pi^0$ mass.*

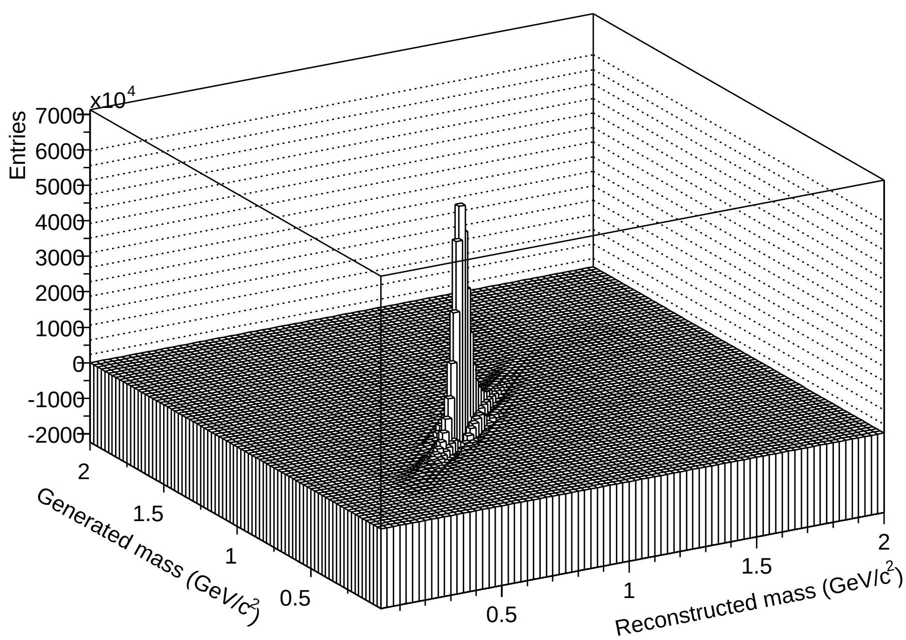

Figure 7.13: *Covariance matrix resulting from the unfolding of the measured invariant mass distribution.*

A

Electromagnetic calorimeter cluster lateral moment

Considering an EMC cluster composed of N crystals with energies E_i, if the energies are ordered so that $E_1 > E_2 > ... > E_N$, we can define a lateral shower shape parameter as

$$LAT = \frac{\sum\limits_{i=3}^{N} E_i r_i^2}{\sum\limits_{i=3}^{N} E_i r_i^2 + E_1 r_0^2 + E_2 r_0^2},$$

where r_0 is the average distance between two crystals (about 5 cm for the *BABAR* electromagnetic calorimeter). The distance, r_i, of each crystal from the cluster centre is measured in a plane perpendicular to the line joining the interaction point and the cluster centre.

The lateral shower shape parameter can be used to discriminate between electromagnetic and hadronic showers. For electromagnetic showers, most of the energy is deposited in a small number of crystals, so that one expects a low value for the LAT parameter. Hadronic showers however, generally result in a distribution of energy which is more even through a number of crystals, resulting in a value for the LAT parameter which is closer to one.

B

Track-cluster matching

In order to match tracks to electromagnetic calorimeter clusters, the separations in θ and ϕ of the track and cluster at the front face of the calorimeter are considered. The intersection of a track with the front face of the calorimeter is found, and the reconstructed centroid position of the cluster is projected onto the front face of the calorimeter (by assuming that the cluster direction lies along the radial direction from the interaction point). The curvature of the charged track results in a signed shift between the track intersection point and the projected cluster centroid. The sign of the shift depends on the charge of the candidate in question.

The mean and sigma (σ) values of the distributions of the separations are parameterised in terms of track momentum, charge and $\cos\theta$ in order to calculate a match-consistency for each track-cluster pair. Charged candidates are constructed by combining the best-matched track-bump pairs with consistency levels at or above the 10^{-6} level.

References

[1] D. Boutigny et al. *BABAR* technical design report. Technical Report SLAC-R-0457, 1995.

[2] An asymmetric B factory based on PEP, the conceptual design report for PEP-II. SLAC-372, 1991.

[3] D. E. Groom et al. Review of particle physics. *Eur. Phys. J.*, C15:1, 2000.

[4] Martin L. Perl et al. *Phys. Rev. Lett.*, 35:1489, 1975.

[5] J. Z. Bai et al. *Phys. Rev.*, D53:20–34, 1996.

[6] Martin L. Perl. Tau physics. SLAC-PUB-6071, 1992.

[7] R. Barate et al. *Z. Phys.*, C74:387, 1997.

[8] D. Buskulic et al. *Z. Phys.*, C70:549–560, 1996.

[9] D. Decamp et al. *Phys. Lett.*, B279:411–421, 1992.

[10] D. Buskulic et al. *Phys. Lett.*, B297:432–448, 1992.

[11] R. Balest et al. *Phys. Lett.*, B388:402, 1996.

[12] Fumihiko Takasaki. *eConf*, C990809:12–21, 2000.

[13] G. Viehhauser. The CLEO III upgrade. *Nucl. Instrum. Meth.*, A446:97, 2000.

[14] M. Finkemeier and E. Mirkes. HEP-PH/9508312, 1995.

[15] I. J. R. Aitchison and A. J. G. Hey. *Gauge Theories in Particle Physics: A Practical Introduction*. Hilger, Bristol UK, second edition, 1989.

[16] J. H. Kuhn and E. Mirkes. *Z. Phys.*, C56:661–672, 1992.

[17] Yung-Su Tsai. *Phys. Rev.*, D4:2821, 1971.

[18] Martin L. Perl. *Rept. Prog. Phys.*, 55:653–722, 1992.

[19] S. Anderson et al. *Phys. Rev.*, D61:112002, 2000.

[20] J. H. Kuhn and A. Santamaria. *Z. Phys.*, C48:445–452, 1990.

[21] G. J. Gounaris and J. J. Sakurai. *Phys. Rev. Lett.*, 21:244, 1968.

[22] R. Barate et al. *Z. Phys.*, C76:15, 1997.

[23] L. M. Barkov et al. *Nucl. Phys.*, B256:365, 1985.

[24] B. Aubert et al. The first year of the *BABAR* experiment at PEP-II. *BABAR*-CONF-00/17, submitted to the XXXth International Conference on High Energy Physics, Osaka, Japan, 2000.

[25] J. Seeman et al. PEP-II new high power low impedance movable collimator. Invited talk at 7th European Particle Accelerator Conferences (EPAC 2000), Vienna, Austria, 26-30 Jun 2000.

[26] C. Bozzi et al. *Nucl. Instrum. Meth.*, A435:25–33, 1999.

[27] G. Sciolla et al. *Nucl. Instrum. Meth.*, A419:310, 1998.

[28] P. F. Harrison and H. R. Quinn ed. The *BABAR* physics book: Physics at an asymmetric B factory. Papers from workshop on physics at an asymmetric B

factory (*BABAR* collaboration meeting), Rome, Italy, 11-14 Nov 1996, Princeton, NJ, 17-20 Mar 1997, Orsay, France, 16-19 Jun 1997 and Pasadena, CA, 22-24 Sep 1997.

[29] Johannes M. Bauer. The CsI(Tl) calorimeter of the *BABAR* detector. Talk given at 7th International Conference on Calorimetry in High-Energy Physics (ICCHEP 97), Tucson AZ, 9-14 Nov 1997.

[30] S. Gehrig. Design and simulated performance of the Level-1 trigger system. SLAC-BABAR-NOTE-380, 1997.

[31] H. Schildt. *C++: The Complete Reference Third Edition*. Osbourne McGraw-Hill, 1998.

[32] S. Jadach and Z. Was. *Comput. Phys. Commun.*, 36:191, 1985.

[33] Stanislaw Jadach, Johann H. Kuhn, and Z. Was. *Comput. Phys. Commun.*, 64:275, 1990.

[34] B. Lockman. Offline simulation. Talk at *BABAR* Software Week, June 16-19 1999.

[35] CERN. *GEANT, detector description and simulation tool*, 1994. Program library long writeup W5013.

[36] B. Jacobsen. Guide to the bear package. `http://www.slac.stanford.edu/BFROOT/www/Computing/Offline/Reconstruction/PackageGuides/BearGuide.ps`.

[37] R. Akers et al. CERN-PPE/93-145.

[38] F. A. Berends, P. H. Daverveldt, and R. Kleiss. *Nucl. Phys.*, B253:441, 1985.

[39] F. A. Berends, P. H. Daverveldt, and R. Kleiss. *Phys. Lett.*, B148:489, 1984.

[40] P. Kessler ed. Gamma gamma physics. Proceedings, seminar Paris France, Mar 11-12 1982. Coll. De France (1982) 235 P. and Coll. De France - L.P.C.-82-14 (82,REC.OCT.) 235p.

[41] P. H. Daverveldt F. A. Berends and R. Kleiss. Monte carlo simulation of two-photon processes. CPC Software Library. `http://rylibweb.man.ac.uk/data1/ir/ejnl/cpcacf.html`.

[42] T. McMahon et al. Electron ID analysis working group documentation. `http://www.slac.stanford.edu/BFROOT/www/Physics/Tools/Pid/Electrons/index.html`.

[43] P. D. Strother. The BetaPidCalib users guide. `http://www.slac.stanford.edu/BFROOT/www/Physics/Tools/Pid/Doc/BetaPidCalib/bpc.html`.

[44] J. J. Back. PhD thesis, Queen Mary and Westfield College, London UK, 1999.

[45] J. L. Harton. Filter and trigger efficiency for tau/QED/QCD/two-photon physics. `http://www.slac.stanford.edu/BFROOT/www/Physics/Meetings/Padova/talks/TauQED/padova_filter.html`.

[46] C. Roat. Nano/micro database summary for *BABAR* release versions 8.6.x. `http://www.slac.stanford.edu/BFROOT/www/doc/workbook/nanomicro/v8.6/`.

[47] Reiner Seitz. Describing energy deposit in CsI crystals. 1996. SLAC-BABAR-NOTE-294.

[48] C. Hearty et al. Muon ID analysis working group documentation. `http://www.slac.stanford.edu/BFROOT/www/Physics/Tools/Pid/muons.html`.

[49] F. James et al. `MINUIT`. *CERN*, DD/D506, 1987.

[50] Andreas Hocker and Vakhtang Kartvelishvili. *Nucl. Instrum. Meth.*, A372:469–481, 1996.